

Electronic Thesis and Dissertation Repository

7-28-2011 12:00 AM

FEM-FCT Based Dynamic Simulation of Trichel Pulse Corona Discharge in Point-Plane Configuration

Paria Sattari
The University of Western Ontario

Supervisor
Dr. K. Adamiak
The University of Western Ontario Joint Supervisor
Dr. G.S.P. Castle
The University of Western Ontario

Graduate Program in Electrical and Computer Engineering
A thesis submitted in partial fulfillment of the requirements for the degree in Doctor of Philosophy
© Paria Sattari 2011

Follow this and additional works at: <https://ir.lib.uwo.ca/etd>



Part of the [Electromagnetics and Photonics Commons](#)

Recommended Citation

Sattari, Paria, "FEM-FCT Based Dynamic Simulation of Trichel Pulse Corona Discharge in Point-Plane Configuration" (2011). *Electronic Thesis and Dissertation Repository*. 215.
<https://ir.lib.uwo.ca/etd/215>

This Dissertation/Thesis is brought to you for free and open access by Scholarship@Western. It has been accepted for inclusion in Electronic Thesis and Dissertation Repository by an authorized administrator of Scholarship@Western. For more information, please contact wlsadmin@uwo.ca.

**FEM-FCT BASED DYNAMIC
SIMULATION OF TRICHEL PULSE
CORONA DISCHARGE IN
POINT-PLANE CONFIGURATION**

(Spine title: Numerical Simulation of Trichel Pulse Corona Discharge)

(Thesis format: Monograph)

by

Paria Sattari

Graduate Program in Engineering Science
Department of Electrical and Computer Engineering

A thesis submitted in partial fulfillment
of the requirements for the degree of
Doctor of Philosophy

School of Graduate and Postdoctoral Studies
The University of Western Ontario
London, Ontario, Canada
July, 2011

© Paria Sattari 2011

Certificate of Examination

THE UNIVERSITY OF WESTERN ONTARIO
SCHOOL OF GRADUATE AND POSTDOCTORAL STUDIES

Chief Advisors:

Dr. Kazimierz Adamiak

Dr. G. S. Peter Castle

Advisory Committee:

Examining Board:

Dr. Anestis Dounavis

Dr. Wamadeva Balachandran

Dr. William D. Greason

Dr. Dimitre Karamanev

The thesis by
Paria Sattari
entitled:

**FEM-FCT BASED DYNAMIC SIMULATION OF TRICHEL PULSE
CORONA DISCHARGE IN POINT-PLANE CONFIGURATION**

is accepted in partial fulfillment of the
requirements for the degree of
Doctor of Philosophy

Date: _____

Chair of Examining Board

Abstract

In this thesis, a new two-dimensional numerical solver is presented for the dynamic simulation of the Trichel pulse regime of negative corona discharge in point-plane configuration. The goal of this thesis is to simulate the corona discharge phenomenon and to improve existing models so that the results have an acceptable compatibility with the experimentally obtained data. The numerical technique used in this thesis is a combination of Finite Element Method (FEM) and Flux Corrected Transport (FCT). These techniques are proved to be the best techniques, presented so far for solving the nonlinear hyperbolic equations that simulate corona discharge phenomenon.

The simulation begins with the single-species corona discharge model and the different steps of the numerical technique are tested for this simplified model. The ability of the technique to model the expected physical behaviour of ions and electric field is investigated. Then, the technique is applied to a more complicated model of corona discharge, a three-specie model, in which three ionic species exist in the air gap: electrons, and positive and negative oxygen ions. Avalanche ionization, electron attachment and ionic recombination are the three ionic reactions which this model includes.

The macroscopic parameters i.e., the average corona current and the Trichel pulses period are calculated and compared with the available experimental data. The technique proves to be compatible with the available experimental results. Finally, the effects of different parameters on the Trichel pulse characteristics are investigated. The results are further compared against the available experimental data for the effect of pressure on Trichel pulse characteristics and are reported to be compatible.

Keywords: negative electric corona discharge, Trichel pulse, finite element method, flux corrected transport, numerical simulation.

Acknowledgements

I would like to give my best regards and gratefulness to Prof. K. Adamiak. Without his consistent help, support, and guidance, I would have been lost in the middle of this project.

Secondly, I would like to thank Prof. G.S.P Castle for his invaluable comments during the course of this project. His great insight and profound knowledge was of great help for me.

I also like to acknowledge the helpful discussions and advises of C.F. Gallo and Dr. P. Atten at different stages of my project.

I would also like to thank Mr. Dan Sich from the library, who helped me find many papers. My thanks to Mr. B. Saunders and Mr. T. Hunt for their help with Linux operating systems and the SHARCNET of Canada for the resources they provided for my computational analysis.

I am grateful to NSERC of Canada and UWO for their financial support. I also acknowledge and admire my colleagues for helping me during the course of this project.

Last but not least, I take this opportunity to thank my husband, Nima, and my parents, for their unconditional love and support they gave me during these years.

Dedication

To my family;

Nima, Roohangiz, Siavash, Pegah, and Sara

Table of Contents

Certificate of Examination	ii
Abstract	iii
Acknowledgements	iv
Dedication	v
List of Figures	x
List of Tables	xiv
Acronyms	xv
Nomenclature	xvii
1 Introduction	1
1.1 What is Corona Discharge?	1
1.2 Features of Corona Discharge	2
1.3 Types of Corona Discharge	4
1.4 Mechanism of Negative and Positive corona	4
1.5 Thesis Objectives	6
1.6 Thesis Outline	9

2	Negative Corona Discharge	12
2.1	Mechanism of Trichel Pulse Corona Discharge	12
2.2	Ionic Reactions	17
2.2.1	Ionization	18
2.2.2	Attachment	18
2.2.3	Detachment	19
2.2.4	Ionic Recombination	19
2.2.5	Ozone Generation and Decomposition	20
2.3	Literature Review	21
2.4	Motivation	25
2.5	Conclusions	26
3	Mathematical Models and Numerical Algorithms in Electric Corona Simulation	28
3.1	Introduction	28
3.2	Literature Review on Mathematical Models for the Trichel Pulse Simulation	29
3.3	Literature Review on the Numerical Techniques	30
3.3.1	Numerical Techniques for Calculating the Electric Field	31
3.3.2	Numerical Methods for Calculating the Space Charge Density	34
3.3.3	Numerical Algorithms for the Simulation of Corona Discharge	36
3.4	Why FEM-FCT?	41
3.5	Finite Element Method	43
3.6	Combined FEM-FCT	48
3.7	Conclusions	54
4	Implementation of FEM-FCT Algorithm for Trichel Pulse Simulation	55
4.1	Governing Equations	55
4.2	Implementation of the Numerical Algorithm	61
4.3	Optimization Techniques	65
4.4	Conclusions	67

5	Dynamic Simulation of Single Species Corona Discharge	69
5.1	Introduction	69
5.2	Mathematical Model	70
5.2.1	Governing Equations	70
5.2.2	Boundary Conditions	71
5.3	Results	75
5.3.1	Step Voltage	75
5.3.2	Pulse Voltage	79
5.4	Conclusions	87
6	Two dimensional Simulation of Trichel Pulses in Air	89
6.1	Introduction	89
6.2	Basic Equations	90
6.3	Boundary Conditions	91
6.4	Numerical Algorithm	92
6.5	Current Components	94
6.6	Results	96
6.6.1	Applied Voltage = -8kV	97
6.6.2	Applied Voltage = -10kV	103
6.7	Conclusions	107
7	A Parametric Study on Trichel Pulse Characteristics	108
7.1	Introduction	108
7.2	Effect of Different Parameters on Trichel Pulse Characteristics	109
7.2.1	External Resistance	109
7.2.2	Ion Mobility	111
7.2.3	Secondary Electron Emission Coefficient	117
7.3	Spatial Distribution of Ionic Species in Air Gap	118
7.4	Shape of Ionization Layer	119
7.5	Conclusions	121

8	Experimental Verifications of the Numerical Results	125
8.1	Introduction	125
8.2	Comparison With Gallo's Experimental Data	126
8.3	Appearance and Physics of the Trichel Pulse Near Needle Tip	128
8.4	Revised Comparison With Gallo's Experimental Data	131
8.5	Effect of Pressure on Trichel Pulse Characteristics	132
8.6	Comparison with Atten's Experimental Data	133
8.7	Conclusions	135
9	Modelling of Corona Discharge in Oxygen	136
9.1	Introduction	136
9.2	Databases	137
9.3	Available Discharge Models	137
9.3.1	Morrow's Model [30]	140
9.3.2	Eliasson et al. Model [23]	140
9.4	Results	143
10	Summary, Conclusions and Recommendations for Future Study	152
10.1	Summary	152
10.1.1	Dynamic Single-Species Model of Corona Discharge	152
10.1.2	Simulation of Trichel Pulse in Air	153
10.1.3	Parametric Study of Trichel Pulse Characteristics	154
10.1.4	Experimental Verification of the Numerical Results	154
10.1.5	Trichel Pulse Simulation in Oxygen	154
10.2	Conclusions	155
10.3	Recommendations for Future Study	157
Appendices		
A	Appendix A	172
A.1	Oxygen Model Databases	172
B	Curriculum Vitae	178

List of Figures

1.1	Types of positive corona discharge, from left: burst corona, glow corona, streamer corona, spark discharge.	6
1.2	Types of negative corona discharge, from left: Trichel pulse corona, pulseless corona, spark.	7
2.1	Ionic reactions in corona discharge. The scaling is not accurate. . . .	15
2.2	Electric field in different regions during Trichel pulse corona discharge, the circles represents the ion clouds.	16
4.1	The configuration of corona discharge system.	56
5.1	Flowchart of the simulation process.	76
5.2	FE grid used in the simulation process.	77
5.3	Corona current versus time ($R_{ext} = 50M\Omega, V = 10kV$)	78
5.4	Corona current versus time for two different external resistances ($V=10kV$). 79	
5.5	Current versus time for two different input voltages ($R_{ext} = 5M\Omega$). . .	80
5.6	Space charge density along the axis of symmetry at six different instants of time ($R_{ext} = 50M\Omega$).	80
5.7	Applied pulse voltage described by $V_s(t) = \frac{V_m t}{t_m} e^{(1-\frac{t}{t_m})} + V_{DC}$	81
5.8	Corona current versus time for the pulse voltage shown in Figure 5.7 ($R_{ext} = 50M\Omega$).	82
5.9	Space charge density on the tip of the corona point versus time for the pulse voltage ($R_{ext} = 50M\Omega$).	82
5.10	Charge density along the axis for five different time instants after the first voltage pulse ($R_{ext} = 50M\Omega$).	83
5.11	Charge distribution in the space for a pulse energization at $t=10 \mu s$ ($R_{ext} = 50M\Omega$).	84
5.12	Charge distribution in the space for a pulse energization at $t=210 \mu s$ ($R_{ext} = 50M\Omega$).	84

Table of Contents

5.13	Corona current versus time for a pulse energization, ($f = 5kHz$, $R_{ext} = 50M\Omega$)	85
5.14	Corona current versus time for a pulse energization, ($f = 50kHz$, $R_{ext} = 50M\Omega$)	86
5.15	Charge distribution in the space between both electrodes at $t=41 \mu s$.	86
6.1	Details of FE grid near corona electrode used in the simulation process.	94
6.2	Circuit model of the needle-plane configuration.	96
6.3	Corona current for $V = -8kV$	98
6.4	Displacement current for $V = -8kV$	99
6.5	Total current for $V = -8kV$, the amplitude of the first pulse is approx- imately equal to the amplitude of the displacement current at $t=0$. . .	99
6.6	Characteristic points on a typical Trichel pulse: 1 - beginning of the pulse, 2 - half-pulse rising, 3 - maximum of the pulse, 4 - half-pulse decreasing, 5 - end of the pulse, 6 -9 microseconds after the pulse . .	100
6.7	Electron density along the axis of symmetry at different instants during a Trichel pulse (In figures 6.7, 6.8 and 6.9, the minimum scale on y axis is chosen to be 0.0001 and the values below this level are considered as noise. Therefore the curves which do not exist in these figures are in the noise level).	101
6.8	Positive ion density along the axis of symmetry at different instants during a Trichel pulse.	102
6.9	Negative ion density along the axis of symmetry at different instants during a Trichel pulse.	102
6.10	Electric field along the axis of symmetry at different instants during a Trichel pulse.	104
6.11	Trichel pulse for $V=-10kV$	105
6.12	Total electron charge in the air gap versus time.	105
6.13	Total negative ion charge in the air gap versus time.	106
6.14	Total positive ion charge in the air gap versus time.	106
7.1	Trichel pulse period versus applied voltage for different external resis- tances	112
7.2	Average corona current versus applied voltage for different external resistances	112

Table of Contents

7.3	Total charge of positive ions versus time ($R_{ext} = 10k\Omega$)	113
7.4	Total charge of positive ions versus time ($R_{ext} = 100k\Omega$)	113
7.5	Total charge of electrons versus time ($R_{ext} = 10k\Omega$)	114
7.6	Total charge of electrons versus time ($R_{ext} = 100k\Omega$)	114
7.7	Total charge of negative ions versus time ($R_{ext} = 10k\Omega$)	115
7.8	Total charge of negative ions versus time ($R_{ext} = 100k\Omega$)	115
7.9	Total corona current versus time ($R_{ext} = 10k\Omega$)	116
7.10	Total corona current versus time ($R_{ext} = 100k\Omega$)	116
7.11	Trichel pulse period versus secondary electron emission coefficient . .	118
7.12	Average corona current versus secondary electron emission coefficient	119
7.13	Positive ion density at point P1	120
7.14	Electron density at point P1	120
7.15	Negative ion density at point P1	121
7.16	Trichel pulses for $V=-9kV$	122
7.17	The thickness of the ionization layer	122
7.18	Electric field on the tip of corona electrode	123
7.19	Ionization profile at different instants of time	123
8.1	Trichel pulse period versus applied voltage - comparison of experimen- tal and numerical results	127
8.2	Average corona current versus applied voltage: experimental and nu- merical results	128
8.3	Experimental shape of the discharge region	130
8.4	Q_i/Q for $V = -9 kV$	134
9.1	Mobility of electrons versus the reduced electric field	138
9.2	Diffusion coefficient versus the reduced electric field	138
9.3	Ionization frequency versus the reduced electric field	139
9.4	Attachment frequency versus the reduced electric field	139
9.5	Mobility of electrons versus the reduced electric field	143
9.6	Diffusion coefficient versus the reduced electric field	144
9.7	Ionization coefficient versus the reduced electric field	144
9.8	Attachment coefficient versus the reduced electric field	145
9.9	Corona current versus time in oxygen	147
9.10	Corona current versus time in air	147

List of Figures

9.11	Total charge of electrons versus time in oxygen	148
9.12	Total charge of electrons versus time in air	148
9.13	Total charge of positive ions versus time in oxygen	149
9.14	Total charge of positive ions versus time in air	149
9.15	Total charge of negative ions versus time in oxygen	150
9.16	Total charge of negative ions versus time in air	150
9.17	Electric field versus time in oxygen	151
9.18	Electric field versus time in air	151

List of Tables

1.1	Corona discharge classification	6
3.1	A comparison between differential-based and integral-base techniques	31
7.1	Trichel pulse characteristics for different applied voltages, $R_{ext} = 100$ k Ω	111
7.2	Trichel pulse characteristics for different applied voltages, $R_{ext} = 50$ k Ω	111
7.3	Trichel pulse characteristics for different applied voltages, $R_{ext} = 10$ k Ω	111
7.4	Trichel pulse characteristics for $V = -7kV$ and different ion mobilities	117
7.5	Trichel pulse characteristics for different secondary emission coeffi- cients, $V = -7kV$	118
8.1	Rough estimates of dimensions	130
8.2	Trichel pulse characteristics for $V = -4kV$, $r = 10\mu m$, $d = 6mm$. . .	132
8.3	Trichel pulse period and pulse duration versus gas pressure ($V=-9kV$, $R_{ext}=100$ k Ω)	133
8.4	Charge-per-pulse (in picocoulombs) for two configurations with differ- ent radii	134
9.1	Morrow's model coefficients [30]	141
9.2	Eliasson et al. model coefficients based on Zhang et al. [100]	142
A.1	Model coefficients in oxygen: Siglo database	173
A.2	Model coefficients in oxygen: Morgan database	174
A.3	Model coefficients in oxygen: Phelps database	175
A.4	Mobility of positive ions	176
A.5	Mobility of negative ions	177

Acronyms

AC	<i>Alternating Current</i>
BEM	<i>Boundary Element Method</i>
CFD	<i>Computational Fluid Dynamics</i>
CSM	<i>Charge Simulation Method</i>
DC	<i>Direct Current</i>
DCM	<i>Donor Cell Method</i>
ESP	<i>Electrostatic Precipitator</i>
FCT	<i>Flux Corrected Transport</i>
FDM	<i>Finite Difference Method</i>
FEM	<i>Finite Element Method</i>
FVM	<i>Finite Volume Method</i>
MoC	<i>Method of Characteristics</i>
MoM	<i>Method of Moment</i>
ODE	<i>Ordinary Differential Equations</i>
1D	<i>One Dimensional</i>
2D	<i>Two Dimensional</i>
3D	<i>Three Dimensional</i>
3S	<i>Three Species</i>

Nomenclature

\vec{A}	<i>Vector Magnetic Potential ($V.s.m^{-1}$)</i>
\vec{B}	<i>Magnetic Field Intensity (Tesla)</i>
\vec{D}	<i>Electrostatic Displacement ($C.m^{-2}$)</i>
D	<i>Diffusion Coefficient ($m^2.s^{-1}$)</i>
E_o	<i>Onset Value of Electric Field ($V.m^{-1}$)</i>
E_{Peek}	<i>Peek's Value ($V.m^{-1}$)</i>
e_0	<i>Electron Charge (C)</i>
\vec{E}	<i>Electric Field Intensity ($V.m^{-1}$)</i>
EN	<i>Reduced Electric Field (Td)</i>
f	<i>Frequency (Hz)</i>
I	<i>Corona current (A)</i>
I_d	<i>Displacement Current (A)</i>
I_{tot}	<i>Total Current (A)</i>
\vec{j}	<i>Electric Current Density ($A.m^{-2}$)</i>
k	<i>Mobility of Charge Carriers ($m^2.V^{-1}.s^{-1}$)</i>
k_i	<i>Ionization Frequency (s^{-1})</i>
k_a	<i>Attachment Frequency (s^{-1})</i>
k_d	<i>Detachment Frequency (s^{-1})</i>
k_b	<i>Boltzmann Constant ($m^2.kg.s^{-2}.K^{-1}$)</i>
μ_e	<i>Mobility of Electrons ($m^2.V^{-1}.s^{-1}$)</i>
μ_n	<i>Mobility of Negative Ions ($m^2.V^{-1}.s^{-1}$)</i>
μ_p	<i>Mobility of Positive Ions ($m^2.V^{-1}.s^{-1}$)</i>
N_e	<i>Number Density of Electrons (m^{-3})</i>
N_n	<i>Number Density of Negative Ions (m^{-3})</i>
N_p	<i>Number Density of Positive Ions (m^{-3})</i>
NO_2	<i>Concentration of Oxygen Molecules (m^{-3})</i>
P	<i>Pressure (atm)</i>
P_0	<i>Standard Pressure (atm)</i>

Nomenclature

r_{eq}	<i>Electrode Equivalent Radius (m)</i>
R_{ext}	<i>External Resistance (Ω)</i>
t	<i>Time (s)</i>
Δt	<i>Time Step (s)</i>
T	<i>Absolute Temperature (K)</i>
T_0	<i>Standard Temperature (K)</i>
\vec{u}	<i>Velocity of the Ions ($m.s^{-1}$)</i>
V	<i>Electric Potential (V)</i>
V_0	<i>Corona Onset Voltage (V)</i>
\vec{W}_e	<i>Drift Velocity of Electrons ($m.s^{-1}$)</i>
\vec{W}_n	<i>Drift Velocity of Negative Ions ($m.s^{-1}$)</i>
\vec{W}_p	<i>Drift Velocity of Positive Ions ($m.s^{-1}$)</i>
ε_0	<i>Gas Permittivity ($F.m^{-1}$)</i>
β_{ep}	<i>Electron-Ion Recombination Coefficient ($m^3.s^{-1}$)</i>
β_{np}	<i>Ion-Ion Recombination Coefficient ($m^3.s^{-1}$)</i>
γ	<i>Secondary Electron Emission Coefficient</i>
α	<i>Ionization Coefficient (m^{-1})</i>
η	<i>Attachment Coefficient (m^{-1})</i>

Chapter 1

Introduction

1.1 What is Corona Discharge?

Corona is a partial discharge phenomenon that requires at least two electrodes: a sharp electrode with very small radius of curvature, usually supplied with a high electric potential which is called the corona electrode and a blunt electrode with much larger radius of curvature which is usually grounded. The partial electrical discharge, which occurs when the strength of the electric field near the corona electrode exceeds a certain critical value but still insufficient for a complete breakdown or arc is known as the electric corona discharge. In corona systems, the electric field near the sharp corona electrode has to be much larger than its value at points far from this electrode. Therefore, in contrast to a spark discharge, only a very small part of the gap between the two electrodes becomes ionized and conductive during the discharge; this is why corona is called a partial discharge phenomenon.

The corona discharge is also classified as a non-equilibrium and non-stationary low temperature plasma. This kind of plasma is unstable and small fluctuations of electron density or their temperature may cause huge quantitative and qualitative

changes in corona current. In negative corona, for example, the current may grow by nine orders of magnitude during a few nanoseconds [1].

Corona electrodes typically consist of needles (points), wires or blades connected to a high voltage power supply [2]. Some examples of different configurations used for generating corona discharge are point-to-plane, multi-point-to-plane, wire-to-plane, wire-to-cylinder, wire between two planes, and multi-wire-to-plane [3]-[5].

1.2 Features of Corona Discharge

The value of the potential at which corona starts is called the corona threshold or the corona onset voltage. At voltages close to this value, there is a region in which corona current increases proportionally with voltage. This region is called the Ohm's law regime. Above this region, the corona current increases more rapidly, approximately as a square function of the applied voltage. Increasing the applied voltage eventually leads to a complete breakdown and arcing at a point called the breakdown potential.

As the electric field near the corona electrode increases, the free electrons existing in the gas in this area are accelerated due to electric forces. When the accelerated electrons have enough energy, they create an electron-positive ion pair upon their collision with neutral gas molecules. The newly generated electrons (provided that they are close enough to the corona electrode) are accelerated and create more electron-ion pairs. Therefore, the number of electrons in the air gap increases exponentially. This process is called Townsend avalanche ionization. As the applied voltage increases further to the value of the breakdown voltage of the gas, the ionization process accelerates further into the air gap and arcing occurs. This is what happens during a lightning strike.

The electric field at which corona discharge starts depends on the ionization characteristics of the gas and the size and surface condition of the high voltage electrode. Peek [6] obtained an expression for the value of critical electric field, at which corona discharge starts on a corona electrode in dry air for highly symmetric configurations.

For over a hundred years the corona discharge has been used in industry. Since electrostatic processes often depend on availability of charge carriers [7], the main application of corona discharge in engineering devices and processes involves the electrical charging of small particles or drops [8]. Examples of devices using this phenomenon include the electrostatic precipitator of Cottrell [9], electrophotography, powder coating systems, static control in semiconductor manufacture, ionization instrumentation, control of acid gases from combustion sources, destruction of toxic compounds, generation of ozone [10], reduction of gaseous pollutants SO_x and NO_x in flue gases [11], jet printers, indoor air cleaners, and industrial processes such as the treatment of polymer films and fabrics [12].

Coronas may have unwanted effects as well. They are generally undesirable in: electric power transmission, where it causes power loss, audible noise, electromagnetic interference, purple glow, ozone production and insulation damage. Inside electrical components such as transformers, capacitors, electric motors and generators, corona progressively damages the insulation leading to premature equipment failure. Thus, power companies spend large sums of money to detect corona discharge on transmission lines and minimize their presence.

1.3 Types of Corona Discharge

Corona discharge phenomena can be categorized from different points of view:

1. Discharge current: burst pulse corona, streamer corona, Trichel pulse corona and glow corona. The specifications and characteristics of these regimes are described later in this Chapter.
2. Electrode configuration: electrode configuration has a major role in different applications of corona discharge. For example, in coating technology, where a high homogeneity is needed, point-plane configuration is used. In gas and water treatment applications, different configurations such as wire-wire, wire-plane, wire-cylinder and mesh/brush configurations have been investigated and implemented on industrial scales [13].
3. Polarity of the electric potential supplied to a sharp electrode: negative corona and positive corona.

In negative corona, a negative voltage is applied to the corona electrode. Electrons and negative ions move towards the ground plane and positive ions move towards the corona electrode. Trichel pulses only happen in negative corona and will be explained in detail in Chapter 2. In positive corona on the other hand, the applied voltage and the direction of ions movement is opposite to that of the negative corona case.

1.4 Mechanism of Negative and Positive corona

If a positive voltage is applied to a corona electrode, positive corona will be developed. In a needle-plane electrode configuration this type of corona starts with burst pulse

corona. This regime consists of random and non-regular current pulses accompanied with short and faint streamers away from the needle [14]. It then proceeds to the glow corona, streamer corona and finally spark discharge as the applied voltage increases [10]. The positive glow corona is known as the Hermstein glow [15]. This glow has a stable current at a fixed voltage, quiet operation and almost no sparking. The streamer regime is unstable, and emits audio and radio noise. It creates many thin and short duration current streamers originating from the needle. This behaviour is shown in Figure 1.1 as a brush growing [14]. The streamer regime of corona can be described as an incomplete breakdown and it is followed by a spark as voltage is increased further [10]. For a wire-cylinder or wire-plate electrode configuration, corona generated at a positive wire electrode may appear as a tight sheath around the electrode or as a streamer moving away from different parts of the electrode [10].

Negative corona starts when a negative voltage is applied to the corona electrode. For this discharge in a needle-plane geometry, the initial form is Trichel pulse corona [16]. Trichel pulses are regular current pulses with fast rise times and short duration and occur only in a negative corona discharge. These pulses are followed by pulseless corona (glow corona) and spark discharge as the applied voltage increases [10]. Negative glow corona which is the second regime in negative corona discharge develops when the electrode is clean and smooth [14]. Corona generated at the negative electrode might be either a rapidly moving glow or concentrated into small active spots, called “tufts” or “beads” [10]. The glow discharge often changes to the tuft form with time [14], a process associated with the formation of more efficient mechanisms of generating successive avalanches. The glow is made up of individual electron avalanches at close locations [10]. In static air, pulseless negative corona changes to a spark with increasing voltage. Negative corona has a higher sparking

Table 1.1: Corona discharge classification

Polarity of the electric field	Positive	Negative
Discharge current	Burst pulse corona Streamer corona Glow corona Spark	Trichel pulse corona Pulseless corona Spark
Electrode configuration	Point to plate, Wire to plate, Wire to cylinder	

potential in comparison to the positive corona; this is why negative corona is often used in electrostatic precipitators [14].

The classification of corona discharge from these different point of views is shown in Table 1.1.

Figures 1.1 and 1.2 show different types of corona discharge from the discharge current point of view [17].

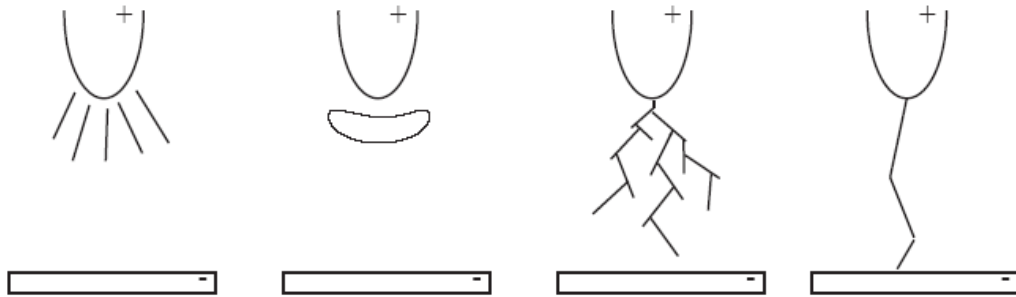


Figure 1.1: Types of positive corona discharge, from left: burst corona, glow corona, streamer corona, spark discharge.

1.5 Thesis Objectives

In summary, the objective of this thesis is to present a numerical technique which can predict the mechanism of the Trichel pulse regime of negative corona discharge. Of

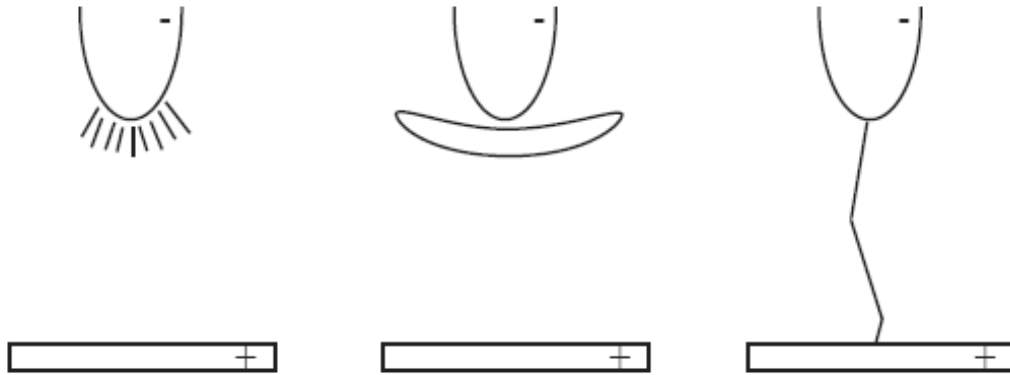


Figure 1.2: Types of negative corona discharge, from left: Trichel pulse corona, pulseless corona, spark.

particular interest is what happens to the magnitude and distribution of the electric field and charge species during this process and how they behave. This technique should be able to produce results compatible with available experimental data. The main objectives of this thesis are as follows:

To present an applicable model for simulating the Trichel Pulse phenomenon found in negative corona discharge in point-to-plane configuration in oxygen and air:

Many researchers have worked in the corona discharge modelling area. However, their presented models are mostly single-species (only one charge carrier is assumed in the air gap and other species are neglected), static (the time dependency of the corona discharge phenomenon is approximated by a static model) or one-dimensional (1D) (while the true nature of the problem is 3D, but symmetrical around the axis, i.e., 2D). A single-species model might be useful for some engineering applications where a simplified model suffices. However, it does not help with understanding the microscopic behaviour of charge carriers during corona discharge. Moreover, single-

species models fail, if a good estimate of corona discharge behaviour is required. Therefore, presenting a model which can accurately predict the physical behaviour of corona discharge has still been missing. In this thesis, a dynamic, three-species, 2D model for predicting the mechanism of the Trichel pulse regime of corona discharge is presented.

To present a numerical technique for solving the model:

The corona discharge is a very complicated phenomenon for which an analytic solution is not available. Also, the governing equations for modelling the behaviour of charge carriers are not easily solvable. Therefore, presenting a technique which can deal with the nonlinear hyperbolic equations modelling this problem is very desirable. To date, many numerical techniques have been presented for solving the hyperbolic equations of charge transport. Of these a combined Finite-Element-Method (FEM) and Flux Corrected Transport (FCT) technique has proved to be the best one for dealing with these classes of problems. However, numerical implementation of this technique is very complicated and needs some modifications for a specific type of problem. In this thesis, a FEM method is used for solving the Poisson equation and a combined FEM-FCT technique is proposed for solving the charge transport equations.

To compare the simulation results with the experimental data:

A good measure of the reliability of the model would be a good agreement of its predicted results with the experimental data. For this reason, the presented model and the numerical results obtained from it are compared with selected experimental data. The compatibility of the results shows that this model is a good approximation of the reality.

In this thesis, after investigating different models presented for the simulation of Trichel pulse corona in air, the most complete 2D dynamic model is chosen; a numerical technique is developed for solving this model and the numerical predictions are compared with the available experimental data presented by other researchers.

To investigate the effect of different parameters of the model on the corona characteristics:

Some of the parameters used in modelling negative corona discharge differ widely in the literature and various values are used in different papers. Since knowing the effect of these parameters on the Trichel pulse characteristics is important, the effect of parameters such as external resistance, mobility, air pressure, and the secondary electron emission coefficient are investigated in this thesis and the observations are reported.

1.6 Thesis Outline

This thesis is divided into eight Chapters. A summary of each Chapter follows.

Chapter 2: This Chapter focuses on explaining the mechanism of negative corona discharge in Trichel pulse regime. It also reviews the literature related to the Trichel pulse regime of corona discharge, mentions the deficiencies of these models and explains the motivation of this work.

Chapter 3: This Chapter's focus is on the numerical techniques proposed for modelling corona discharge. First, a comprehensive review on the numerical techniques used by the researchers for solving different equations governing corona

discharge is presented. Secondly, the numerical techniques selected in this thesis are explained in detail. FEM is used for the electric field computations and the FEM-FCT technique is used for the space charge density calculations.

Chapter 4: In this Chapter, the complete set of equations for modelling the Trichel pulse regime of corona discharge is presented and the solution methodology is explained. Moreover, the numerical problems faced during the course of this work are presented. The suggested solutions for these problems are presented along with several techniques used for optimizing the code.

Chapter 5: In this Chapter, a numerical algorithm for the dynamic simulation of corona discharge in air, assuming single species charge carriers is proposed. The simulation results show the behaviour of corona current and space charge density under two waveforms of the applied voltage: step and pulse.

Chapter 6: In this Chapter, which is the main Chapter of this thesis, Trichel pulses are numerically reproduced. The mechanism of these pulses is explained by discussing in detail field and charge behaviour during these pulses. It is assumed that three ionic species exist in the air gap: electrons, and positive and negative oxygen ions.

Chapter 7: In this Chapter, effects of different parameters of the model on Trichel pulse characteristics (i.e., Trichel pulse period and the average corona current) are studied. The parameters of interest are: external resistance of the circuit, secondary electron emission coefficient, and negative and positive ion mobilities.

Chapter 8: In this Chapter, numerical results are compared against two sets of available experimental data and the compatibility of numerical and experimental results are shown as a proof for the suitability of the model.

Chapter 9: In this Chapter, the data required for modelling the Trichel pulse regime of corona discharge in oxygen is presented. A series of Trichel pulses are simulated in oxygen as well.

Chapter 10: This Chapter summarizes the results found in the thesis. Some suggestions for future studies on this subject are also presented.

Chapter 2

Negative Corona Discharge

2.1 Mechanism of Trichel Pulse Corona Discharge

Electronegative gases are gases which have affinity for electrons. These gases are characterized by one or two electrons deficient in their outer shell [18]. Oxygen, water vapour, and carbon dioxide are several common examples for electronegative gases [12]. The gases that do not have the affinity for electrons are called free-electron gases [18]. Nitrogen, hydrogen, helium, and argon are several examples of free-electron gases.

In electronegative gases (also electropositive gases under very specific conditions), the first regime of negative corona is Trichel pulse corona. This regime is followed by pulseless corona (glow corona) and spark discharge as the applied voltage increases. It was supposed that in a non-electronegative (free-electron) gas like nitrogen, current is continuous without pulses; however, Akishev et al. [19], [20] have recently determined that a regular pulsed regime similar to Trichel pulses can be observed in Nitrogen as well, but under very specific conditions.

If the negative voltage applied to the corona electrode is larger than the corona onset voltage¹, a very large electric field appears near the corona electrode. If this electric field exceeds the critical value required for the ionization of the gas, the corona discharge is initiated. The threshold value for the electric field depends on factors such as wire radius, the roughness of the wire, ambient gas temperature and pressure [12].

In the area between electrodes there are always some seed electrons (20 electron-ion pairs/cm³ per second at atmospheric pressure) which are created due to cosmic radiations and other phenomena. When the electric field is large enough, these seed electrons are accelerated and upon colliding with neutral molecules, detach electrons from these molecules leaving positive oxygen ions. In a very short time a very large number of electrons and positive ions is created in the ionization layer². This process is called avalanche ionization.

Since beyond the ionization layer electrons do not have enough energy to detach electrons from the neutral molecules, this process stops at the edge of the ionization layer.

Free electrons may also attach to neutral molecules of the electronegative gas and create negative ions. This attachment process happens in both the ionization and drift region³. Recombination between positive ions and electrons or between

1. The voltage at which the electric field on the corona electrode is equal to the Peek's value

2. The region in which the electric field can accelerate electrons to the speed at which they can detach electrons from the neutral molecules

3. The region at which the ionization reaction does not happen. This region is much larger than the ionization layer

positive ions and negative ions are some of the other ionic reactions occurring in the air gap. Recombination results in the reduction of the number of ions and electrons. The secondary electrons which sustain the discharge have three different sources: photoemission from the discharge electrode, collision of positive ions with the corona electrode surface and photoionization in the gas [21].

There are two distinct regions in the corona discharge [22]. In the vicinity of the corona electrode, in which avalanche ionization occurs due to the collision of highly accelerated electrons with neutral molecules, an ionization layer exists. In most cases, this layer is less than a few millimetres around the electrode [22]. A larger region which is called the drift region is the region which is mostly filled with ions of the same polarity as those of the corona electrode. In the ionization layer, ionization prevails over attachment. Beyond the ionization layer the electric field decreases gradually and electrons do not have sufficient energy to ionize the gas molecules. Therefore, the avalanche ionization stops and the number of electrons decrease gradually in the drift region. Since beyond the ionization layer and in the drift region, there might be some electrons with sufficient energy for the ionization of gas molecules, some authors assume another layer, called the plasma layer, which is a region starting from ionization boundary and extends a few millimeters into a drift region. Davidson [12] has defined this region as the corona plasma region, in which corona-enhanced chemical reactions are possible and its radius is the radius at which the reduced field E/N (where N is the density of neutral molecules) equals 80 Td. At this value the mean kinetic energy of electrons is 1.85 eV and some electrons are energetic enough to cause electron-impact ionization. Figure 2.1 shows the schematic explanation of negative corona discharge in a point-plane geometry.

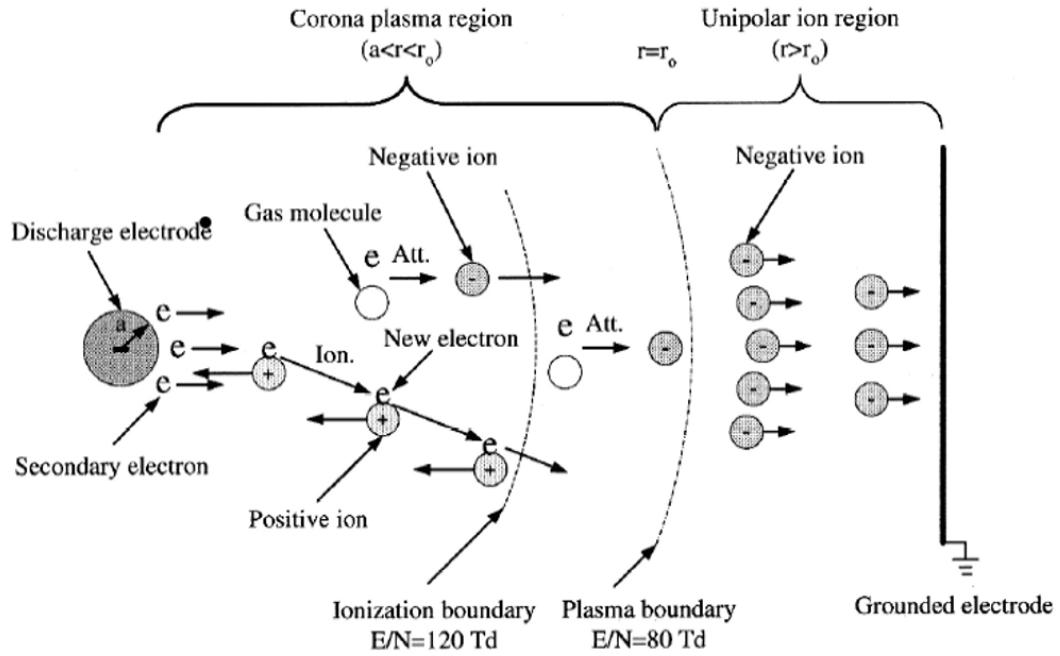


Figure 2.1: Ionic reactions in corona discharge. The scaling is not accurate.

Subsequent to the avalanche ionization, a cloud of positive ions is created close to the corona electrode in the air gap. In a very short time, the attachment also creates a cloud of negative ions just outside the ionization layer. This formation of ionic clouds causes the increase of electric field between the positive ion cloud and the corona electrode, decrease of electric field between the two clouds and increase of electric field between the negative ion cloud and the plane as shown in Figure 2.2.

The increase of the electric field in the ionization layer increases the avalanche ionization in this area which causes a very fast build-up of the corona current. As soon as the negative ion cloud is created, the ionization layer is shortened and the avalanche ionization is limited to region (I). The positive ions then move towards the corona electrode due to their opposite polarity. Therefore, the current reaches a maximum value and as soon as the process of deposition of positive ions on the

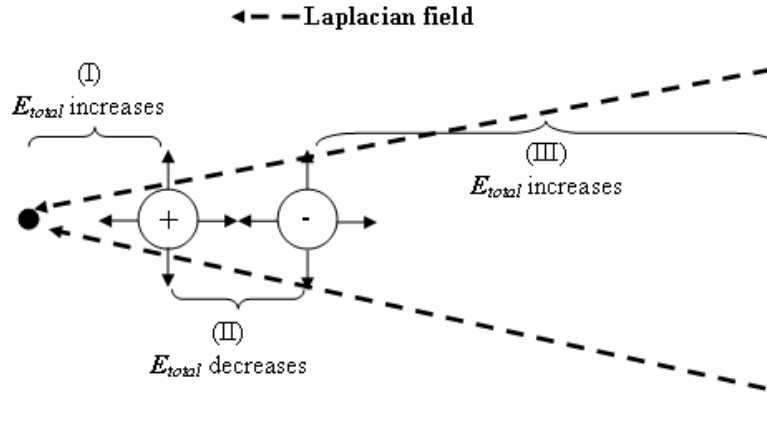


Figure 2.2: Electric field in different regions during Trichel pulse corona discharge, the circles represents the ion clouds.

corona electrode starts, the corona current's value decreases.

The maximum of corona current occurs when the total number of positive ions in the space is largest. At this moment the avalanche ionization has not stopped yet. For a short time after the maximum of the pulse, avalanche ionization still occurs. Therefore, the total number of electrons in the space still increases after the Trichel pulse. However, since the positive ions are being deposited on the corona electrode and the deposition rate is larger than the generation rate, the number of positive ions decreases with time.

The negative ion cloud finally chocks off the electron avalanche and the ionization process stops completely. After this step, the attachment processes is the only reaction which increases the total number of negative ions in the air gap after the pulse.

Negative ions move towards the ground electrode due to the electric force and are being deposited there. Since the mobility of negative ions is small and they have a long distance to travel (in contrast with positive ions), this deposition process is very slow and takes a long time (in comparison to the rise time of the Trichel pulse). As soon as negative ions start being deposited on the ground, the total number of negative ions in the air gap decreases. Once enough negative ions are deposited on the ground plate and they disappear from the space, the electric field near the corona electrode increases again and everything gets ready for the next pulse to appear. Right before the next pulse, the secondary electron emission creates a sufficient amount of electrons required for the avalanche ionization of the second pulse.

In wire-plate or wire-cylinder configurations, negative corona appears in a form of discrete tufts or beads along the wire [10]. These tufts are randomly spaced along the wire and their number is dependent on the applied voltage. As the voltage increases, the number of tufts increases too and they become more uniformly spaced [12].

2.2 Ionic Reactions

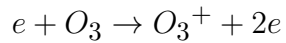
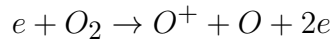
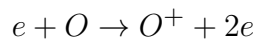
Fifty reactions and twelve ionic species exist in the electric corona discharge in oxygen. More reactions and species appear during corona discharge in air. Since including all these species and reactions needs a large memory and a very powerful processor, the number of reactions and species that the model includes should be limited. The list of ionic reactions for the corona discharge in oxygen can be classified into five categories [22], [23]. These categories along with several examples for each of them are presented below.

2.2.1 Ionization

In gas discharge, ionization is defined as the process of liberating an electron from a gas particle with either the simultaneous production of a positive ion or with the increase of positive ion charge [18]. There are various ways for the creation of positive ions:

- Electron collision
- positive ion collision
- radiation: light, X-ray, nuclear
- thermal ionization
- excited atoms
- chemical and nuclear processes

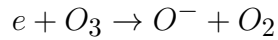
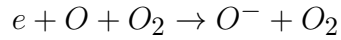
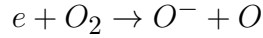
Some equations that show the ionization process in oxygen are shown below:



2.2.2 Attachment

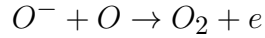
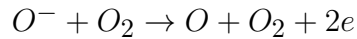
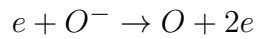
There is a tendency of capturing free electrons by atoms lacking one or two electrons in their outer shell.

The process of attaching free electrons to neutral atoms and molecules and the formation of negative ions is called attachment. Here are some examples for attachment in oxygen:



2.2.3 Detachment

The process of detaching electron from neutral molecules or negative ions is called detachment. Some examples for this process are:

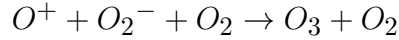
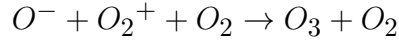
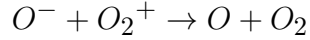


2.2.4 Ionic Recombination

Recombination or neutralization is the combination of a positive ion with either a free electron or an excessive electron of a negative ion. This process is a major cause of the decrease in charged particle numbers.

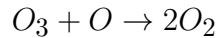
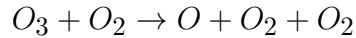
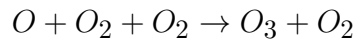
Experiments proved that the probability of the recombination of a positive ion and a negative ion is larger than the probability of the recombination of a positive ion and an electron [18]. This process can be explained considering the velocity of electron. Since an electron approaching the positive ion is usually too fast and the time of interaction between these two particles is very small, the probability of capturing an electron by the positive ion is very small. Therefore, the recombination

between electron and positive ions occurs only for very slow electrons. Here are some examples for recombination processes:



2.2.5 Ozone Generation and Decomposition

Disinfection, bleaching and chemistry are three domains in which ozone has expanding applications. In water purification applications, ozone is used extensively as a substitute for chlorine. Electric corona discharge is the best technique for creating ozone. This technique has been investigated for a long time and is now largely industrialized. The following equations show the processes causing ozone generation and decomposition in oxygen.



As mentioned earlier, including all these species and reactions makes the corona model too complicated. Therefore, considering the specific application of corona and the information needed, only some of these species should be considered in the model.

If the charge density distribution of electrons and negative and positive oxygen ions are required, the three species model which only includes the reactions between e , O_2^+ , O_2^- should be studied. This model is also sufficient for the reproduction of Trichel pulses and is used in this thesis as well. However, if the application involves

ozone generation and its generation rate is required, five species model which include the reactions between e , O_2^+ , O_2^- , O_3 , O should be investigated.

2.3 Literature Review

The Trichel pulse regime of corona discharge which is the first regime in negative corona is an interesting phenomena from both scientific and industrial points of view. Trichel pulses are normally very regular pulses with very short rise times (as short as 1.3 ns [24]) and short durations (tens of nanoseconds [25]) separated by much longer inter-pulse periods (tens of microseconds [25]). Trichel reported the existence of such pulses in oxygen [16] and was able to explain some very important features of the corona discharge like the shielding effect produced by the positive ion cloud near the cathode. He also predicted that the space charge formation and subsequent clearing in the gap is the cause of the periodic character of the discharge. A negative cloud of space charge is formed far from the discharge electrode (point) and a positive cloud is formed near the point. The presence of positive ions near the point increases the field in this area and decreases the electric field between the positive and the negative ion clouds. Therefore, no ionization can take place beyond the positive ion cloud. The positive ions move towards the point under the effect of the electric force; this narrows the region of the enhanced electric field and, finally, the ionization process stops.

It was also observed that the frequency of pulses varies linearly with the corona current and is a function of the point diameter varying as an inverse function of the radius of the point for the same corona current. The frequency of the pulses is not a function of gap length, but varies with current independently of gap length [26].

Loeb et al. [27] believed that these regular pulses exist only in electronegative gases. This assumption contradicts the recent discovery of Akishev et al. [19]. They tried to explain this phenomenon by presenting a theory which involved successive electron avalanches, each giving rise to three successors near the end of its development but this theory could not explain the fast rise time of 1.5ns observed in air at atmospheric pressure.

Zentner 1970 [24] found that the rise time of the pulse in air may be as short as 1.3 ns. He also observed a step on the leading edge of the current pulse.

Lama and Gallo [26] carried out a series of carefully designed experiments and determined the dependence of pulse frequency, charge per pulse and time averaged corona current with the applied voltage, needle tip radius, and needle to plane spacing. They further explained the physical mechanism proposed by Trichel and Loeb, by adding a very rapid electron Townsend avalanche from the tip, followed by electron attachment to electronegative molecules to form a slow moving negative ion cloud that reduces the electric field below threshold and thus chokes the discharge. The corona discharge then remains off until the negative ion cloud drifts sufficiently far from the tip causing the electric field to rise above threshold and the discharge re-initiates. This is repeated in successive stages leading to Trichel current pulses. Lama and Gallo analyzed the electric field and characterized the discharge in terms of several parameters as follows defined in terms of applied voltage, gap spacing and tip radius:

- “Transit time”: the time for a negative ion cloud to transverse the gap.
- “Clearing length”: the distance the choking negative ion cloud must move before the electric field regains its breakdown value and the corona discharge

re-initiates.

- The number of negative ion charge clouds in the gap at any given time, particularly as a function of applied voltage.
- The total value of negative ion charge in the gap at any given time, particularly as a function of applied voltage.

By incorporating experimental data into the expressions for the space-charge-free electric field, Lama and Gallo were able to obtain equations for the complex space-charge perturbed situation. These equations remain to be verified by independent analysis. Depending upon applied voltage, their major conclusion is that there are many negative ion charge clouds simultaneously in transit across the gap.

Aleksondrov [28] presented the theory of parallel development of several avalanches rather than successive avalanches. He therefore succeeded in predicting much faster rise times for the main pulse. Kekez et al. [29] used an equivalent circuit for the point-to-plane corona discharge and described the succession of pulses. However, his model could not explain the detailed mechanism of the pulse formation.

In 1985, Morrow [30], [31] proposed a one-dimensional model for the development of Trichel pulses by applying the combined Finite-Difference and Flux-Corrected Transport (FCT) technique to solve the set of continuity equations for ionic species along with Poisson's equation for electric potential. He could only predict the first Trichel pulse and offered a theoretical explanation for the different stages of the pulse. His work was the best-known among all the attempts for theoretical explanation of the Trichel pulse phenomenon. The results agreed well with the experimental data on the current-voltage dependency and also on the dynamics of the pulse initiation.

However, the extension of the calculations to longer times showed only continuing decay of the current without subsequent pulses. Although Morrow did explain the different stages of the pulse, he ignored the ion secondary emission.

Atten et al. [32] investigated the process of corona discharge in air at different gas pressures and point radii. They showed that the Paschen's law is still valid in high pressure air (up to 7 MPa) for very small point electrodes.

Castellanos et al. [33] proposed a three species model to study corona discharge in oxygen at a reduced pressure (50 Torr). They solved the problem in 1D using a Particle-in-Cell technique. Their results were compared with experimental data, but the model they were using was valid for oxygen and at a reduced pressure while the experimental data was reported for air and at atmospheric pressure [26]. Moreover, the investigated geometry was different from that of experiment. Therefore, they did not expect a quantitative agreement between experimental and numerical results. Still their model and technique had some advantages; it was fast and they could obtain a reasonable agreement between the characteristics of Trichel pulse in simulation and experiment.

Napartovich et al. [34] proposed a quasi-one-dimensional, 1.5D, numerical model for the analysis and reproduction of Trichel pulses. This means that they assumed a constant distribution for all the physical quantities (charge densities and electric field) in every cross section of the discharge channel. The same approximation was made by Morrow but he assumed a cylindrical shape for the discharge channel. However, experimental observations show that the ratio of the discharge channel on the anode and cathode is on the order of 10^4 . They assumed that the radius of the current channel is a function of the axial distance, x . With this assumption, they

could model the sequence of Trichel pulses in dry air for short gaps ($< 1\text{cm}$).

The same authors later presented a two-dimensional model for negative corona discharge in air and successfully showed the presence of a sequence of Trichel pulses [35]. This paper, however, did not contain any detail on the technique and the model used. Some other authors used similar simplified models in order to reproduce sequences of Trichel pulses [29], [36] and [37].

Georghiou et al. [38] presented a two-dimensional model for Trichel pulse simulation in air. They used COMSOL-Multiphysics (a FEM based commercial software) for solving the corresponding equations. Their results, however, were not compatible with experimental expectations. The period of the Trichel pulses they calculated was approximately 20 times smaller than the experimental predictions for the same configuration.

2.4 Motivation

The Trichel pulse regime of negative corona discharge is a very interesting and unique phenomenon. From the physical point of view, in the Trichel pulse regime, a pulsating current will appear in the air gap if a DC voltage is applied to the sharp electrode. In practice, there are many industrial devices which use negative corona discharge: electrostatic precipitators, electrophotographers, ozone generators and ionizers are some examples of these devices. Optimizing these devices needs a deep understanding of the mechanism of the corona discharge. Therefore, presenting a model for the Trichel pulse regime of corona is an interesting subject among both physicists and engineers.

As mentioned in the literature review, none of the existing models proposed for modelling this phenomenon are either comprehensive or compatible with the experimental data. Therefore, a model for simulating Trichel pulse regime of corona discharge will be proposed in this thesis. The proposed model improves the existing models and has the following features simultaneously:

- it is three-dimensional
- it can simulate the dynamic behaviour of Trichel pulses
- it includes three ionic species and it can be easily modified to include a larger number of species
- it is the first proposed model which shows a reasonable correlation with the experimental data published by other researchers.

2.5 Conclusions

In this chapter, a detailed description of the mechanism of negative corona discharge was presented and the literature related to Trichel pulses was reviewed.

The literature review has identified some specific deficiencies in the understanding and explanation of Trichel pulses which justifies the motivation for this project.

The purpose of this thesis is to clarify our understanding of the Trichel pulse mechanism. The interest in doing this is certainly because corona is important in many practical applications but more importantly to fill in gaps of understanding that exist. The goal of producing a model and numerical solution that helps in this

understanding by improving on existing models and correlates better with existing experimental data is certainly a worthy topic of an engineering study.

Moreover, due to a very large number of industrial applications of corona discharge, in-depth knowledge of corona characteristics, their transition to arc and their chemical interactions with the environment are essential for further progress in this field. Understanding the mechanism of corona helps with optimizing the industrial devices which use corona discharge.

Chapter 3

Mathematical Models and Numerical Algorithms in Electric Corona Simulation

3.1 Introduction

Due to the complexity of equations governing corona discharge, finding analytical solutions for these equations is not possible unless some major simplifications are made or the problem geometry is highly symmetric. Therefore, numerical simulation is principally the only feasible approach for the corona discharge modelling.

The use of numerical tools for studying this phenomenon has recently reached an advanced degree of development. Different types of numerical techniques have been used for modelling this interesting and complicated phenomenon. However, there is still no complete and stable algorithm for modelling the Trichel pulse regime of corona discharge.

The equations describing the electric field and space charge density used in modelling corona discharge can be treated as a simultaneous set of partial differential

equations. The charge density distribution is unknown in advance due to its dependence on the electric field. On the other hand, the field distribution is a function of charge density. Therefore, the solution of these equations can not be found easily and both problems are mutually coupled.

In order to simulate electric corona discharge numerically, most researchers use iterative techniques. Electric field and space charge density are solved iteratively until convergence is obtained. This approach allows the use of different methods to independently compute both distributions.

3.2 Literature Review on Mathematical Models for the Trichel Pulse Simulation

First attempts on modelling of the Trichel pulse regime of negative corona discharge were made by Morrow [30]. Three charge continuity equations along with the Poisson equation were solved for calculating the distributions of electrons, positive and negative ions, and electric field at reduced pressure oxygen (50 Torr). His model was 1D and included the three main reactions occurring in corona discharge: electron ionization, attachment, and recombination (electrons-positive ions and negative ions-positive ions). He also included both secondary electron emission and photoionization as the source of secondary electrons. However, his model could only predict the first Trichel pulse and the sequence of Trichel pulses could not be simulated.

Napartovich et al. [35] proposed a 2D mathematical model for simulating Trichel pulses in air. The same set of equations as in Morrow's case was proposed. The differences between both models were as follows:

1. ambient gas: air versus pure oxygen,
2. gas pressure: 1 atm versus 0.066 atm,
3. recombination coefficient between negative and positive ions and photoionization effect were ignored in the Napartovich model.

These authors were apparently successful in reproducing the sequence of Trichel pulses. However, the numerical technique they used was never reported. Moreover, their results were not compared with any experimental data.

Castellanos et al. [33] used Morrow's 1D model in oxygen (at reduced pressure) to reproduce the series of Trichel pulses. They ignored the photoionization, diffusion and recombination effects but investigated the voltage range at which stable Trichel pulses can be generated. However, their model was 1D and such models are too simplistic for accurate estimation of the Trichel pulses behaviour.

Georghiou et al. [38] used a 2D model to produce a Trichel pulse sequence in air. They were successful in simulating the sequence of pulses but their results were not comparable with the experimental observations reported in literature.

3.3 Literature Review on the Numerical Techniques

In this section, different techniques used for solving electric field and space charge density equations along with the algorithms used for modelling corona discharge are presented.

Table 3.1: A comparison between differential-based and integral-base techniques

Methods	Differential-based	Integral-based
Discretization	Whole domain	Boundaries, interfaces and areas with space charge
Suitable for	Laplacian or Poissonian Linear or nonlinear	Laplacian problems Open boundary problems
Not suitable for	Open boundary problems	Poissonian or nonlinear problems

3.3.1 Numerical Techniques for Calculating the Electric Field

In gas discharge problems, the Poisson equation needs to be solved to calculate the electric potential as well as the electric field. To date, many different techniques have been proposed for solving this equation and can be classified into two different categories: integral-based and differential-based.

Boundary Element Method (BEM) and Charge Simulation Method (CSM) are two examples of integral-based techniques; Finite Difference Method (FDM), Finite Element Method (FEM), and Finite Volume Method (FVM) are examples of differential-based techniques used for solving this equation. A brief comparison of these two categories is shown in Table 3.1.

The first proposed technique for calculating the electric field was FDM [39]. In this technique, the derivatives in the partial differential equation are replaced with finite differences. The whole region is discretized and a mesh is formed. The finite difference approximation is then applied to every node of a mesh. As a result, the differential equations are transformed to linear algebraic equations. Simplicity of this technique is one of the advantages of FDM; however, since this technique needs a rectangular mesh, it is difficult to apply FDM to problems for irregular domains. For problems with complicated geometry, FDM must use a large mesh which will be time

consuming. Another disadvantage of this technique is that it can not handle the sharp geometry of the discharge electrode very well [39]; therefore, using this technique for modelling corona discharge is not recommended.

FEM was the next proposed technique and eventually it became a dominant technique for solving Laplace and Poisson equations [40]-[43]. FEM is based on minimizing the energy of the system instead on direct solution of the equations. Therefore, it can determine the energy related parameters with a much better accuracy. To use FEM, the whole domain should be discretized into a set of triangular, quadrilateral or other type of elements depending on the problem configuration. A simple matrix equation for each element is then obtained by minimizing a properly formulated functional, which can be obtained from the variational principle. By assembling these matrix equations, a global set of algebraic equations can be formulated. After introducing the boundary conditions, this global set of equations is solved to obtain the values of the unknown functions at each node. A detailed description of this technique will be presented later in this Chapter.

The advantage of FEM over FDM is its ability in solving problems with complicated configurations. It can use unstructured grids as compared with structured grids required for FDM which results in a smaller mesh and makes the calculations less time consuming. By increasing the number of elements or the order of interpolating polynomials in each element, accuracy of the technique can be easily improved.

Singer and Steinbigler [44] introduced CSM, the first integral-based technique for the calculation of high voltage fields and applied it to two and 3D fields with rotational symmetry. Since then, many refinements to the original method have been proposed by Horenstein [45], Castle [46], Malik [47] and Elmoursi [48], and the CSM

has been successfully used to solve a variety of field problems.

This technique is based on the fact that the electric field in a considered domain can be uniquely determined by the problem boundary conditions. Therefore, the original problem can be replaced by introducing a set of fictional charges that match the boundary conditions. In this technique, some number of point charges are used instead of continuous surface charge density on electrodes [47]. Values of the discrete charges are determined in order to satisfy the boundary conditions of the original problem. Knowing the values and positions of these substitute charges, the potential and field distribution can be easily computed anywhere in the region. If the charges are set properly by the user, CSM can be fast and accurate. However, since there is no specific rule for setting these charges, finding their best number, value and location is not easy. This technique is not suitable for problems with complicated geometries or in the presence of several different materials in the domain.

BEM was the next integral-based technique proposed for solving the Poisson equation [49]-[52]. Similarly to CSM, BEM introduces a set of field sources but they are located on the boundaries. These sources are selected so that the continuity and boundary conditions are satisfied. The advantage of BEM over CSM is that in BEM the charges are on the surface of the electrode while in CSM the user should locate the charges somewhere inside the electrode and the accuracy of the technique is dependent on these locations. The main disadvantage of BEM is that it is time consuming for problems with space charge and it is impossible to use it for non-linear problems.

FVM is a more recent technique, proposed for corona discharge problems [52]. This technique also converts partial differential equations into algebraic equations.

Similarly to the FDM, values of unknown solution are calculated at discrete nodes of a mesh. “Finite volume” refers to the small volume surrounding each node. In the FVM, the volume integrals in a partial differential equation containing divergence terms are converted to surface integrals using the divergence theorem. These terms are then evaluated as fluxes at the surfaces of each finite volume. Because the flux entering a given volume is identical to that leaving the adjacent volume, these methods are conservative. Another advantage of the FVM is that it can be easily formulated for both structured and unstructured meshes. This method is used in many computational fluid dynamics packages.

Since each of these techniques has its own advantages and disadvantages, it is useful to combine different methods in one algorithm. The integral-based and differential based techniques have some complementary characteristics; therefore, hybrid techniques which take the advantage of the individual techniques are proposed by many researchers. As an example, combination of BEM-FEM is used by Adamiak and Atten [53]. In their approach, FEM was used to calculate the Poissonian and BEM the Laplacian components of the electric field.

3.3.2 Numerical Methods for Calculating the Space Charge Density

The space charge density distribution in corona discharge can be determined from the charge continuity equation. This equation is hyperbolic and nonlinear. The space charge density also depends on the electric field and the electric field depends on the space charge. This mutual dependence makes the solution complicated.

The Method of Characteristic (MoC) is one of the most popular techniques for

solving the charge continuity equation. In this technique, it is assumed that ions move along electric field lines called the characteristic lines. Along these lines, the partial differential continuity equation for the space charge density changes to ordinary differential equations (ODE). These ODEs can be integrated and an analytical or numerical solution for charge density can be obtained. If the initial charge density at the first point of each characteristic line is known, the charge density at any point in the space along the characteristic line can be easily calculated. However, this technique has an important disadvantage. It is simple for a single-species problem only. It is difficult to extend this technique to problems with multi-species ions since a set of ordinary differential equations must be solved numerically [54]. Moreover, for the problems in which diffusion plays an important role, MoC is not suitable at all.

The Finite Volume Method, especially in the form called the Donor-Cell Method (DCM), is another technique used for solving charge continuity equations. This technique uses the charge conservation equation in the integral form [55] and the computation region needs to be meshed so that each node should be surrounded by a polygon. The advantage of this technique over MoC is that it can solve multi-species problems and it can take into account the ion diffusion. The disadvantage is that it can be very time consuming [56]. Therefore, for single-species modelling MoC is preferred over DCM.

Combination of FEM with Flux Corrected Transport (FCT) technique is another useful technique for solving charge continuity equations. This technique has been proposed by Morrow and others [30], [57] and [58], who successfully applied it to solve the charge continuity equation. The advantage of FEM is that it can be applied to unstructured grids which leads to a smaller algebraic system and makes

the calculations faster. FCT removes the non-physical (numerical) oscillations usually introduced by conventional FEM schemes. This is done by adding adequate diffusion but only to the nodes where results are oscillatory. Another advantage of this technique is that there is no need to regenerate the mesh at each iteration or to interpolate charges which is necessary in MoC [59] and [60]. This technique can also be easily used for multi-species time domain modelling.

3.3.3 Numerical Algorithms for the Simulation of Corona Discharge

All of the numerical algorithms that have been proposed for the simulation of corona discharge can be classified into two groups: simple and hybrid. In simple algorithms, the same technique is used for the calculation of electric field and space charge density while the hybrid techniques take the advantages of two or more numerical methods simultaneously.

FDM was the first technique used for solving both Poisson equation and charge transport equation [61]. FEM was then applied by Janischewskyj and Gela [62] for modelling corona discharge in between two coaxial cylinders and used for solving both equations. The coaxial cylinder configuration, due to its high degree of symmetry, reduces to a 1D model for which the analytical solution is available and can be used as a reference. The computer program prepared for their study was the skeleton model for application in 2D situations. Feng [63] combined Galerkin FEM in computing steady-state unipolar corona discharge in 2D geometry. In this work, a set of non-linear algebraic equations for steady state electric field and space charge was solved simultaneously using the Newton technique for all unknowns.

Hybrid techniques are the second option, which can be employed for solving corona discharge problems. By combining different methods to solve electric field and space charge density equations, it is possible to benefit from the advantages of each technique while mitigating their disadvantages.

Abdel-Salam [64] used the combination of FEM and CSM to model the corona discharge in a wire-ground geometry. He used the same iterative technique which was proposed by Janischewskyj. Then, he calculated the power loss along the transmission lines due to the corona discharge [65]. Takuma et al. [66] also used the combination of FEM and CSM to calculate the electric field and the upwind FEM to find the space charge density distribution for the simulation of corona discharge in the wire-plane configuration.

Davis and Hoburg [40] combined FEM with MoC to study the corona discharge in the wire-duct electrostatic precipitators (ESPs). FEM was used to calculate the electric field and MoC was used for the calculation of the space charge density.

Butler and Hoburg [67] also used a hybrid FEM-MoC approach to model corona discharge. A general purpose technique was suggested which can be used for a wide variety of geometries. The most critical element of this algorithm is a coupling between both techniques. Since FEM calculates the electric field on mesh nodes and MoC calculates the space charge density along the characteristic lines, with these two sets of nodes, which are not the same, a technique should be adopted to interface them. Two techniques were suggested for providing an interface between FEM and MoC. The first technique used the nodes of the characteristic line to regenerate a new FEM mesh after every iteration which can be used for problems with simple configuration. The second technique traced the characteristic lines from every FEM

mesh node backwards to the starting point on the corona electrode and requires much longer computing time.

Al-Hamouz [68] proposed a new method for combining FEM and MoC which made it possible for the characteristic lines to follow the FEM mesh pattern. To do this, special flux tubes were introduced which started at the surface of the discharging wire and terminated at the ground plates. The space charges were assumed to flow along the centers of these flux tubes, i.e., the field lines. Therefore, the characteristic lines could follow the FE grid pattern and there was no need for generating a new mesh at every iteration. This technique was simple but it needed a fine mesh in order to reach convergence.

Elmoursi and Castle [46] used the combination of CSM and MoC for electric corona discharge simulation in wire-plane geometry. CSM was used for the electric field and MoC was used for the space charge density calculations.

Levin and Hoburg [43] applied a combination of FEM and DCM to simulate the corona discharge in a wire-duct precipitator. FEM was used for the electric field calculation and DCM was used for the space charge density calculations. This technique was very time consuming but could include ion diffusion into the calculations.

Adamiak [49] used a combined BEM and MoC technique for the simulation of electric corona discharge in the wire-duct electrostatic precipitators. The proposed technique was reliable but time consuming.

Adamiak and Atten [53] used the combination of BEM, FEM and MoC for the simulation of positive corona discharge in the point-plane configuration. The electric field was divided into two components: Laplacian and Poissonian. BEM was used

to solve the Laplace equation which governs the distribution of electric field due to the external voltage. FEM was used to solve the Poisson equation which governs the electric field produced by space charge and MoC was used for the space charge density calculation. To obtain a good accuracy, the discretization of the area near the tip should be very fine because the variation of electric field near the tip of the corona electrode is very steep.

Atten et al. [69] combined FEM, FVM, and MoC for the simulation of electric corona discharge. They used FEM for the electric field calculation and the combination of FVM and MoC for the space charge density calculations.

The above techniques were applied for modelling a steady-state single-species corona discharge. Very few attempts have been made for modelling transient and/or multi-species corona discharge.

Mengozi and Feldman [70] developed a 1D time-dependent model of Trichel pulse development in a wire-cylindrical geometry. This model was simplified to avoid large-scale computations and only considered 2-5 μs energization pulses producing a single ionizing burst. Sekar [71] modeled the pulse corona discharge in a wire-cylinder geometry using the idea of charge shells. It was assumed that under Kaptzov's hypothesis, discrete charge shells were liberated during pulse discharge. Salasoo et al. [72] simulated corona in both space and time for a pipe type precipitator. Their model could estimate ion densities and field distribution for various pulse parameters.

Buccella [73] proposed a 2D dynamic model to predict the V-I characteristics of a duct-type electrostatic precipitator operating under pulse energization. She utilized an implicit-explicit finite difference time domain method (FDTD). The electrostatic

precipitator model was divided in two distinct parts: one that is valid during the pulse-on period and uses the wave equation to calculate the electric field distribution in the inter-electrode region, and the second is valid during the pulse-off period and uses the continuity equation to calculate the space charge drift. The comparison of the results with the experimental data showed a satisfactory agreement.

Meroth and others [74] presented a numerical model which was based upon a FEM for solving the Poisson equation and a non-stationary higher-order upstream finite volume scheme on unstructured grids for the charge transport equation. However, they assumed a model free of ion diffusion.

Liang et al. [75] proposed a method for modelling a wire-cylinder ESP under nanosecond pulse energization. They included dust loading in their model and studied the interactions between ion space charge and particle charging and their influence on the electric potential and field distributions. They used FDM as the numerical solver of their 1D and single-species model. The author of this thesis believes that they mistakenly reported the pulse-shaped output current as a Trichel pulse; it appears that this pulse was generated due to the pulsed-shape of the applied voltage.

Qin and Pedrow [76] applied a dynamic 2D simulation based on the particle-in-cell technique for modelling a cylindrical bipolar DC corona. FEM and CSM were used for the Poisson equation and FDM was used for the calculation of particle concentration.

Zhang and Adamiak [77] proposed a dynamic model for the negative corona discharge in the point-plane geometry. They used a hybrid BEM-FEM technique to calculate the electric-field parameters and they used MoC for the charge-transport

prediction. This model was valid for single-species discharge only but successfully simulated the full current waveform under different waveforms of the applied voltage: step, square and pulse.

3.4 Why FEM-FCT?

As mentioned earlier, for modelling gas discharge problems like streamers, Trichel pulses and coronas, the Poisson equation needs to be solved for calculating the electric field due to the space charge and charge continuity equations should be solved to model the transport and generation of ionic space charge density [30], [35]. The electric field has a very non-uniform distribution with the strongest values localized in the area close to the corona electrode but is affected by the net space charge which depends on the electron, negative and positive ion densities. Hence, to find its value accurately, charge densities must be determined with high accuracy with no ripples or artificial diffusion [78]. Therefore, a very accurate numerical technique is required for this purpose.

Linear schemes have a poor performance for transient problems with steep gradients, i.e. coronas, because the high-order solution would be oscillatory and noisy, and the low-order solution would be smooth but over-diffusive [79]. Godunov's theorem states this observation as follows:

No linear scheme of order greater than one will yield monotonic (wiggle-free and ripple-free) solutions [80].

To overcome this difficulty, nonlinear schemes should be developed. The easiest way for creating a nonlinear algorithm is by mixing a high-order one with a low-

order one. Combining these two schemes is called “limiting” and FCT is an algorithm developed based on this idea. Such an algorithm is used in many CFD problems which involve transport of scalar quantities that should remain positive for physical reasons [81]. Moreover, since the method should be able to describe the transport of low density values with the same accuracy as large ones, in solving charge continuity equations most of the existing methods for the solution of gas discharge problems are based on the FCT [78]. The combination of FCT with FDM was very common until recently, but since FDM needs a rectangular discretization of the domain and a structured mesh, the number of unknowns is very large; this leads to very long calculations and needs a large memory. In order to avoid this, the problem dimension is often reduced to one [82], [83], [84] and [85]. This approximation is not accurate enough and can only be used for very simple geometries. Some work has been done in using FDM-FCT in two dimensions but they were restricted to very simple geometries [86]-[87] or very short time intervals [88].

To overcome the restrictions mentioned above, in this thesis a FEM-FCT algorithm has been developed. This technique fulfills the following requirements [78]:

- it gives positive, accurate results, free from non-physical density fluctuation and numerical diffusion,
- it is computationally efficient,
- it can be easily adopted for any geometry.

The first requirement is satisfied by using a special method such as the FCT, which takes into account only the “real” diffusion in the system. The FCT method can capture the steep density gradients without introducing spurious oscillations or

artificial diffusion. In order to fulfill the last two requirements, FEM should be used because it offers computational efficiency through the use of unstructured grids. Therefore, the FEM version of FCT used in this thesis can fulfill all the requirements [81] and is an extension of the method proposed by Loehner et al. [79], which has been successfully used in fluid mechanics.

3.5 Finite Element Method

The FEM originated from the need for solving complex elasticity and structural analysis problems in civil and aeronautical engineering [89]. Its development can be traced back to the work by Alexander Hrennikoff (1941) and Richard Courant (1942). While the approaches used by these pioneers were dramatically different, they share one essential characteristic: mesh discretization of a continuous domain into a set of discrete sub-domains usually called elements [90].

At 1968, this method was first used in electromagnetic (EM) problems [91]. In comparison with FDM and Method of Moments (MoM), FEM is more complicated but it is more versatile and powerful for handling problems with complex geometries and in non-homogeneous media. Another advantage of this technique is in programming flexibility and elegance. Because of the systematic generality of this technique, a general purpose computer program can be developed and can be used for a wide range of problems.

Six basic steps are involved in this method [91]:

1. Discretization of the solution region into elements: these elements can be 1D, 2D or 3D depending on the configuration of the problem.

2. Interpolation of the solution: in this step, the unknown variable inside the element is interpolated based on the nodal values.
3. Deriving governing equations for each element: by converting the differential equations and the associated boundary conditions to an integro-differential formulation. This can be done either by minimising a functional or by using a weighted residual method such as the Galerkin one. After this step, a matrix equation for one element is generated.
4. Assembling matrix equations for all elements in the solution region to form a global set of equations.
5. Introducing the boundary conditions.
6. Solving the resulting system of equations using matrix inversion or iterative techniques.

Solving Poisson Equation Using FEM

In order to solve the Poisson equation: $\nabla^2 V = -\frac{\rho}{\epsilon_0}$ using FEM, the solution region should first be divided into elements. In this thesis, triangular elements are assumed for simplicity.

Secondly, the electric potential V and the charge density distribution (ρ) should be approximated over each element using a linear function:

$$V_e = \sum_{i=1}^3 V_{ei} \alpha_i(x, y) \quad (3.1)$$

$$\rho = \sum_{i=1}^3 \rho_{ei} \alpha_i(x, y) \quad (3.2)$$

As equations (3.1) and (3.2) show, potential and charge density at any point (x, y) within the element is known provided that nodal values of V and ρ are known. Therefore, another advantage of FEM over FDM is its ability to obtain the unknown values at any point within the region not just at the grid points.

α_i s are called shape functions and they have the following properties:

1. $\alpha_i(x_j, y_j) = \begin{cases} 1 & i = j \\ 0 & i \neq j \end{cases}$
2. $\sum_{i=1}^3 \alpha_i(x, y) = 1$

According to the variational principle, the problem of solving Poisson equation is equivalent to the problem of finding an extremum for the energy functional. For the Poisson equation, this functional is given by [91]:

$$F(V_e) = \frac{1}{2} \int_S [\epsilon |\nabla V_e|^2 - 2\rho_e V_e] \quad (3.3)$$

$F(V_e)$ represents the total potential energy per unit length accumulated in the element. The first term: $\frac{1}{2} \vec{D} \cdot \vec{E} = \frac{1}{2} \epsilon |\nabla V_e|^2$ is the energy density in the electrostatic system while the second term $\rho_e V_e dS$ is the work done in moving the charge $\rho_e dS$ to its location at potential V_e . Substituting equations (3.1) and (3.2) in equation (3.3) we have,

$$F(V_e) = \frac{1}{2} \sum_{i=1}^3 \sum_{j=1}^3 \epsilon V_{ei} \left[\int \nabla \alpha_i \cdot \nabla \alpha_j dS \right] V_{ej} - \sum_{i=1}^3 \sum_{j=1}^3 V_{ei} \left[\alpha_i \alpha_j dS \right] \rho_{ej}$$

This functional can be written in matrix form as:

$$F(V_e) = \frac{1}{2}\varepsilon [V_e]^t [C^{(e)}] [V_e] - [V_e]^t [T^{(e)}] [\rho_e] \quad (3.4)$$

$$C_{ij}^{(e)} = \int \nabla \alpha_i \nabla \alpha_j dS$$

$$[C^{(e)}] = \begin{bmatrix} C_{11}^{(e)} & C_{12}^{(e)} & C_{13}^{(e)} \\ C_{21}^{(e)} & C_{22}^{(e)} & C_{23}^{(e)} \\ C_{31}^{(e)} & C_{32}^{(e)} & C_{33}^{(e)} \end{bmatrix}$$

Matrix $[C^{(e)}]$ is the element coefficient matrix, or stiffness matrix. Each element of this matrix shows the coupling between node i and j .

Also,

$$T_{ij}^{(e)} = \int \alpha_i \alpha_j dS$$

Equation (3.4) which is the governing equation for one element can be applied to every element in the solution region. Sum of the functionals for each element yields the functional for the whole solution region.

$$F(V) = \sum_{e=1}^N F(V_e) = \frac{1}{2}\varepsilon [V]^t [C] [V] - [V]^t [T] [\rho] \quad (3.5)$$

Matrices $[V]$ and $[\rho]$ are composed of n values of potential and space charge densities at all the nodes.

The functional in equation (3.5) can be minimized by differentiating it with respect to V_{ei} and setting the result equal to zero.

The resulting equations can then be solved by either the iteration method or matrix inversion. In order to minimize the storage, many different schemes can be used; the simplest one is band matrix scheme [91]. These techniques are described below:

- Iteration method: By fixing the potential at the boundary nodes and setting the potential at other nodes to some initial value, equation (3.6) is applied to all nodes until convergence is reached.

$$V_k = -\frac{1}{C_{kk}} \sum_{i=1, i \neq k}^n V_i C_{ki} + \frac{1}{\varepsilon C_{kk}} \sum_{i=1}^n T_{ki} \rho_i \quad (3.6)$$

- Matrix inversion: the left hand side matrix is inverted and multiplied by both sides.
- Band Matrix Method: This important technique minimizes the size of the matrix storage for a time-efficient use of FEM. Since all the matrices involved in FEM are symmetric, sparse and banded, to reduce the memory usage and simulation time, only the matrix entries inside of a half-band-width not the whole matrix are stored [92].

In order to minimize the bandwidth, the nodes should be renumbered such that the difference between the lowest and the highest node numbers of any element of the mesh is minimized. The Cuthill-McKee algorithm was used by Xishen Deng, a senior student [92] for node renumbering. The generated subroutines are used in this thesis.

After finding potentials at all the nodes, the electric field can be calculated by differentiating V : $\vec{E} = -\nabla V$

3.6 Combined FEM-FCT

A typical format for charge continuity equation is: $\frac{\partial u}{\partial t} + \nabla \cdot (ku\vec{E}) = 0$

FEM-FCT algorithm for solving this equation consists of the following steps:

1. Compute the high order solution: Discretize the equation by a linear high order method (e.g., Galerkin FEM) and compute the high order solution (K) [93].

$$M_C \frac{du}{dt} = Ku, \text{ such that } \exists j \neq i : k_{ij} < 0$$

where M_C is the consistent mass matrix.

The discretization of a charge continuity equation using Galerkin FEM technique will be explained in the next Chapter.

2. Compute the low order solution (L): Compute solution from some low order scheme that guarantees monotonic and oscillation-free results. This technique is called upwinding.

$$L = K + D$$

$$M_C \frac{du}{dt} = Lu \text{ such that } l_{ij} \geq 0, \forall j \neq i$$

For the low order scheme to be non-oscillatory, all off-diagonal coefficients of the matrix L should be nonnegative. Hence the entries in matrix D are given by [93].

$$d_{ii} = -\sum_{j \neq i} d_{ij}, d_{ij} = \max(0, -k_{ij}, -k_{ji}) = d_{ji}$$

After initialization: $L = K$, each pair of nonzero off-diagonal elements l_{ij} and l_{ji} are examined. If the smaller one is negative, it is set equal to zero and three other entries are modified so as to restore row sums:

$$l_{ii} = l_{ii} - d_{ij};$$

$$l_{ij} = l_{ij} + d_{ij}$$

$$l_{ji} = l_{ji} + d_{ij};$$

$$l_{jj} = l_{jj} - d_{ij}$$

The low order solution can be represented as [79]:

$$u_i^l = u_i^h + \sum_{node} LEC_i, i = 1, 2, \dots, n$$

where u_i^h is the high order solution and LEC_i is the low-order contribution calculated for the i^{th} node. This scheme yields the least diffusive low order scheme obtainable from the original Galerkin discretization.

This technique is called discrete upwinding. The low order solution which is obtained in this step is over-diffusive. In order to improve the quality of the results and remove the excessive diffusion in smooth regions, a nonlinear antidiffusive correction is applied to the monotone operator L in the final step.

3. Limit the diffusion of the low order solution: In this step, all the unnecessary low-order contribution added in the second step is removed. This removal should be performed such that the solution remains oscillation free:

- Define the antidiffusive node contribution (A) [79] $A = K - L = -D$
Removal of excessive artificial diffusion is then accomplished by applying a limited amount of compensating anti-diffusion (F) which depends on the local solution behaviour and improves the accuracy in smooth regions. It is desirable to retain as much antidiffusion as possible without generating new extrema and amplifying already existing ones. To do this, the antidiffusive fluxes (A_{ij}) should be multiplied by an appropriate correction factor before they are added to the low order solution.
- Apply limiting to the antidiffusive node contribution and update the solution:

$$u_i = u_i^l + \sum_j A_{ij}^C$$

$$\text{where, } A_{ij}^C = \alpha_{ij} A_{ij}; 0 \leq \alpha_{ij} \leq 1$$

By varying the limiting factor α_{ij} between zero and unity, high-order method can be blended with the low-order method. In the vicinity of steep gradients (which is near the corona electrode in our geometry), where spurious oscillations are likely to arise, low order solution is used. The objective of this step is to control the antidiffusive fluxes so that they can not create or enhance a local extremum [94].

This step is very critical in the whole method. If we consider an isolated node surrounded by other nodes, the task of limiting is to ensure that the increase or decrease due to antidiffusive node contribution (A) does not exceed a prescribed tolerance. Limiting procedure will be discussed in the next section.

Applying FEM-FCT to a charge continuity equation

The charge continuity equation can be written in more detailed form as:

$$\frac{\partial \rho}{\partial t} + k \vec{E} \cdot \nabla \rho + \frac{k}{\varepsilon} \rho^2 - D \nabla^2 \rho = 0 \quad (3.7)$$

First, the above equation is discretized using Galerkin-FEM method and the high order solution is obtained:

$$\int_{\Delta} N_i \left(\frac{\partial \rho}{\partial t} + k \vec{E} \cdot \nabla \rho + \frac{k}{\varepsilon} \rho^2 - D \nabla^2 \rho \right) ds = 0$$

$$\rho = \sum_j \rho_j N_j$$

$$\rho^2 \simeq \sum_j \rho_j^2 N_j$$

The matrix form of this equation would be:

$$[T] \frac{\partial \rho}{\partial t} = [K] [\rho] + [Q] [\rho^2] \quad (3.8)$$

$$\text{in which, } t_{ij} = \int_{\Delta} N_i N_j dS = \frac{\Delta}{12} \begin{cases} 2 & i = j \\ 1 & i \neq j \end{cases}$$

$$\text{For simplicity of calculations, matrix } [T] = \frac{\Delta}{12} \begin{bmatrix} 2 & 1 & 1 \\ 1 & 2 & 1 \\ 1 & 1 & 2 \end{bmatrix} \text{ is approximated}$$

$$\text{by its lumped mass corresponding matrix: } [M] = \frac{\Delta}{3} \begin{bmatrix} 1 \\ 1 \\ 1 \end{bmatrix} \text{ in which } m_i = \sum_j t_{ij};$$

therefore, the simplified charge continuity equation is:

$$[M] \frac{\partial \rho}{\partial t} = [K] [\rho] + [Q] [\rho^2]$$

This equation can be solved by approximating the time derivative by finite differences:

$$\frac{\partial \rho}{\partial t} = \frac{\rho_i^{n+1} - \rho_i^n}{t}$$

This results in:

$$\rho_i^{n+1} = \rho_i^n + \frac{\Delta t}{m_i} \left([K] [\rho] + [Q] [\rho^2] \right) \quad (3.9)$$

where,

$k_{ij} = - \int_{\Delta} k \vec{E} \cdot N_i \left(\frac{b_j}{2\Delta} \hat{x} + \frac{c_j}{2\Delta} \hat{y} \right) ds = -\frac{k}{6} (E_x b_j + E_y c_j)$ and Q_{ij} can be calculated analytically.

To transform this oscillatory high-order solution into its nonoscillatory low-order counterpart, a discrete diffusion operator D as described in previous section is added to the high order solution [93].

$$[M] \left[\frac{\partial \rho}{\partial t} \right] = [K] [\rho] + [Q] [\rho^2] \rightarrow [M] \left[\frac{\partial \rho}{\partial t} \right] = [L] [\rho] + [Q] [\rho^2] \quad (3.10)$$

in which, $[L] = [K] + [D]$. The antidiffusive node contribution is:

$$AEC_i = HEC_i - LEC_i = \frac{\Delta t}{m_i} \sum_{j \neq i} d_{ij} (\rho_i^n - \rho_j^n) \quad (3.11)$$

The updated low order solution is:

$$\rho_i^l = \rho_i^n + \sum_j LEC_j \Rightarrow \rho_i^l = \rho_i^n + \frac{\Delta t}{m_i} \sum_j (k_{ij}\rho_j^n + q_{ij}\rho_j^{2n}) + \frac{\Delta t}{m_i} \sum_{j \neq i} d_{ij}(\rho_j^n - \rho_i^n) \quad (3.12)$$

In the next step, limiting is applied and the final solution is obtained as follows:

$$\rho_i^{n+1} = \rho_i^l + \sum_j AEC_{ij}^c =$$

$$\rho_i^n + \frac{\Delta t}{m_i} \sum_j (k_{ij}\rho_j^n + q_{ij}\rho_j^{2n}) + \frac{\Delta t}{m_i} \sum_j d_{ij}(\rho_j^n - \rho_i^n) + \frac{\Delta t}{m_i} \sum_{j \neq i} \alpha_{ij} d_{ij}(\rho_i^n - \rho_j^n) \quad (3.13)$$

where, α_{ij} is:

$$\alpha_{ij} = \begin{cases} R_i^+ & A_{ij} \geq 0 \\ R_i^- & A_{ij} < 0 \end{cases} \quad (3.14)$$

where, $A_{ij} = -d_{ij}(\rho_j^n - \rho_i^n)$

$$R_i^+ = \begin{cases} \min\left(1, \frac{Q_i^+}{P_i^+}\right) & P_i^+ \neq 0 \\ 0 & P_i^+ = 0 \end{cases} \quad R_i^- = \begin{cases} \min\left(1, \frac{Q_i^-}{P_i^-}\right) & P_i^- \neq 0 \\ 0 & P_i^- = 0 \end{cases} \quad (3.15)$$

$$P_i^+ = \frac{1}{m_i} \sum_{j \neq i} \max(0, A_{ij}) = \frac{1}{m_i} \sum_{j \neq i} \max(0, -d_{ij}(\rho_j - \rho_i)) \quad (3.16)$$

$$P_i^- = \frac{1}{m_i} \sum_{j \neq i} \min(0, A_{ij}) = \frac{1}{m_i} \sum_{j \neq i} \min(0, -d_{ij}(\rho_j - \rho_i)) \quad (3.17)$$

$$Q_i^+ = \rho_i^{max} - \rho_i^l$$

$$Q_i^- = \rho_i^{min} - \rho_i^l$$

$$\rho_i^{max} = \max[\rho_j^n, \rho_i^l], j \in S_i$$

$$\rho_i^{min} = \min[\rho_j^n, \rho_i^l], j \in S_i$$

S_i consists of node i and its nearest neighbors (all nodes which are connected to node i).

3.7 Conclusions

In this Chapter, a comprehensive review on different proposed techniques for solving the Poisson equation, charge continuity equation, and both equations simultaneously were explained. Among these techniques, the one which seems to be best suited for simulating corona discharge, the FEM-FCT, was explained in detail and is used in this thesis. The full mathematics of this technique were explained in detail.

Chapter 4

Implementation of FEM-FCT Algorithm for Trichel Pulse Simulation

4.1 Governing Equations

Figure 4.1 shows the configuration of corona discharge system used in this thesis. A hyperbolic needle is perpendicular to an infinitely large plate at a distance d with a tip radius curvature R and length L . Negative potential V_c is applied to the circuit. An external resistance R_{ext} is connected in series with the needle and the ground plate. The ambient gas is air at room temperature and atmospheric pressure.

As explained in the previous chapter, for three-species modelling of the Trichel pulse regime in negative corona discharge, three charge continuity equations and the corresponding Poisson equations should be simultaneously solved in order to model the variations of the space charge densities and the electric field with time. The details for solving all continuity equations are discussed below.

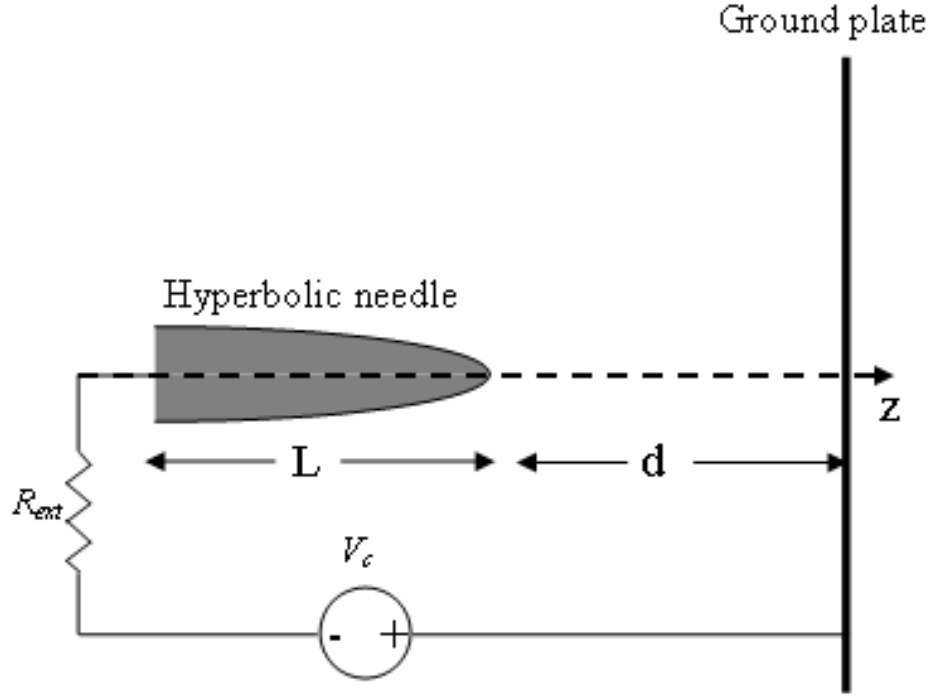


Figure 4.1: The configuration of corona discharge system.

1. Continuity equation for electrons:

$$\frac{\partial N_e}{\partial t} + \nabla \cdot \vec{J}_e = N_e \alpha |\vec{W}_e| - N_e \eta |\vec{W}_e| - \frac{N_e N_p \beta_{ep}}{e_0} \quad (4.1)$$

$$\vec{J}_e = -k_e N_e \vec{E} - D_e \nabla N_e \quad (4.2)$$

(4.1), (4.2) \Rightarrow

$$\frac{\partial N_e}{\partial t} + \nabla \cdot \left(-k_e N_e \vec{E} - D_e \nabla N_e \right) = N_e \alpha |\vec{W}_e| - N_e \eta |\vec{W}_e| - \frac{N_e N_p \beta_{ep}}{e_0} \quad (4.3)$$

In these equations, N_e is the electron density, \vec{J}_e is the current density due to the motion of electrons, α is the ionization coefficient, \vec{W}_e is the drift velocity

of electrons, η is the attachment coefficient, N_p is the positive ion density, β_{ep} is the recombination coefficient between electrons and positive ions, e_0 is the electron charge and is equal to 1.602×10^{-19} , k_e is the mobility of electrons, \vec{E} is the electric field, and D_e is the diffusion coefficient. N_e , N_p and \vec{E} are unknown distributions, $\vec{W}_e = -k_e \vec{E}$ and the value of other coefficients will be presented in Chapter 6.

Applying Galerkin FEM (weak formulation) to this equation results in:

$$\begin{aligned} & \sum_j \left(\int_{\Delta} N_i N_j ds \right) \frac{\partial N_{ej}}{\partial t} - k_e \vec{E} \cdot \sum_j \left(\int_{\Delta} N_i \nabla N_j ds \right) N_{ej} - \frac{k_e N_p}{\varepsilon_0} \sum_j \left(\int_{\Delta} N_i N_j ds \right) N_{ej} \\ & + \frac{k_e N_n}{\varepsilon_0} \sum_j \left(\int_{\Delta} N_i N_j ds \right) N_{ej} + \frac{k_e}{\varepsilon_0} \sum_j \left(\int_{\Delta} N_i N_j ds \right) N_{ej}^2 + \\ & D_e \sum_j \left(\int_{\Delta} \nabla N_i \cdot \nabla N_j ds \right) N_{ej} = \alpha_i |W_{ei}| \sum_j \left(\int_{\Delta} N_i N_j ds \right) N_{ej} - \\ & \eta_i |W_{ei}| \sum_j \left(\int_{\Delta} N_i N_j ds \right) N_{ej} - \frac{N_p \beta_{ep}}{e_0} \sum_j \left(\int_{\Delta} N_i N_j ds \right) N_{ej} \end{aligned}$$

This integro-differential equation can be simplified to an algebraic form as follows:

$$\begin{aligned} & \sum_j t_{ij} \frac{N_{ej}^{n+1} - N_{ej}^n}{\Delta t} = \sum_j k_{eij} N_{ej} + \frac{k_e N_p}{\varepsilon_0} \sum_j t_{ij} N_{ej} - \frac{k_e N_n}{\varepsilon_0} \sum_j t_{ij} N_{ej} - \\ & \frac{k_e}{\varepsilon_0} \sum_j t_{ij} N_{ej}^2 - D_e \sum_j s_{ij} N_{ej} + \alpha_i |W_{ei}| \sum_j t_{ij} N_{ej} - \eta_i |W_{ei}| \sum_j t_{ij} N_{ej} - \\ & \frac{N_p \beta_{ep}}{e_0} \sum_j t_{ij} N_{ej} \end{aligned}$$

In this equation, the first five terms of the right hand side of the equation form the transport component and the remaining terms form the reaction component and,

$$s_{ij} = \int_{\Delta} \nabla N_i \cdot \nabla N_j ds$$

$$t_{ij} = \int_{\Delta} N_i N_j dS = \frac{\Delta}{12} \begin{cases} 2 & i = j \\ 1 & i \neq j \end{cases}$$

$$k_{eij} = \int_{\Delta} k_e \vec{E} \cdot N_i \left(\frac{b_j}{2\Delta} \hat{x} + \frac{c_j}{2\Delta} \hat{y} \right) ds = \frac{k_e}{6} (E_x b_j + E_y c_j)$$

where, N_i and N_j are the shape functions: $N_j = \frac{a_j + b_j x + c_j y}{2\Delta}$, $N_i = \frac{a_i + b_i x + c_i y}{2\Delta}$

Δ is the area of the element and is equal to:

$$\Delta = \frac{1}{2} ((y_j - y_k)(x_i - x_k) - (y_k - y_i)(x_k - x_j))$$

$$\text{and } \begin{bmatrix} b_i \\ b_j \\ b_k \end{bmatrix} = \begin{bmatrix} y_j - y_k \\ y_k - y_i \\ y_i - y_j \end{bmatrix}$$

$$\begin{bmatrix} c_i \\ c_j \\ c_k \end{bmatrix} = - \begin{bmatrix} x_j - x_k \\ x_k - x_i \\ x_i - x_j \end{bmatrix}$$

The time derivative term, $\frac{\partial N_{ej}}{\partial t}$, has been substituted with its finite difference representation form: $\frac{N_{ej}^{n+1} - N_{ej}^n}{\Delta t}$ in which $n+1$ and n are two successive time instants and Δt is the time step.

This discretized equation shows that there are two terms involved with the electron density calculations: the transport term, which is related to the advection and diffusion of charge and the reaction term, which is related to the charge creation or disappearance due to the ionic reactions such as ionization, attachment and recombination.

The matrix form for this equation can be written as

$$[T] \left(\frac{\partial N_e}{\partial t} \right) = [K] (N_e) + [S] (N_e),$$

in which matrix $[K]$ is related to the transport term and matrix $[S]$ is related to the reaction term. The superposition principle is used for solving this equation as follows:

First, $[T] \left(\frac{\partial N_e}{\partial t} \right) = [K] (N_e)$ is solved by using FEM-FCT as explained in the previous Chapter. Secondly, the electron density related to the reaction term is calculated at each node and is directly added to the results obtained from the first step.

2. Continuity equation for negative ions:

$$\frac{\partial N_n}{\partial t} + \nabla \cdot \vec{J}_n = N_e \eta |W_e| \quad (4.4)$$

$$\vec{J}_n = -k_n N_n \vec{E} \quad (4.5)$$

where k_n is the mobility of negative ions, N_n is the negative ion density and \vec{J}_n is the current density due to the motion of negative ions.

Discretization of this equation leads to:

$$\sum_j t_{ij} \frac{N_{nj}^{n+1} - N_{nj}^n}{\Delta t} = \sum_j k_{nij} N_{nj} + \frac{k_n N_p}{\varepsilon_0} \sum_j t_{ij} N_{nj} - \frac{k_n N_e}{\varepsilon_0} \sum_j t_{ij} N_{nj} - \frac{k_n}{\varepsilon_0} \sum_j t_{ij} N_{nj}^2 + \eta_i |W_{ei}| \sum_j t_{ij} N_{ej}$$

in which,

$$k_{nij} = \int_{\Delta} k_n \vec{E} \cdot N_i \left(\frac{b_j}{2\Delta} \hat{x} + \frac{c_j}{2\Delta} \hat{y} \right) ds = \frac{k_n}{6} (E_x b_j + E_y c_j)$$

3. Continuity equation for positive ions:

$$\frac{\partial N_p}{\partial t} + \nabla \cdot \vec{J}_p = N_e \alpha \left| \vec{W}_e \right| - \frac{N_e N_p \beta_{ep}}{e_0} \quad (4.6)$$

$$\vec{J}_p = k_p N_p \vec{E} \quad (4.7)$$

where k_p is the mobility of positive ions, N_p is the positive ion density and \vec{J}_p is the current density due to the motion of positive ions.

After discretization we have,

$$\begin{aligned} \sum_j t_{ij} \frac{N_{pj}^{n+1} - N_{pj}^n}{\Delta t} = & - \sum_j k_{pij} N_{pj} + \frac{k_p N_n}{\varepsilon_0} \sum_j t_{ij} N_{pj} + \frac{k_p N_e}{\varepsilon_0} \sum_j t_{ij} N_{pj} - \frac{k_p}{\varepsilon_0} \\ & \sum_j t_{ij} N_{pj}^2 + \alpha_i |W_{ei}| \sum_j t_{ij} N_{ej} - \frac{N_e \beta_{ep}}{e_0} \sum_j t_{ij} N_{pj} \end{aligned}$$

in which,

$$k_{pij} = \int_{\Delta} k_p \vec{E} \cdot N_i \left(\frac{b_j}{2\Delta} \hat{x} + \frac{c_j}{2\Delta} \hat{y} \right) ds = \frac{k_p}{6} (E_x b_j + E_y c_j)$$

4. Poisson equation:

For calculating the electric field distribution, Poisson equation needs to be solved. For solving this equation, FEM method is used as described in the previous chapter.

$$\nabla^2 V = - \frac{N_p - N_n - N_e}{\varepsilon_0} \quad (4.8)$$

$$\vec{E} = -\nabla V$$

in which V is the electric potential and ϵ_0 is the permittivity of the gas.

4.2 Implementation of the Numerical Algorithm

At the initial stage of the project, there was a number of problems in the numerical technique which caused divergence in the calculation process. All attempts to solve the equation set resulted in an uncontrollable increase in time of the charge density amplitudes. Although the algorithm was tested for single-species modelling (Chapter 5) with the results being reasonable and consistent with the physical expectations, the three-species simulation was not convergent. A thorough search for finding the cause of the problem was conducted.

After doing a detailed investigation of different routines of the code and confirming the solution of the Poisson equation by comparing the code results with a commercial FEM solver (COMSOL Multiphysics), it was found that FEM-FCT algorithm used for solving the charge continuity equations was the cause. Two steps of this algorithm were the most critical: the high order and low order solutions. The process of finding the reasons for the lack of convergence and modifying the technique is described below:

1. The high-order solution:

The charge continuity equation for electrons (4.3) can be written in a simpler form as:

$$\frac{\partial N_e}{\partial t} + \nabla \cdot \vec{J}_e = (v_i - v_a) N_e - \frac{N_e N_p \beta}{e_0} \quad (4.9)$$

in which, $v_i = \alpha \left| \vec{W}_e \right|$ and $v_a = \eta \left| \vec{W}_e \right|$

After discretizing (4.9) the following equation is obtained:

$$\sum_j t_{ij} \frac{\partial N_{ej}}{\partial t} = \sum_j (c_{ij} N_{ej}) + \sum_j \left(\left(v_{iav} - v_{aav} - \beta \frac{N_{pav}}{e_0} \right) t_{ij} N_{ej} \right) \quad (4.10)$$

in which $c_{ij} = k_{ij} + \left(\frac{k_e}{\varepsilon_0} (N_{pav} - N_{eav} - N_{nav}) \right) t_{ij} - D_e s_{ij}$, and N_{pav} , N_{eav} , N_{nav} , v_{iav} and v_{aav} refer to the average values of N_p , N_e , N_n , v_i and v_a over an element.

To solve this equation, the first step is to find the high-order solution related to the transport term by solving:

$$[T] \left(\frac{\partial N_{ei}}{\partial t} \right) = [K] (N_{ei}) \quad (4.11)$$

In the previous Chapter, it was explained that in order to avoid using the Gaussian elimination technique, the distributed mass matrix $[T]$ can be approximated by a simpler lumped mass matrix $[M]$ in which $m_i = \sum_j t_{ij}$.

If the same approximation is used for the three species modelling, the numerical technique would diverge. The space charge densities will have oscillatory behaviour and will increase uncontrollably up to very large values. The large densities of space charge increase the amplitude of the corona current to very large values as well and the program eventually diverges. The origin of this

problem is that this approach to the high order solution is not accurate enough.

To fix this, two solutions were proposed:

- Solve the equation: $[M] \left(\frac{\partial N_{ei}}{\partial t} \right) = [K] (N_{ei}) + ([M] - [T]) \left(\frac{\partial N_{ei}}{\partial t} \right)$ which can be represented as:

$$N_{ei}^{n+1} - N_{ei}^n = \frac{1}{m_i} (\Delta t [[K] (N_{ei}) + ([M] - [T]) (N_{ei}^{n+1} - N_{ei}^n)])$$

In the literature, it is mentioned that the above equation usually leads to a convergent result after three iterations. However, this was not confirmed in the discussed case and a larger number of iterations was required for this purpose.

- Use matrix $[T]$ (instead of $[M]$) and the Gaussian elimination inversion technique to directly solve (4.11).

These two approaches were tested and both of them were able to fix the convergence problems although the second approach was less time-consuming, as the number of iterations needed for the first approach to converge was rather large (10-12 iterations) and it was much more time-consuming in comparison with the exact solving of the equation set.

2. The low-order solution: Since the high-order solution is oscillatory, this step adds some artificial diffusion which is needed to remove these oscillations from the charge distributions.

$$los_i = hos_i + \frac{\Delta t}{m_i} \sum_j d_{ij} (N_{ej}^n - N_{ei}^n) \quad (4.12)$$

In the literature, this procedure is not sufficiently clear. It is mentioned that eliminating all negative off-diagonal elements from the coefficient matrix removes the oscillations and smoothes the charge distributions. The necessary approach in a case when the coefficient matrix ($[C]$) is negative dominant has never been discussed in detail.

For negative ions and electrons, the coefficient matrix is mostly negative and removing all negative off-diagonal elements will cause convergence problems in these cases. The low-order solution is not supposed to create negative values for charge density distributions; however, during the simulation this step was generating such values. It was suspected that removing the positive off-diagonal elements from the coefficient matrix of electrons and negative ions equations would alleviate the problem.

Therefore, the next important step was to verify if changing the coefficient matrix ($[C]$), so that all off-diagonal entries are negative for electron and negative ions would improve the results. This hypothesis has been confirmed and the results were convergent and consistent with the expectations.

3. Limiting procedure: Since in the second step the added diffusion is not fully needed, in the flat (nonoscillatory) parts of the distributions the extra diffusion should be removed. Diffusion is only needed in the oscillatory parts and an exact amount of diffusion should be left just to remove the oscillations.

$$m_{ei} = los_i + \frac{\Delta t}{m_i} \sum_j (-\alpha d_{ij} (N_{ej} - N_{ei})) \quad (4.13)$$

After performing the third step, the electron distributions due to the transport term are calculated, m_{ei} . However, to find the final distributions, there is still a term related to reactions, ionization, attachment and recombination which needs to be added to the charge densities. Therefore, the final result for the density of electron at node i would be:

$$N_{ei} = m_{ei} + \frac{\Delta t}{m_i} \sum_j t_{eij} m_{ej} \quad (4.14)$$

in which m_{ei} is the calculated electron density resulting from the transport term. N_{ei} is the total electron density obtained from the superposition of the transport term and the reaction terms.

4.3 Optimization Techniques

Since the time step which needs to be used in the two-dimensional Trichel pulse simulation is usually very small; this process is very time-consuming. It has been checked that during the pulse, the time step cannot be larger than 0.2ps while between the pulses the time step can be increased up to 3ps. If the time step is too large the program diverges because it cannot capture the very steep changes of the space charge density of all ionic species.

Since the period of Trichel pulses is in the range of several micro-seconds, the ratio between the time of a full pulse and the time step would be in the order of 10^7 . Since the numerical calculations for each iteration are very complicated and time-consuming, the time needed for the simulation of several Trichel pulses would

be extremely long. Therefore, presenting a technique that can reduce the simulation time is essential. The following techniques were used in this thesis for this purpose.

Since maintaining short time steps during the whole simulation would lead to prohibitively long calculations, an algorithm for an adaptive time step selection has been adopted; the time step was adjusted depending on the value of the total corona current. The larger the current, the smaller time step should be used since at larger currents the electric field is larger and a smaller time step is required in order to capture the generation of electrons.

There are two conditions for time step that should be satisfied [30]:

1. Courant-Friedricks-Lewy condition $\Delta t \leq \frac{\Delta x}{|\vec{W}_e|}$
2. Von Neumann condition $\Delta t \leq \frac{\Delta x^2}{2D}$

in which Δx is the smallest mesh size along the axis.

According to the equation, $\Delta t = \frac{\Delta x}{|\vec{W}_e|}$, the time step depends on the charge velocity $|\vec{W}_e|$. Therefore, it indirectly depends on the magnitude of electric field and mobility of charges, as $|\vec{W}_e| = \mu \vec{E}$.

As this formula shows, it is clear that with the same Δx , a larger mobility μ results in shorter tolerable time step Δt . Since the mobility of electrons is at least 100 times larger than the mobilities of the positive and negative ions, the time step limitations resulting from presence of electrons are at least 100 times smaller than the limitations resulting from the presence of ions. Therefore, if electrons can be

neglected, the time step can be increased at least 100 times and this would greatly accelerate the simulation process.

This was the idea behind the optimization technique used in this thesis for reducing the simulation time. Accordingly, two models are used in the simulation process:

1. three-species model with a short time step used during the Trichel pulse or for the time periods in which the total charge of electrons in the air gap is significant,
2. two-species model with a larger time step used for the time periods in which the total charge of electrons in the air gap has been reduced and was sufficiently small to be neglected. In these periods the density of electrons at every node is practically zero and the charge calculations are limited to positive and negative ions.

To test this technique, the double time step algorithm is compared with the three-species model assuming a specific applied voltage. The characteristics of the Trichel pulses (period and amplitude) have been obtained using both techniques. The optimized technique has proved to be very close with the exact technique.

4.4 Conclusions

In this chapter, the charge continuity equations governing a three species model of the Trichel pulse regime of corona discharge were discussed and the FEM-FCT technique was applied to these equations. Practical problems associated with the numerical

implementation of the proposed technique were discussed. The effective solutions for dealing with these problems were presented and explained in detail. Moreover, two techniques for accelerating the simulation process were proposed and explained.

Chapter 5

Dynamic Simulation of Single Species

Corona Discharge

5.1 Introduction

In Chapters 3 and 4, the numerical algorithm and the mathematical model for simulating the Trichel pulse regime of a corona discharge were presented. To test this algorithm before using it in three-species modelling, it was necessary to apply it to a simpler problem (single-species modelling) first.

Moreover, the majority of published studies have dealt with the point-plane electrode systems and DC voltages rather than pulsed ones. This is due to the simpler nature of DC systems for understanding and analysis. However, corona systems with pulse energization are preferred in many applications because of lower power consumption and reduction of some parasitic effects such as the back corona discharge. The numerical simulation of the full dynamics of transient corona discharge is important for the optimization of these devices [95]. While some authors attempted the simulation of the transient behaviour of corona discharge, no simple model of the

electric corona discharge valid for an arbitrary waveform of the applied voltage has been presented to date.

The Trichel pulse regime is only present in DC negative corona. To investigate the behaviour of pulsed corona without interference from Trichel pulse, it is necessary to test the algorithm with positive polarity where no Trichel regime is present.

In this chapter, a numerical model for the simulation of corona discharge in air is proposed. The model is dynamic and single-species, i.e. the ionization layer is completely neglected and it is assumed that only positive ions are present. The simulation results show the behaviour of conduction current and space charge density under two waveforms of the applied voltage: step and pulse. The electric field is calculated by means of FEM and the hybrid FEM-FCT technique is utilized for the space charge density calculations. The details of these techniques were explained in Chapter 3.

5.2 Mathematical Model

5.2.1 Governing Equations

Two different waveforms of the voltage, step and pulse-shaped were applied to the corona electrode. As this is a single species model, it is assumed that the ionization layer can be neglected and positive ions with average mobilities are assumed to be injected from the corona electrode.

The magnetic effects in the considered problem are negligible because of very low currents densities. As a result, the generated magnetic field is very weak and doesn't affect the ionization process. The equations modelling this problem are explained in

Chapter 3 but are repeated here for clarification. The equations defining the electric field and charge are:

$$\nabla^2 V = -\frac{\rho}{\varepsilon_0} \quad (5.1)$$

$$\frac{\partial \rho}{\partial t} + k\vec{E} \cdot \nabla \rho + \frac{k}{\varepsilon} \rho^2 - D\nabla^2 \rho = 0 \quad (5.2)$$

where \vec{D} is the electrostatic displacement, ρ is the space charge density, \vec{j} is the electric current density, ε_0 is the gas permittivity, \vec{E} is the electric field, V is the electric potential and k is the mobility of charge carriers. At atmospheric pressure and room temperature, k is equal to $2 \times 10^{-4} m^2/V \cdot s$ [23].

D is the diffusion coefficient and is calculated using the Nerst-Einstein relation [37]:

$$D = \frac{k_B T \cdot k}{e_0} \quad (5.3)$$

where k_B is the Boltzmann constant which is equal to $1.38065 \times 10^{-23} m^2 kg s^{-2} K^{-1}$, T is the absolute temperature, e_0 is the electron charge, equal to $1.602 \times 10^{-19} C$.

To model the corona discharge, equations (5.1) and (5.2) should be solved simultaneously assuming the boundary conditions introduced in the following section.

5.2.2 Boundary Conditions

The corona electrode and ground are equipotential. Therefore, the boundary conditions for voltage are the Dirichlet boundary conditions:

- $V = V_c$ on the corona electrode.
- $V = 0$ on the ground plate.

Since the charge continuity equation is a second order differential equation, it needs two boundary conditions. The first condition is that the normal derivative of space charge is zero on the ground electrode which is a Neumann boundary condition.

The value of space charge density at different points of the corona electrode is the second required boundary condition for space charge density. Since the assumed model of the problem ignores the ionization process, it is impossible to derive the exact value of space charge density at different points of the corona electrode. The corona discharge starts as the field strength exceeds some threshold value E_o . Therefore, the boundary condition for the charge density is usually replaced by the additional condition for the field strength on the corona electrode surface, $E(P) = E_o$, which can be related to the corona onset voltage V_o [96].

In this case, it is assumed that the onset value of the electric field on the corona electrode surface is obtained using Peek's formula which in air has the following form [53]:

$$E_o = 3.1 \times 10^4 \delta \left(1 + \frac{0.308}{\sqrt{r_{eq} \delta}} \right) (kv/cm)$$

where $\delta = \frac{T_0 P}{T P_0}$, T_0 is the standard temperature, T is the actual temperature, r_{eq} is the equivalent radius, P_0 is the standard pressure and P is the actual pressure of gas.

This formula is theoretically valid only for 1D cases: point-sphere or wire-cylinder. However, the same formula is used for the needle-plane geometry by assuming that the equivalent radius $r_{eq}(cm)$ is equal to the mean of the principal radii of curvature of the corona wire surface [97]. When the electric field magnitude is smaller than the Peek's value, the space charge density on the corona electrode surface is assumed to be zero. When the electric field is larger than the Peek's value, the space charge density is iterated until the electric field is sufficiently close to this value.

In this Chapter, an iterative algorithm has been developed in C programming language. It was then compiled and run in Linux environment. For a given space charge density, the electric field is calculated by solving (5.1). The electric field varies strongly in both space and time. Near the discharge electrode the electric field variation is particularly steep which demands a very fine spatial mesh while in the remaining region the electric field variation is more uniform. A non-uniform spatial mesh is therefore essential for an accurate numerical treatment near the electrodes and the air gap. As discussed in Chapter 3, FEM is used for electric field simulation and a Finite Element version of FCT is used for space charge density calculations.

At first, some arbitrary initial space charge density on the corona electrode surface is assumed. When the applied voltage is larger than the corona onset value, (5.1) and (5.2) are solved iteratively for one time step and the charge density on the surface of the corona electrode is updated until the electric field on the electrode surface is equal to the Peek's experimental value. If the applied voltage decreases below the corona onset level, the surface charge density on the corona electrode is zero and the existing space charge moves towards the ground plate under the effect of the applied voltage which creates an electric field and pushes the space charge

towards the ground.

The termination criteria of the iterative loops are the satisfaction of the following conditions:

1. The change of conduction current in two successive iterations should be less than δ_1 . This condition is used to check the convergence of the corona electrode voltage which changes due to voltage drop on the external resistor. Also, it is affected by the space charge convergence since if the space charge is convergent, the electric current which is related to space charge will also be convergent.

$$\left| \frac{I_{k+1} - I_k}{I_{k+1}} \right| < \delta_1 \quad (5.4)$$

2. Summation of deviations of electric field on the corona tip nodes from Peek's value should be less than δ_2 :

$$\sum_{i=\text{tip nodes}} \frac{(E_i - E_{peek,i})^2}{E_{peek,i}^2} \leq \delta_2 \quad (5.5)$$

Figure 2.1 shows the flowchart of the simulation process. Figure 5.2 shows the mesh generated for the air gap required for numerical calculations. As this Figure shows, triangular elements are used. To generate these elements, the equipotential lines and the electric field lines are traced and nodes are placed at the points of intersection of both lines. Quadrilaterals are formed and each of them is divided into two adjacent triangles.

5.3 Results

As shown in Figure 4.1, the hyperbolic needle is 1cm long ($L=1\text{cm}$) and is placed at 1cm above the ground plate ($d = 1\text{cm}$). The equivalent radius curvature R of the tip of the needle is $100 \mu\text{m}$. At room temperature and atmospheric pressure, the corona onset voltage for this configuration is calculated using the Peek's formula and is evaluated to be 4.7 kV.

5.3.1 Step Voltage

A step voltage with the value of 10.0 kV is applied at $t=0$. The total corona current in the circuit with the external resistance of $50 \text{ M}\Omega$ is shown in Figure 5.3. This graph has been obtained assuming that δ_1 and δ_2 in (5.4) and (5.5) are 0.05 and 0.1, respectively. The upper electrode and the ground plate form a capacitor and as a result, the system acts like an RC circuit.

The corona current can be calculated from [98]:

$$I = \frac{1}{V_0} \int \int \int \rho \vec{u} \cdot \vec{E}_L dv \quad (5.6)$$

where \vec{u} is the velocity of the ions, $\vec{u} = k\vec{E}$ and V_0 is the voltage applied to the corona electrode. E_L is the electric field calculated from the solution of Laplace's equation. This formula only includes conduction current as displacement current is neglected.

At $t=0$, there is no space charge in the air gap. Therefore, a very large space charge should be injected from the corona tip in order to satisfy Kaptzov's hypothesis

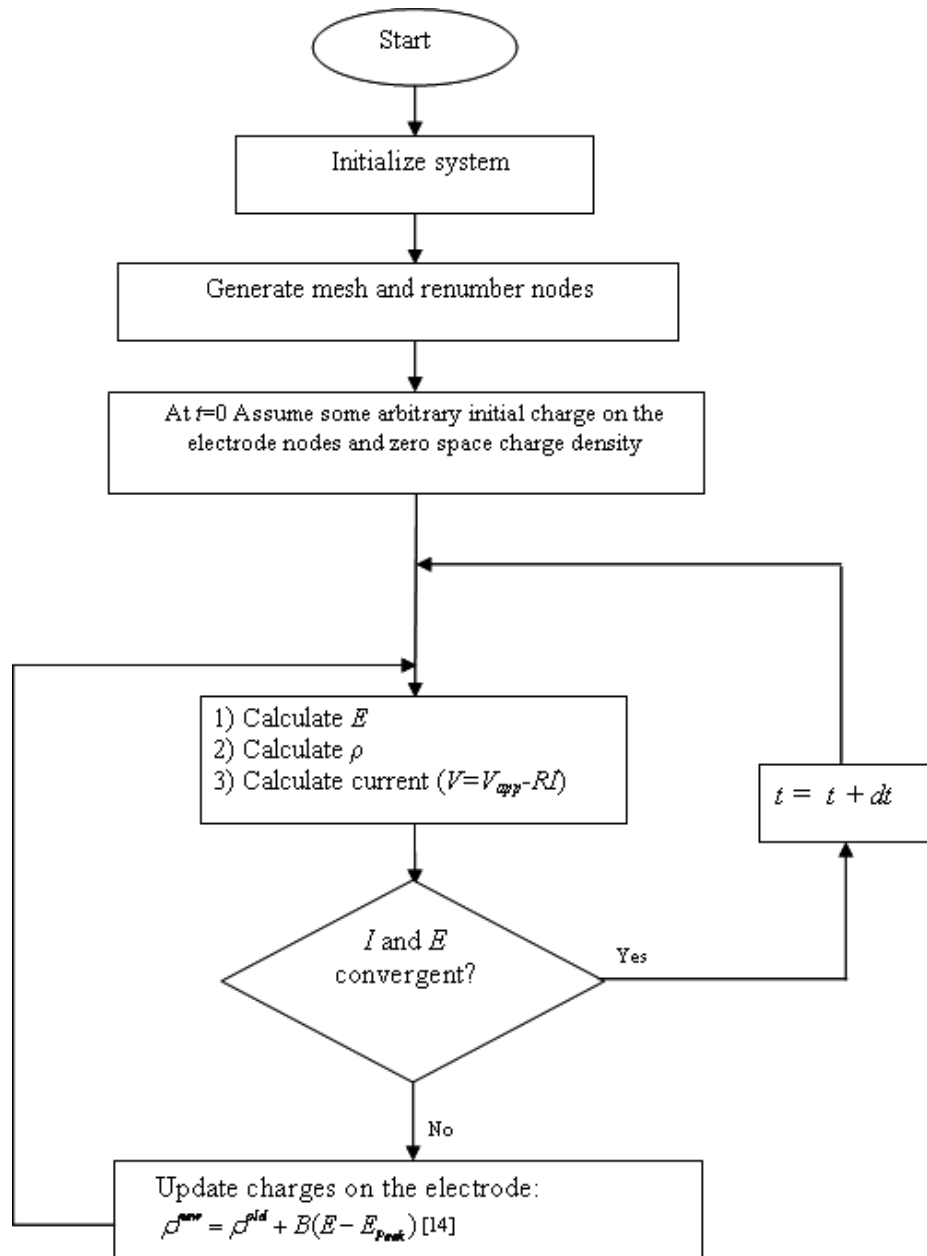


Figure 5.1: Flowchart of the simulation process.

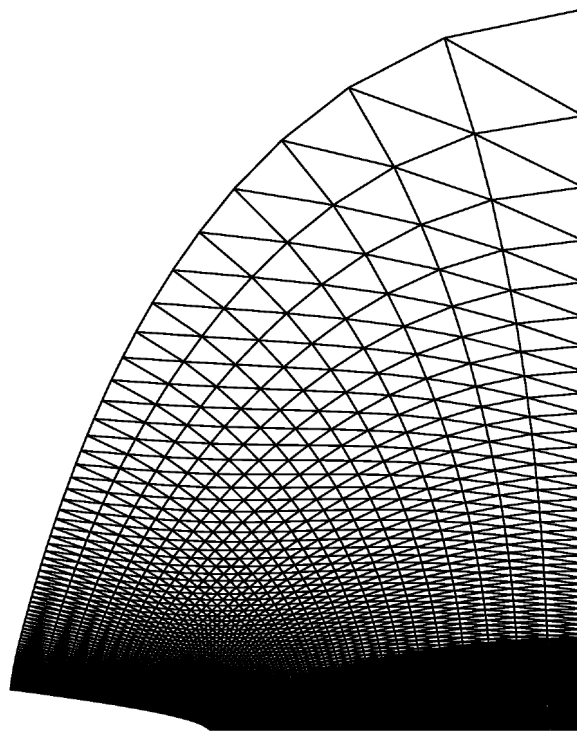


Figure 5.2: FE grid used in the simulation process.

for the electric field and this results in a large current at $t=0$. As time increases, since space charge is accumulated in the air gap, smaller injected charge is required to keep the electric field equal to Peek's value and this results in electric current decreasing with time.

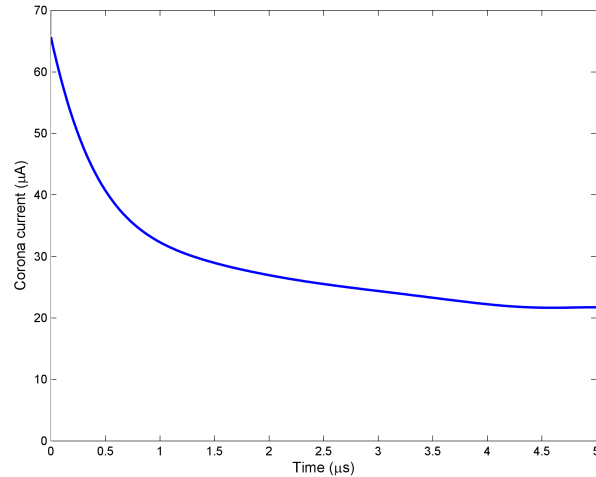


Figure 5.3: Corona current versus time ($R_{ext} = 50M\Omega, V = 10kV$)

Figure 5.4 shows this corona current versus time along with that for an external resistance equal to $5 M\Omega$. As expected, the value of current is larger for smaller external resistance. In Figure 5.5, the corona current versus time for two different input voltages is shown. This Figure shows that, as expected, a larger input voltage results in a larger current in the circuit.

Figure 5.6 shows the space charge density along the axis at six different instants of time. At $t = 160$ ns, the charge density is large and concentrated near the corona tip. Therefore, its value drops quickly along the axis. As time goes on, charge travels towards the ground plate and, as the Figure shows, it reaches the ground plate at about $t=50 \mu s$.

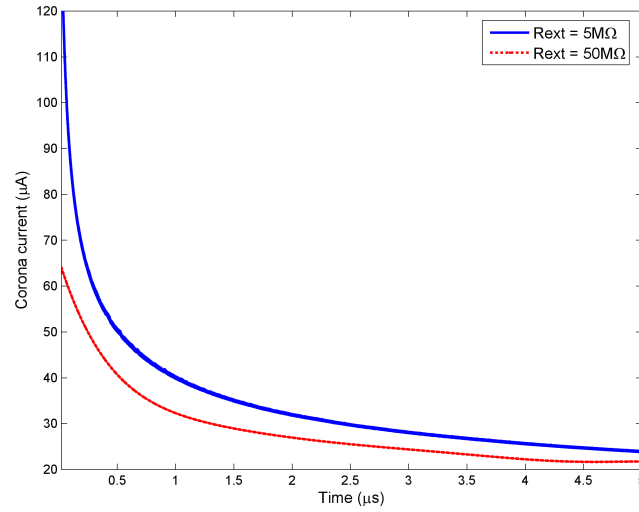


Figure 5.4: Corona current versus time for two different external resistances ($V=10\text{kV}$).

5.3.2 Pulse Voltage

In this section, a pulse voltage with the waveform shown in Figure 5.7 is applied to the corona electrode. The pulse voltage waveform is generated using a double exponential function having pulse parameters: the width of 300 ns, height of 6 kV ($V_m=6\text{ kV}$) and the rise time of $t_m = 60\text{ ns}$. These values are suitable for ESP applications [75].

The frequency of the pulses is chosen to be 5 kHz. This pulse voltage is superimposed on a DC voltage which is set at a value below the corona onset voltage (4kV).

Figures 5.8 and 5.9 show the corona current and space charge density on the corona tip versus time. Total corona current is zero at $t = 0$ and increases with applied voltage to a peak. Then, it starts decreasing and after some time only a

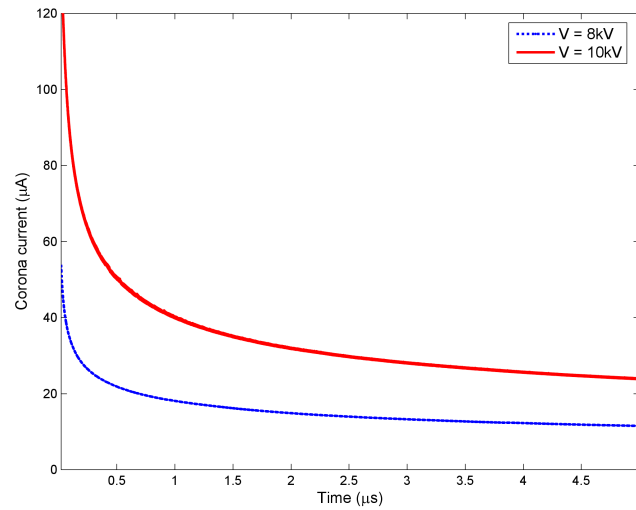


Figure 5.5: Current versus time for two different input voltages ($R_{ext} = 5M\Omega$).

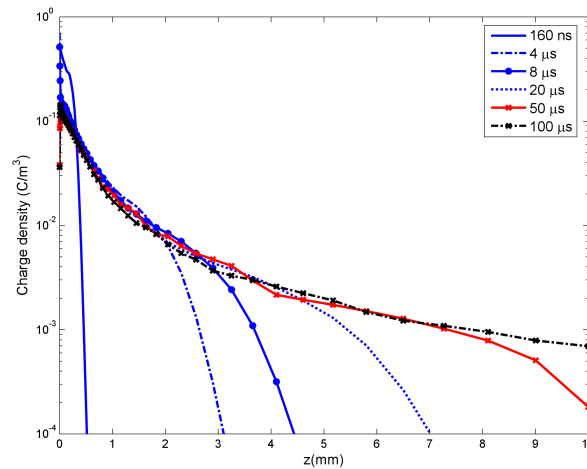


Figure 5.6: Space charge density along the axis of symmetry at six different instants of time ($R_{ext} = 50M\Omega$).

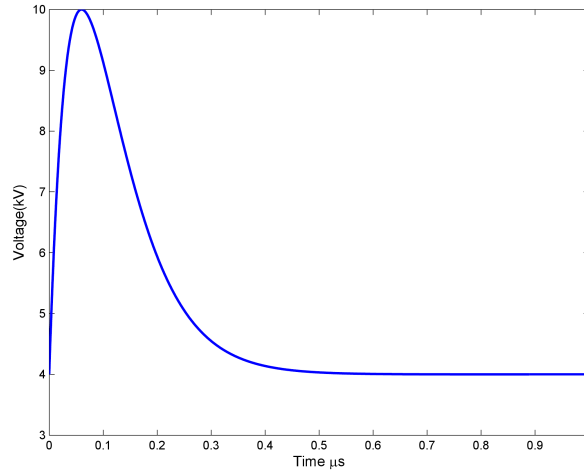


Figure 5.7: Applied pulse voltage described by $V_s(t) = \frac{V_m t}{t_m} e^{(1-\frac{t}{t_m})} + V_{DC}$.

small DC current ($I=1.24 \mu\text{A}$ at $t=1 \mu\text{s}$) will remain in the circuit. The local peak in Figure 5.9 at around $t=0.08 \mu\text{s}$ is a numerical artifact.

Figure 5.10 shows charge density along the axis of symmetry for five different time instants during and after the first voltage pulse. The ion cloud moves along the axis with time. At $t=40 \text{ ns}$, the ion cloud is near the tip and the value of space charge is large in this area. As time goes on, this cloud travels along the axis; at some instant of time the ionization stops and charge becomes negligible near the electrode tip. At $t=100 \mu\text{s}$ and $t=200 \mu\text{s}$, the charge cloud gets further from the tip and its peak decreases.

Figures 5.11 and 5.12 show the distribution of the space charge density in the entire air gap at two instants of time. At $t=10 \mu\text{s}$ (Figure 5.11), which is shortly after the first voltage pulse, the charge concentrates near the corona tip only.

At $t = 210 \mu\text{s}$ (Figure 5.12) there are two charge clouds. The smaller one is related to the first voltage pulse which has traveled along the axis, hence its value is

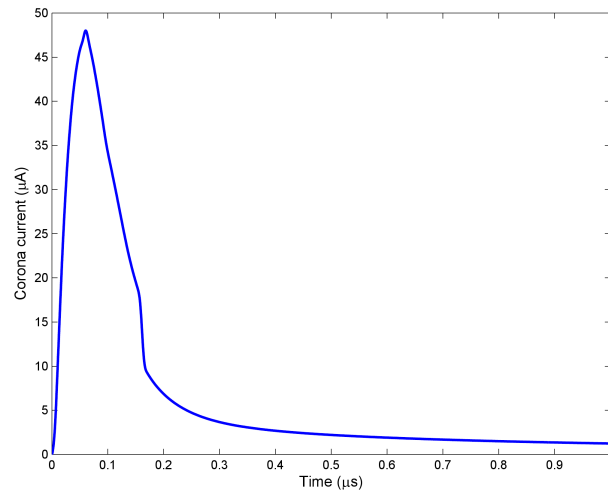


Figure 5.8: Corona current versus time for the pulse voltage shown in Figure 5.7 ($R_{ext} = 50M\Omega$).

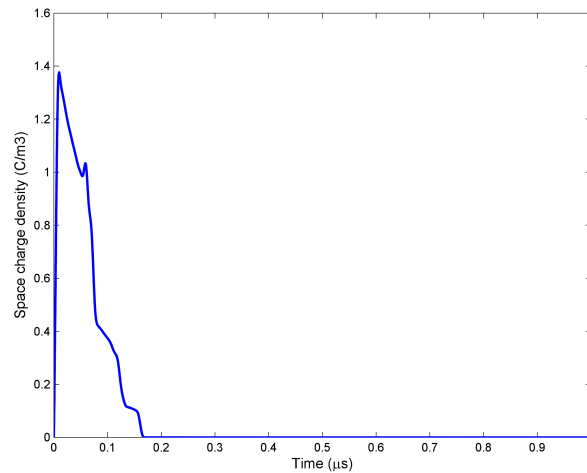


Figure 5.9: Space charge density on the tip of the corona point versus time for the pulse voltage ($R_{ext} = 50M\Omega$).

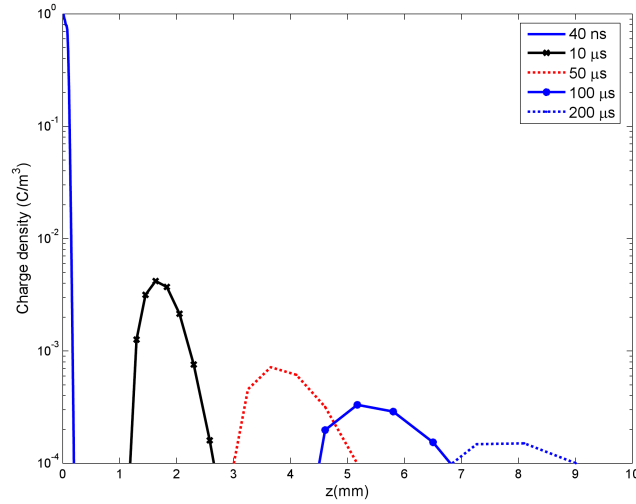


Figure 5.10: Charge density along the axis for five different time instants after the first voltage pulse ($R_{ext} = 50M\Omega$).

decreased due to radial dispersion. The other one with a larger peak value is the one resulting from the second voltage pulse. Both of these clouds move along the axis with time with the velocity of $\vec{u} = k\vec{E}$. Since the value of electric field near the tip is large and decreases along the axis, the velocity of ion cloud decreases as it gets further from the tip. The cloud closer to the tip experiences a larger electric field; it initially moves faster than the other one and this effect decreases the distance between the two pulses.

Figure 5.13 shows the corona current versus time for two subsequent voltage pulses. When the applied voltage is below the corona onset level the corona discharge stops. In this period, the DC voltage (4kV in our case) produces an electric field, which moves the existing charges towards the ground producing a small DC current. The peak value of successive current pulses decreases only slightly from $48.8 \mu\text{A}$ to $48.4 \mu\text{A}$. The decrement in the current peak in successive pulses results from the fact that as time goes on, the space charge density increases in the air gap. This increment of the space charge decreases the electric field and decreases the peak of successive

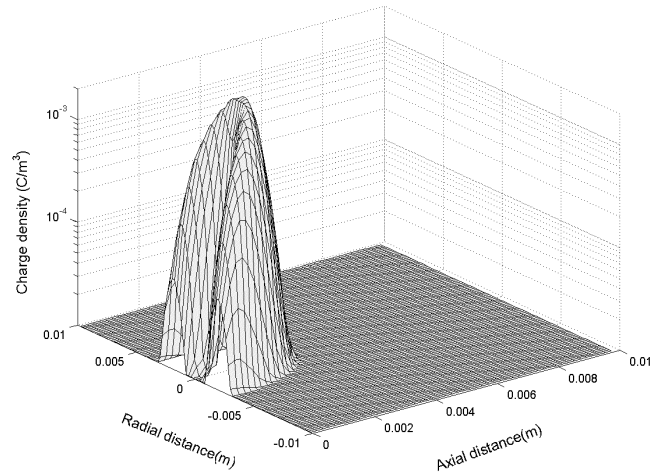


Figure 5.11: Charge distribution in the space for a pulse energization at $t = 10 \mu\text{s}$ ($R_{ext} = 50M\Omega$).

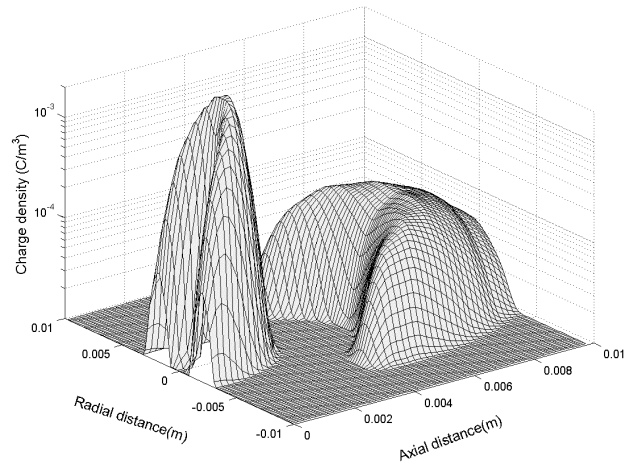


Figure 5.12: Charge distribution in the space for a pulse energization at $t = 210 \mu\text{s}$ ($R_{ext} = 50M\Omega$).

pulses of corona current.

To better show the effect of space charge on the peak value of current with time, the frequency of the pulse was increased from 5 kHz to 50 kHz. Figure 5.14 shows the corona current versus time for five applied voltage pulses. The current peak values are 48.8, 47, 45.8, 45, 42.5 μA , respectively.

The average current in each case has been also calculated using the formula:

$$I_{av} = \frac{1}{T_p} \int_0^{T_p} I dt$$

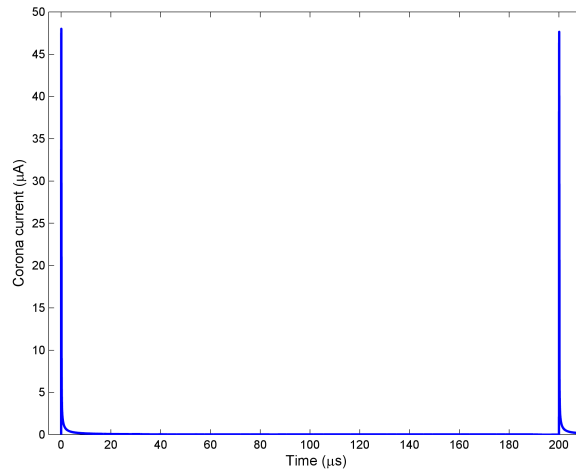


Figure 5.13: Corona current versus time for a pulse energization, ($f = 5\text{kHz}$, $R_{ext} = 50\text{M}\Omega$)

This value is calculated to be 0.073 μA and 0.56 μA for $f=5\text{kHz}$ and $f=50\text{kHz}$, respectively. As expected, the average current increase as the frequency is increased although not in direct proportion.

Figure 5.15 shows the distribution of the space charge density after the third pulse (at $t=41\ \mu\text{s}$) in the entire air gap for frequency $f=50\text{kHz}$. At this time, three pulses have been applied to the corona electrode. This Figure shows that if the

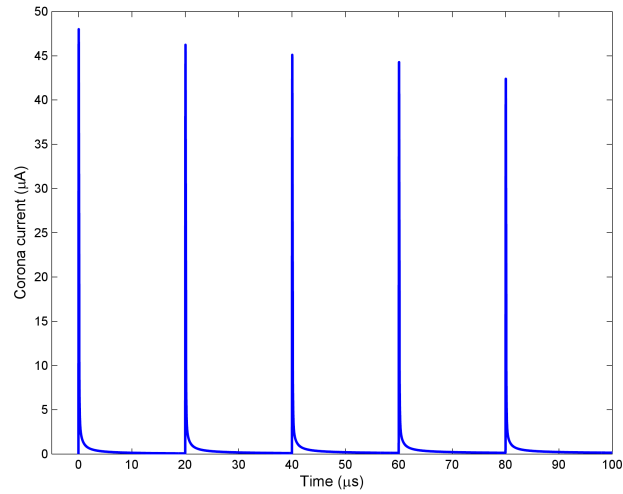


Figure 5.14: Corona current versus time for a pulse energization, ($f = 50kHz$, $R_{ext} = 50M\Omega$)

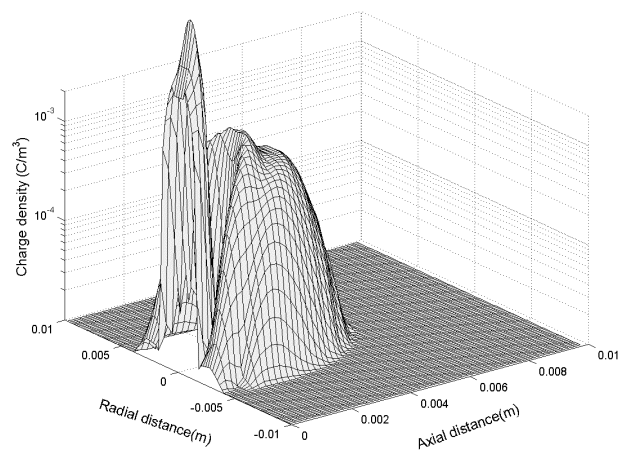


Figure 5.15: Charge distribution in the space between both electrodes at $t=41 \mu s$

frequency of the applied voltage is too high, the charge pulses will practically combine. This effect can be explained by both physical and numerical diffusions in the system. While FCT should theoretically remove an artificial diffusion introduced to stabilize the iteration process, some portion of this diffusion remains in the model, which can be responsible for collapsing of adjacent charge clouds.

5.4 Conclusions

In this Chapter, a hybrid FEM-FCT dynamic model has been applied for simulating a dynamic single-species electric corona discharge model. The results show the behaviour of the corona current and space charge density for two different waveforms of the applied voltage: step and pulse.

When a step voltage is applied to the corona electrode, the total corona current and space charge density have large values at $t=0$ but they decrease quickly to a constant value at steady state. It was also shown that, as expected, a larger input voltage results in a larger current in the circuit and the value of current is larger for smaller external resistance.

When a periodic pulse voltage is applied to the corona electrode, the resulting current will be periodic too. The average current depends on the frequency and increases as the frequency of pulses increase. It was shown that the peak value of these sequential current pulses decreases. This results from the fact that as time goes on, space charge is accumulated in the air gap and increased space charge decreases the value of electric field. A decrease in electric field value results in decreasing the peak of successive pulses of the corona current. When a pulse voltage is applied, the current increases quickly to a peak value and then decreases to a small DC value

when the applied voltage is below the corona onset voltage. The charge clouds are formed in the air gap and move towards the ground plate. The velocity of these charge pulses depends on the electric field magnitude. Therefore, as they move, their velocity decreases due to the decrease in the electric field along the axis. It follows that if the frequency of the applied pulse voltage is too high, charge pulses will eventually combine.

Chapter 6

Two dimensional Simulation of Trichel Pulses in Air

6.1 Introduction

In the previous Chapter, the proposed numerical technique was applied to a single-species model of corona discharge. The results were compatible with the physical expectations and it was realized that the technique is working correctly. Since the properties of Trichel pulses are determined by the processes occurring in the active zone, it is necessary to use at least a three-species model in order to include the ionization layer in the calculations. In this Chapter, the technique discussed in this thesis is used for simulating the Trichel pulse regime of corona discharge using a three-species model. The series of Trichel pulses for different applied voltages are successfully reproduced. In addition, the electron and ion densities and the electric field distributions at the different stages of Trichel pulses are presented.

6.2 Basic Equations

The model proposed in this section is two-dimensional (to be precise, 3D with axial symmetry). This means that both the axial and radial development of the discharge is considered. It is assumed that the ionization characteristics of the gas are determined by the local reduced electric field E/N where E is the electric field and N is the neutral gas number density. For simulating the pulse mode of the negative corona discharge in point-to-plane configuration, solving continuity equations for electrons, positive ions and negative ions along with the Poisson equation is necessary. These equations are shown below:

$$\frac{\partial N_e}{\partial t} + \nabla \cdot (N_e \vec{W}_e - D \nabla N_e) = (k_i - k_a) N_e - \beta_{ep} N_e N_p \quad (6.1)$$

$$\frac{\partial N_p}{\partial t} + \nabla \cdot (N_p \vec{W}_p) = k_i N_e - \beta_{ep} N_e N_p \quad (6.2)$$

$$\frac{\partial N_n}{\partial t} + \nabla \cdot (N_n \vec{W}_n) = k_a N_e \quad (6.3)$$

$$\nabla \cdot \vec{D} = (N_p - N_e - N_n) \quad (6.4)$$

where,

$$\vec{W}_e = \mu_e \vec{E}, \quad \mu_e = 0.05 m^2 / V \cdot s \quad (6.5)$$

$$\vec{W}_p = \mu_p \vec{E}, \quad \mu_p = 2.24 \times 10^{-4} m^2 / V \cdot s \quad (6.6)$$

$$\vec{W}_n = \mu_n \vec{E}, \quad \mu_n = 2.16 \times 10^{-4} m^2/V \cdot s \quad (6.7)$$

k_i and k_a are the ionization and attachment coefficients and are equal to [99]:

$$k_i = 10^{11.93 - \frac{449.3}{EN}} (1/s)$$

$$k_a = 6 \times 10^6 (1/s)$$

$EN = \frac{E \times 10^{21}}{NO_2}$; E is the magnitude of electric field in V/m and NO_2 is the number density of oxygen molecules which is approximately equal to $2.46 \times 10^{25} (1/m^3)$ under standard pressure and at room temperature [100].

β_{ep} is the electron-positive ion recombination coefficient and is equal to [99]:

$$\beta_{ep} = 5 \times 10^{-13} (m^3/s)$$

D is the diffusion coefficient of electrons [100].

6.3 Boundary Conditions

The corona electrode and ground are equipotential. Therefore, the boundary conditions for voltage are:

$$V = V_{applied} - IR_{ext} \text{ on the corona electrode.}$$

$$V = 0 \text{ on the ground plate.}$$

The equations for negative and positive ions are of the first order. Therefore, the boundary conditions for these species are:

$$N_p = 0 \text{ on the ground plane.}$$

$N_n = 0$ on the corona electrode.

Since the charge continuity equation for electrons is a second order differential equation, it needs two boundary conditions. The first condition is that the normal derivative of electron density is zero on the ground electrode. The value of electron density at different points of the corona electrode is the second required boundary condition and is obtained using the secondary electron emission,

$$N_{ec} = \gamma N_{pc} \frac{\mu_p}{\mu_e}$$

where γ is the secondary electron emission coefficient and is estimated to be equal to 0.01 [30].

6.4 Numerical Algorithm

For the charge continuity equations, a combination of FEM and FCT (as explained in Chapter 4) proved to be a feasible technique. In this technique, artificial oscillations in the calculated results which occur when a classical FEM approach for the charge transport equations is used are removed using a three step procedure [101].

The simulation is performed by developing a code using C programming language. Linux platform is chosen for compiling and running the code. Initially, a small initial space charge density of electrons in the air gap was assumed, which represents typical background ionization. The electric field is calculated by solving Poisson equation and is substituted into the charge continuity equations to determine densities of ionic species. This internal loop is iteratively repeated until both the

electric potential and charge densities are convergent. The convergence criteria for this inner loop are as follows:

$$\frac{\sum_i \left(N_i^k - N_i^{k-1} \right)^2}{\sum_i \left(N_i^k \right)^2} < \delta_1 \quad (6.8)$$

$$\frac{\sum_i \left(V_i^k - V_i^{k-1} \right)^2}{\sum_i \left(V_i^k \right)^2} < \delta_2 \quad (6.9)$$

where i stands for electrons (e), negative ions (n) and positive ions (p).

Then, using the obtained electric field and charge densities distributions, total corona current is calculated using Sato's formula. The termination criterion of this outer iterative loop (current calculation loop) was that the change of the drift current in two successive iterations was less than δ_3 as given in (6.10). This condition was used to check the convergence of the corona electrode voltage which changes due to the voltage drop on the external resistor.

$$\left| \frac{I_{k+1} - I_k}{I_{k+1}} \right| \leq \delta_3 \quad (6.10)$$

δ_1 , δ_2 and δ_3 were chosen arbitrarily, but were tested to give accurate results in a reasonable time period. Therefore, they were assumed to be 0.01 in our calculations.

When the electric field and space charge densities were found for one time step, the electron density on the corona electrode was updated from the secondary electron

conditions. The same process was then repeated for all the time steps. To reduce the simulation time, the optimization technique proposed in Chapter 4 is used in the code.

Figure 6.1 illustrates the non-uniform FE grid used in the simulation. The element size close the corona electrode is in the order of $5 \mu\text{m}$. This element size is proved to be adequate for accurate estimation of charge and field distributions close to the corona electrode.

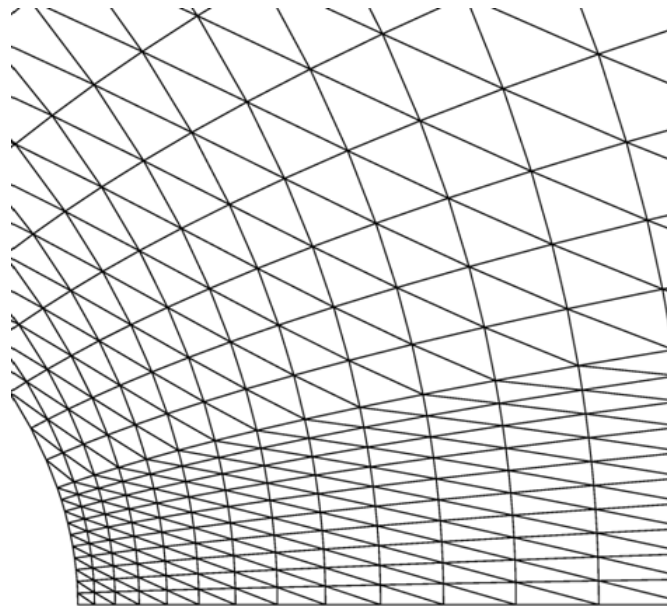


Figure 6.1: Details of FE grid near corona electrode used in the simulation process.

6.5 Current Components

There are two components of current which need to be superimposed to yield the total current in the circuit: corona current and displacement current.

Corona current is produced due to the movement of charges (electrons and ions) and it is obtained from the formula [98]:

$$I = \frac{1}{V_c} \int \int \int \left(N_p \vec{W}_p - N_n \vec{W}_n - N_e \vec{W}_e \right) \cdot \vec{E}_L dv \quad (6.11)$$

where V_c is the voltage of the corona electrode and \vec{E}_L is the Laplacian electric field.

The other component of the current is the displacement current, which is created due to the capacitive behaviour of the needle-plane geometry. Figure 6.2 shows the circuit model of the needle-plane configuration. In this circuit, the external resistance R_{ext} is assumed to be 100 k Ω and C_d the capacitance of the air gap is equal to 0.055 pF. The capacitance value is calculated by integrating the total charge in the air gap and dividing the derived value by the applied voltage. Equations (6.12) and (6.13) are used for calculating the voltage between the needle and plane, and the displacement current, respectively. The total current is the sum of the displacement current (i_d) and the corona current (i_c).

$$\frac{dV_c(t)}{dt} = \frac{1}{R_{ext}C_d} (V_{app} - R_{ext}i_c) - \frac{1}{R_{ext}C_d} V_c(t) \quad (6.12)$$

$$i_d = C_d \frac{dV_c}{dt} \quad (6.13)$$

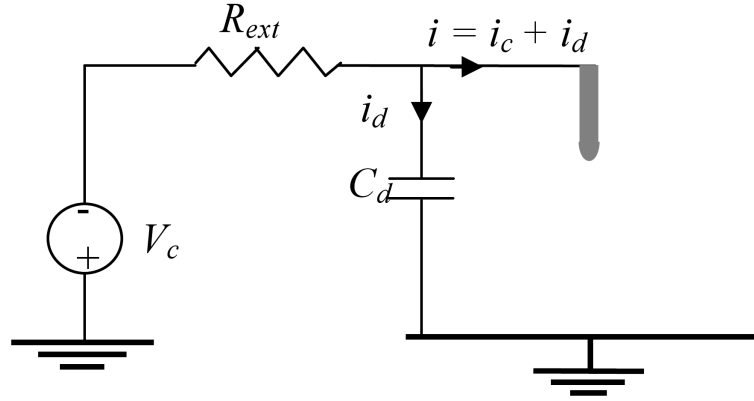


Figure 6.2: Circuit model of the needle-plane configuration.

6.6 Results

The hyperbolic needle is 1cm long ($L=1\text{cm}$) and is placed 1cm from the ground plate ($d = 1\text{cm}$). The radius of curvature R of the tip of the needle is $100\ \mu\text{m}$. At the room temperature and atmospheric pressure the corona onset voltage for this configuration evaluated from experimental Peek's formula is equal to $-4.7\ \text{kV}$. The capacitance of the needle-plane is calculated and is equal to $0.055\ \text{pF}$, and the stray capacitance of the external resistance is disregarded.

In this section, the results of the numerical analysis showing a series of Trichel pulses for different applied voltages are presented. The behaviour of the electric field and charge densities during one Trichel pulse is closely investigated. The distributions of charge densities along the axis of symmetry are compared at six different stages of one steady-state pulse: i.e. at the beginning, half-pulse rising slope, maximum, half-pulse decreasing slope, after the pulse finishes, and after an approximate steady-state is reached. The electric field distributions along the axis are also presented.

6.6.1 Applied Voltage = -8kV

A voltage of -8kV was applied to the needle-plane system and the corona current versus time curve is plotted in Figures 6.3 to 6.5. Six sequential pulses are shown in these Figures. The time differences between subsequent pulses are: 14.35 μs , 8.75 μs , 9.61 μs , 10.4 μs and 10.88 μs . Therefore, after some initial variations, the Trichel pulses become rather regular. The peak currents of the pulses are approximately: 15 mA, 1.8 mA, 2.04 mA, 1.72 mA, 1.71 mA and 1.73 mA.

It was observed that the first pulse in the series of Trichel pulses always has a different behaviour. Its amplitude is much larger than the rest of the pulses and the time interval between the first and second pulse is usually longer than the period between pulses in steady-state. This difference in behaviour can be explained by the fact that the first pulse is always produced in a charge-free space. There is no significant negative charge in the space to suppress the electric field in the ionization region. As a result, the maximum value of the electric field for the first pulse is larger than its value for the rest of the pulses. Therefore, the avalanche ionization is more intense and the total number of electrons and positive ions which are created due to the avalanche ionization is larger resulting in a larger corona current for the first pulse.

With regard to the time between the first and second pulses, the total number of negative ions created due to the attachment during the first pulse is larger than the total number of negative ions created during the subsequent pulses. Therefore, these negative ions need more time to travel towards the ground plate. As a result, more time is needed for the electric field to increase above the value required for avalanche ionization and the appearance of the next Trichel pulse.

Figures 6.7, 6.8 and 6.9 show the electron density, positive ion density and negative ion density along the axis of symmetry at different time instants for one typical Trichel pulse. These time instants are shown in Figure 6.6.

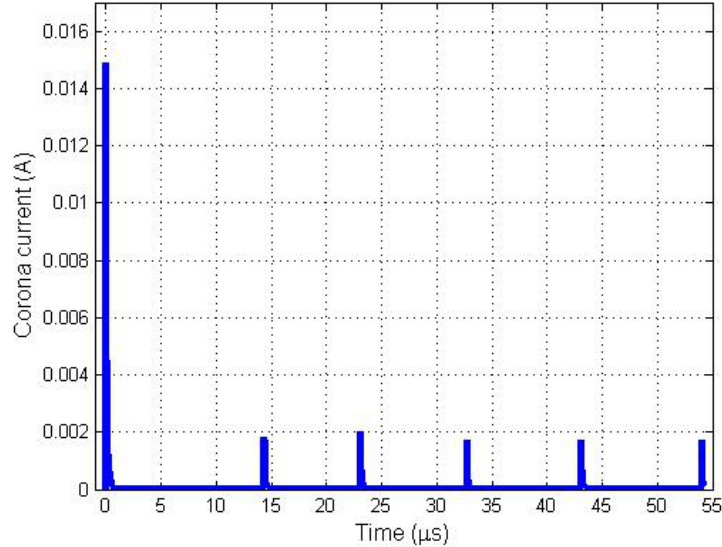
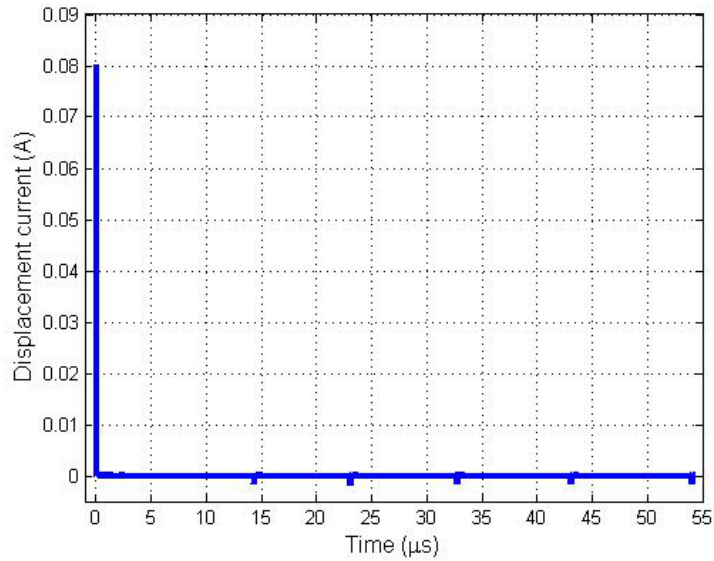
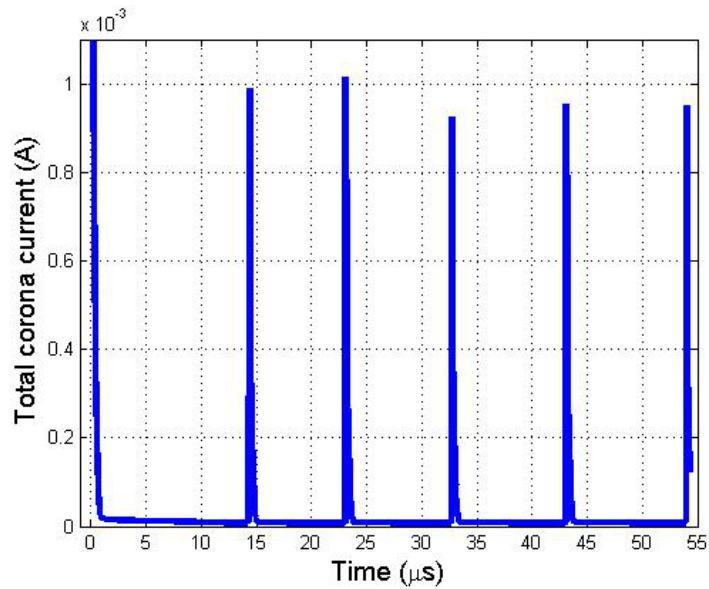


Figure 6.3: Corona current for $V = -8\text{kV}$.

As Figure 6.7 shows, electron density has very small values at the beginning of the pulse, then it starts increasing due to avalanche ionization and approximately at the half pulse rising point (point 2 in 6.6), it reaches its maximum value. The electron density then starts decreasing and practically disappears between pulses, mainly due to the attachment to neutral oxygen molecules and also because of rapid movement towards the ground due to the electric force.

Figure 6.8 shows the positive ion density along the axis of symmetry at different instants of time. The behaviour of positive ions is very similar to that of electrons. There are very few positive ions at the beginning of the pulse and then their number increases because of the avalanche ionization process. Similarly to electrons at the

Figure 6.4: Displacement current for $V = -8\text{kV}$.Figure 6.5: Total current for $V = -8\text{kV}$, the amplitude of the first pulse is approximately equal to the amplitude of the displacement current at $t=0$.

peak of the current pulse, the density of positive ions reaches their maximum value.

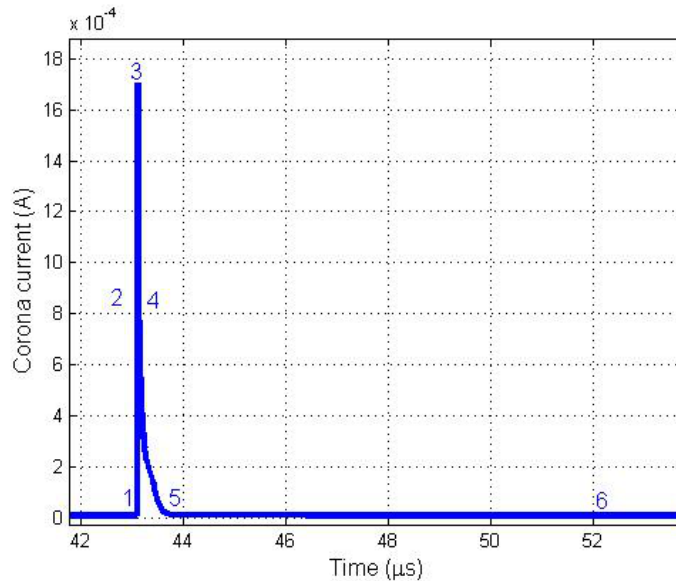


Figure 6.6: Characteristic points on a typical Trichel pulse: 1 - beginning of the pulse, 2 - half-pulse rising, 3 - maximum of the pulse, 4 - half-pulse decreasing, 5 - end of the pulse, 6 - 9 microseconds after the pulse

As soon as the positive ions appear in the air gap, the electric field force attracts them towards the corona electrode and they start being deposited on the corona electrode. The mobility of positive ions is relatively small, but since the distance they have to travel is also very small, they arrive to the corona electrode in a few nanoseconds. This deposition can be seen between point 2 and 3 on Figure 6.8. As soon as the positive ions start depositing on the corona electrode, the electric field in the ionization layer decreases and therefore the thickness of the ionization layer is reduced. The reduction of the electric field and thickness of the ionization layer, limits the avalanche ionization process and it eventually stops when practically all positive ions are deposited on the corona electrode.

Figure 6.9 shows the negative ion density along the axis of symmetry at different

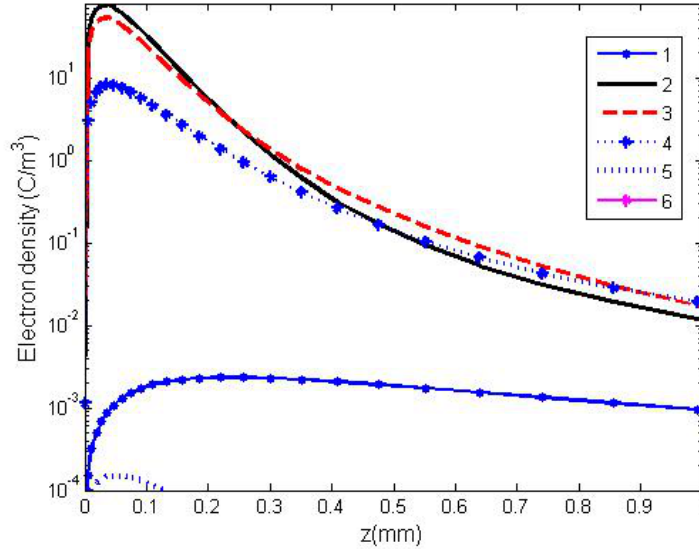


Figure 6.7: Electron density along the axis of symmetry at different instants during a Trichel pulse (In figures 6.7, 6.8 and 6.9, the minimum scale on y axis is chosen to be 0.0001 and the values below this level are considered as noise. Therefore the curves which do not exist in these figures are in the noise level).

time instants. As this figure shows, the negative ion density increases with time due to the attachment of electrons to neutral molecules. The electric field pushes the negative ions towards the ground plate but their velocity is relatively small and the distance they have to travel is much longer than the distance for the positive ions. This explains the reason for a very long time between Trichel pulses (in comparison with the Trichel pulse width). The existence of negative ions in the air gap decreases the electric field between the cloud and corona electrode. Therefore, it delays the time for the electric field to once again reach the threshold value required for the avalanche ionization and the creation of a new Trichel pulse. The negative ions must move far enough from the corona electrode before a new pulse can develop.

Figure 6.10 shows the electric field intensity along the axis of symmetry at different time instants during one Trichel pulse. At the beginning of the pulse, the

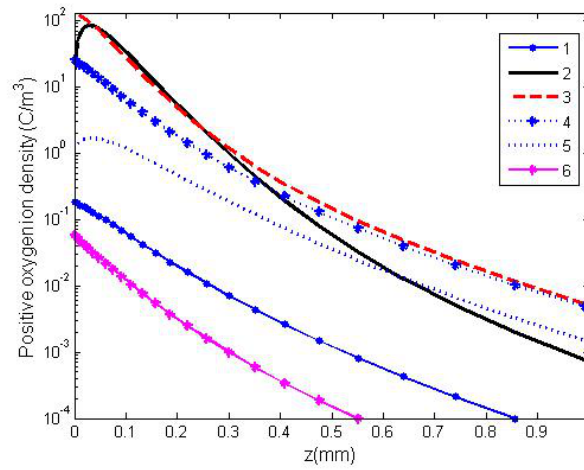


Figure 6.8: Positive ion density along the axis of symmetry at different instants during a Trichel pulse.

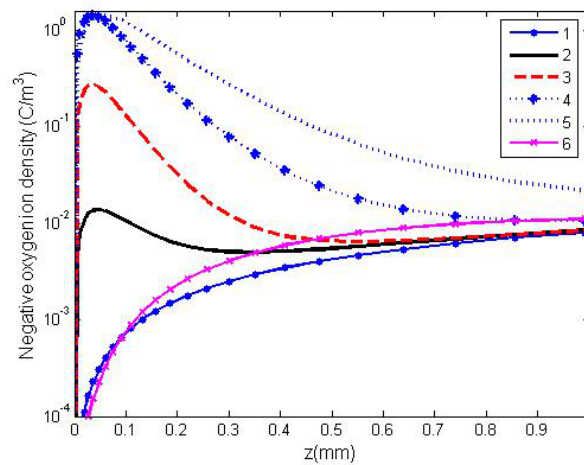


Figure 6.9: Negative ion density along the axis of symmetry at different instants during a Trichel pulse.

electric field is large enough for the avalanche ionization to start. At point 2, which is the half-pulse rising point, the positive ion and negative ion clouds are already created. The positive ion cloud which is closer to the corona electrode increases the electric field value in that area. Between the positive ion cloud and the negative ion cloud the electric field decreases (curve 2). At point 3, which is the maximum of the pulse, all the positive ions have been removed from the air gap and, therefore, the electric current starts decreasing. The minimum of electric field is at a point between the negative and positive ion clouds. Comparing curves 2 and 3 of Figure 6.10, it is clear that the position of minimum electric field has not practically moved, so the negative ion cloud has not practically moved and the distance of the point of maximum negative charge density from the corona electrode is constant at about 0.04mm. At this point the electric field in the ionization layer has dropped below the threshold value and the avalanche ionization has stopped.

The negative ions then very slowly move towards ground. At point 6, which is 9 μs after the pulse, the negative ions have traveled considerably along the axis and electric field near the corona electrode has increased. These ions continue to move towards the ground electrode and the electric field at the corona electrode increases until the next pulse appears. This process repeats and the pulses are rather regular.

6.6.2 Applied Voltage = -10kV

Figure 6.11 shows the series of Trichel pulses for the applied voltage of -10kV. The amplitudes of subsequent pulses are approximately: 21.1 mA, 2.64 mA, 2.12 mA, 1.78 mA, 1.71 mA and 1.78 mA. Distances between subsequent pulses are: 15.75 μs , 4.86 μs , 6.33 μs , 6.77 μs and 6.83 μs .

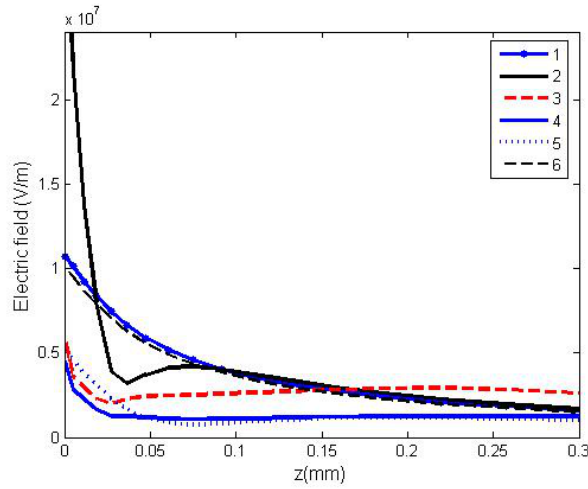


Figure 6.10: Electric field along the axis of symmetry at different instants during a Trichel pulse.

By comparing the period of the Trichel pulses for -8 kV and -10 kV, it can be seen that the frequency of these pulses increases with increasing the applied voltage. This agrees with the trend observed in the previously reported experimental results [26].

Figures 6.12, 6.13 and 6.14 show the total number of electrons, negative ions and positive ions in the air gap as a function of time. These quantities are obtained using the following formulae:

$$\text{Total electron charge} = \int \int \int N_e dv$$

$$\text{Total negative charge} = \int \int \int N_n dv$$

$$\text{Total positive charge} = \int \int \int N_p dv$$

As it can be seen, the total number of electrons and positive ions between pulses is very small. Only during the Trichel pulse occurrence there is sudden generation of new charges. The negative ions are present in the air gap practically all the time, with a steady decrease between pulses and fast increase shortly after the pulse.

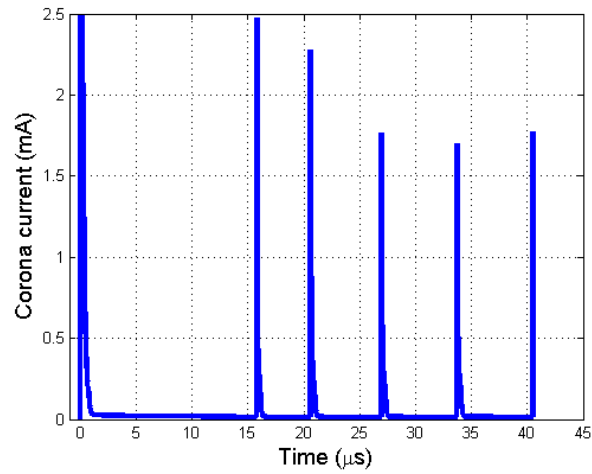
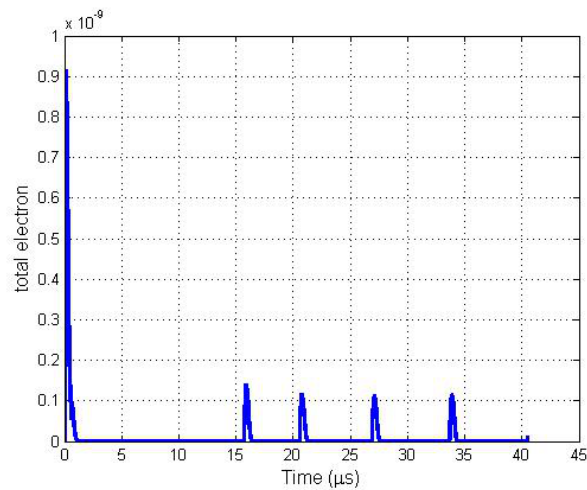
Figure 6.11: Trichel pulse for $V=-10\text{kV}$.

Figure 6.12: Total electron charge in the air gap versus time.

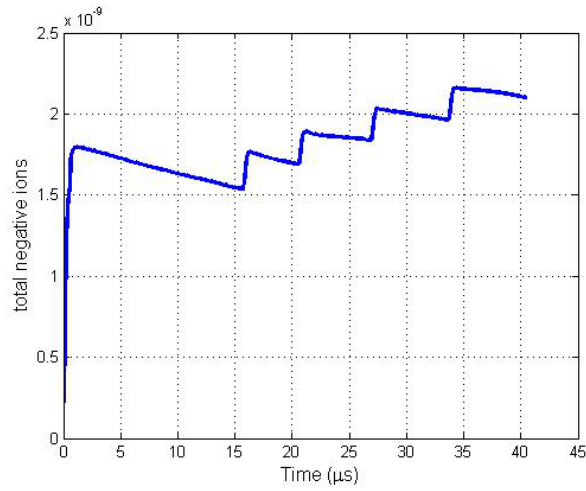


Figure 6.13: Total negative ion charge in the air gap versus time.

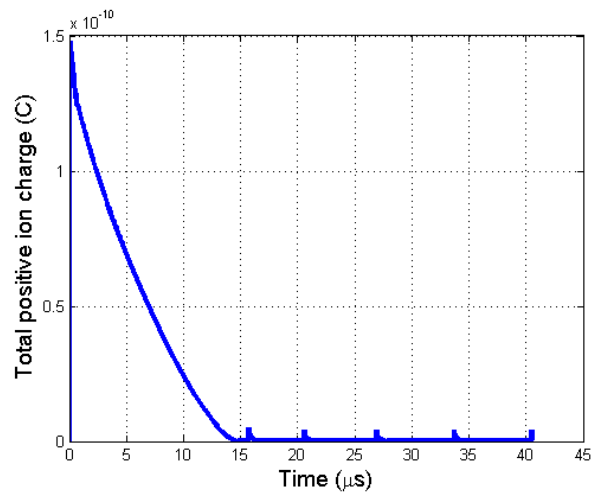


Figure 6.14: Total positive ion charge in the air gap versus time.

6.7 Conclusions

In this Chapter, a new two-dimensional FEM-FCT based model for three-species simulation of Trichel pulses in air has been described. The model has successfully reproduced a series of Trichel pulses for different applied voltages and the pulse formation was explained by showing the densities of electrons, ions and the electric field distributions along the axis of symmetry. To the best of our knowledge, this is the first time the FEM-FCT based technique has been successfully applied for the 2D simulation of Trichel pulses for different applied voltages.

Chapter 7

A Parametric Study on Trichel Pulse Characteristics

7.1 Introduction

In Chapter 6, a basic investigation of Trichel pulses was presented. In this Chapter, the 2D three-species numerical model presented in Chapters 3 and 4 is used for more systematic study of the negative corona discharge in air. The effect of different parameters of the discharge system such as external resistance R_{ext} secondary electron emission γ ion mobilities and pressure P on the properties of Trichel pulses (T , $I_{average}$) will be discussed.

In order to make this process possible in a reasonable time, only the first six Trichel pulses were simulated for each case.

7.2 Effect of Different Parameters on Trichel Pulse Characteristics

7.2.1 External Resistance

A ballast resistor usually exists between the voltage source and the corona electrode and it is intended to:

- protect the elements of the circuit in the case of spark discharge or short-circuit in the air gap,
- limit the amount of current in the electric circuit. When the total current increases, the voltage drop on the ballast resistor increases reducing the voltage applied to the corona electrode and thus reducing the applied field and gas ionization.

In this section, the Trichel pulse characteristics: average pulse period, standard deviation of the period and average corona current were investigated for three different values of the external resistance in the circuit. The results are shown in Figure 7.1. The standard deviation of the period at each applied voltage is also shown in this Figure. Figure 7.2 shows the average corona current versus applied voltage for the same values of external resistances.

From the numerical simulation data it can be observed that:

1. as the external resistance decreases the time between the first pulse and the second pulse increases (Figures 7.9 and 7.10),

2. as the external resistance decreases, the period of the pulses increases (with the exception of $V = -8\text{kV}$ case) (Figure 7.1),
3. as the external resistance decreases, the value of the maximum current increases (Figures 7.9 and 7.10).

To explain the reasons for these observations, Figures 7.3 to 7.10 are presented. These Figures show the total charge of positive ions, electrons and negative ions, and the corona current for two different values of the external resistance. By comparing the corresponding Figures for $R_{ext} = 10 \text{ k}\Omega$ and $R_{ext} = 100 \text{ k}\Omega$ it is clear that total charge of positive ions and electrons created in the case of a smaller resistance are much larger than the total charge of the same species created in the case of a larger resistance. Subsequently, these ions need more time to migrate towards the ground plate. Therefore, the average period of the pulses increases as the external resistance decreases. Since for smaller external resistances the voltage drop is smaller, a larger voltage is applied to the corona electrode and it creates a stronger electric field. Therefore, more charge is needed to reduce the electric field below the ionization level. For the same reason, the time interval between the first two pulses for smaller external resistances is much larger than the time interval between the first two pulses for larger resistances.

As the average period of pulses increases, the average corona current decreases. The reason is that even though the peak values of current are larger, a longer period means a greater time interval at which the corona current has very small values. Therefore, the average corona current is smaller.

Table 7.1: Trichel pulse characteristics for different applied voltages, $R_{ext} = 100 \text{ k}\Omega$

Voltage	$-7kV$	$-8kV$	$-9kV$	$-10kV$
$T_{average}^*$	$13.5\mu s$	$9.9\mu s$	$6.6\mu s$	$6.2\mu s$
$I_{average}$	$13.6\mu A$	$19.0\mu A$	$28.1\mu A$	$33.3\mu A$
St. D. of $T_{average}^*$	2.09	0.81	0.61	0.80
Gallo's T	$11.3\mu s$	$8.1\mu s$	$6.1\mu s$	$4.8\mu s$
Gallo's $I_{average}$	$17.1\mu A$	$23.7\mu A$	$31.4\mu A$	$40.0\mu A$

Table 7.2: Trichel pulse characteristics for different applied voltages, $R_{ext} = 50 \text{ k}\Omega$

Voltage	$-7kV$	$-9kV$
$T_{average}^*$	$13.8\mu s$	$6.7\mu s$
$I_{average}$	$12.4\mu A$	$27.8\mu A$
St. D. of $T_{average}^*$	1.64	0.86

The effect of external resistance on the system is nonlinear. This is why the difference between Trichel pulse characteristics for $R_{ext} = 100 \text{ k}\Omega$ and $R_{ext} = 50 \text{ k}\Omega$ is not as dramatic as the difference between these two cases and the case of $R_{ext} = 10 \text{ k}\Omega$. It seems that there is a critical value for external resistance below which its effect on the system becomes more important.

7.2.2 Ion Mobility

The pulsating nature of Trichel pulses is caused by the finite time it takes for ionic species to drift across the air gap. This time is directly related to the drift veloc-

Table 7.3: Trichel pulse characteristics for different applied voltages, $R_{ext} = 10 \text{ k}\Omega$

Voltage	$-7kV$	$-8kV$	$-9kV$	$-10kV$
$T_{average}^*$	$17.1\mu s$	$9.2\mu s$	$9.1\mu s$	$7.7\mu s$
$I_{average}$	$11.7\mu A$	$19.8\mu A$	$25.8\mu A$	$32.9\mu A$
St. D. of $T_{average}^*$	1.34	0.88	0.35	1.62

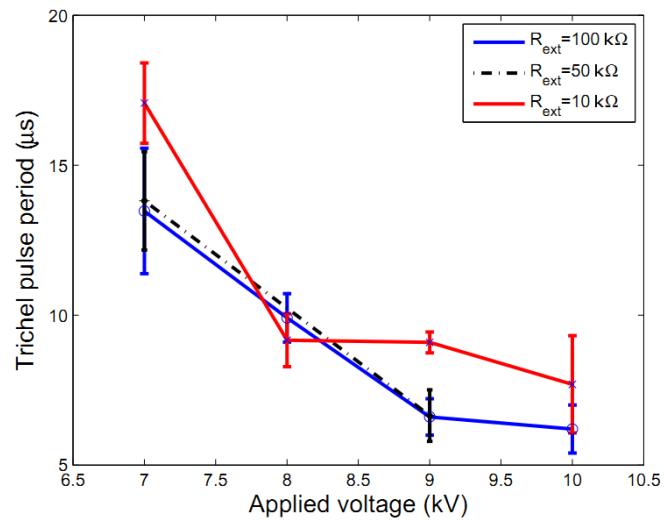


Figure 7.1: Trichel pulse period versus applied voltage for different external resistances

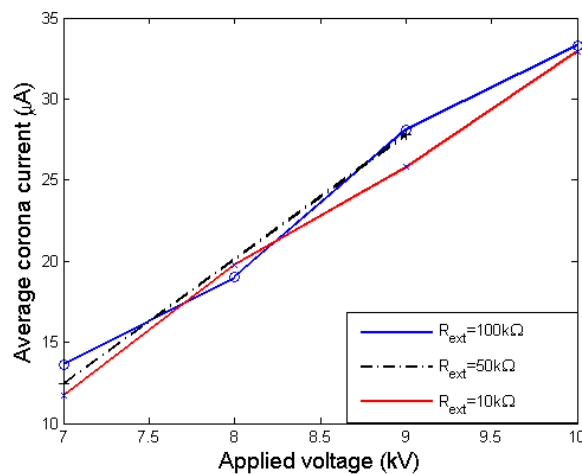


Figure 7.2: Average corona current versus applied voltage for different external resistances

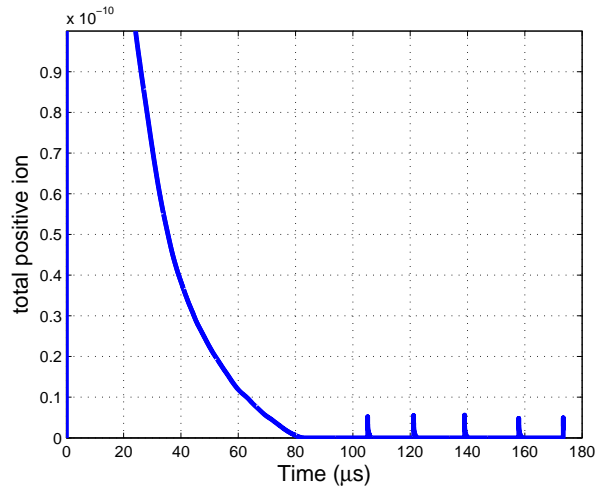


Figure 7.3: Total charge of positive ions versus time ($R_{ext} = 10k\Omega$)

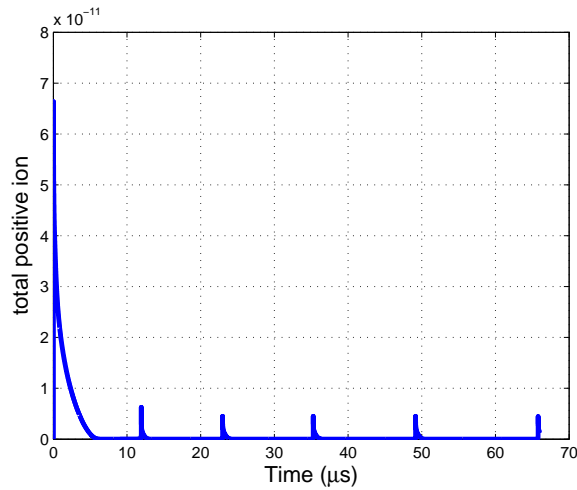
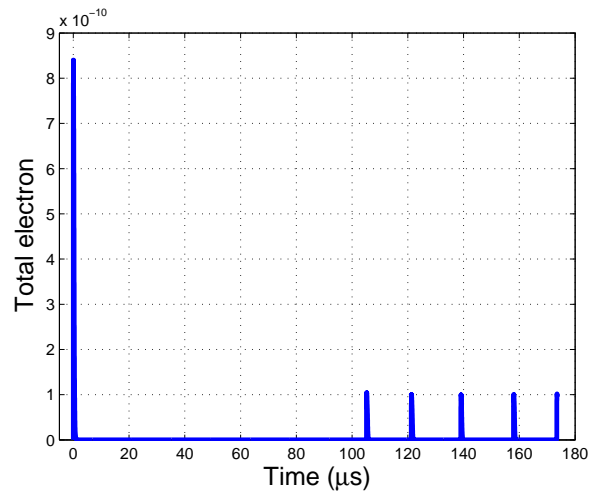
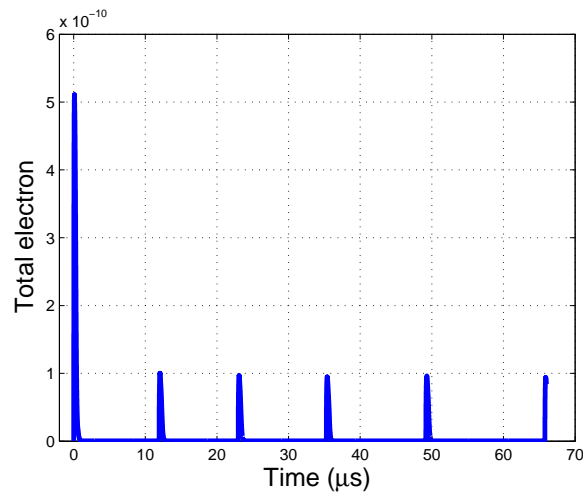
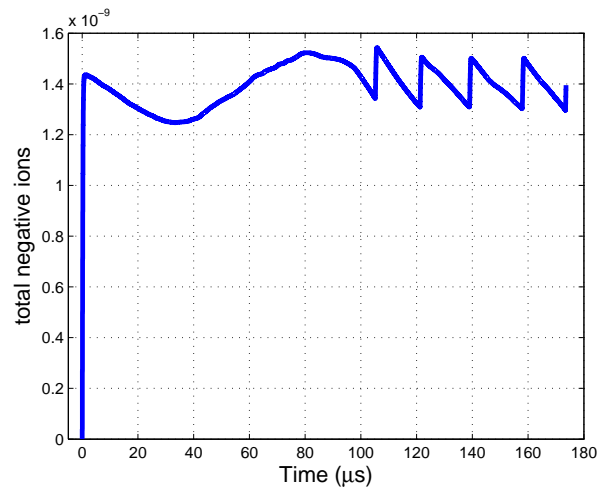
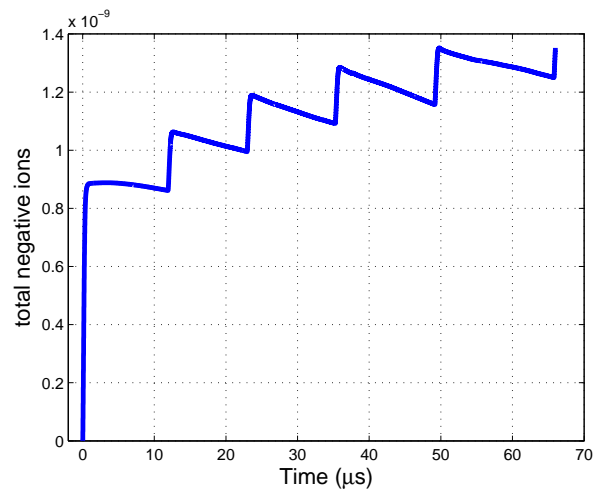


Figure 7.4: Total charge of positive ions versus time ($R_{ext} = 100k\Omega$)

Figure 7.5: Total charge of electrons versus time ($R_{ext} = 10k\Omega$)Figure 7.6: Total charge of electrons versus time ($R_{ext} = 100k\Omega$)

Figure 7.7: Total charge of negative ions versus time ($R_{ext} = 10\text{k}\Omega$)Figure 7.8: Total charge of negative ions versus time ($R_{ext} = 100\text{k}\Omega$)

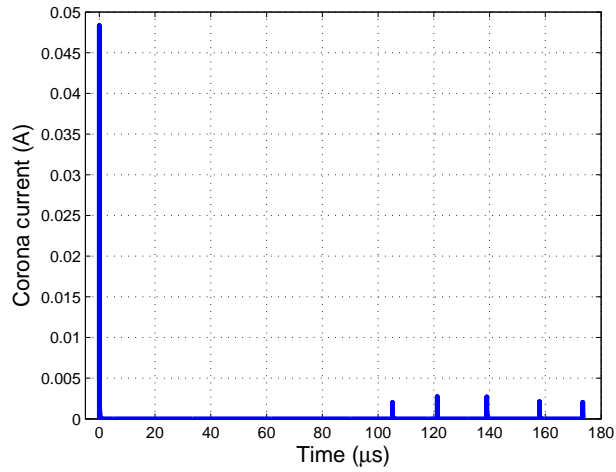
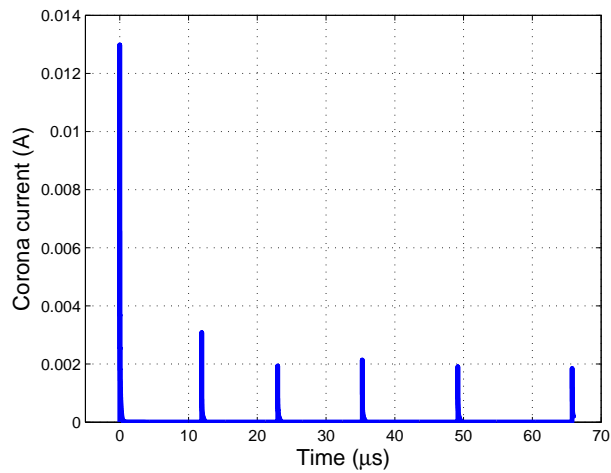
Figure 7.9: Total corona current versus time ($R_{ext} = 10k\Omega$)Figure 7.10: Total corona current versus time ($R_{ext} = 100k\Omega$)

Table 7.4: Trichel pulse characteristics for $V = -7kV$ and different ion mobilities

Ion mobilities ($m^2.V^{-1}.s^{-1}$)	$k_p = 2.24e4$ $k_n = 2.16e4$	$k_p = 1.9e4$ $k_n = 2.2e4$	$k_p = 1.9e4$ $k_n = 2e4$
$T_{average}^*$	13.5 μs	14.3 μs	14.7 μs
$I_{average}$	13.6 μA	12.7 μA	11.7 μA
St. D. of $T_{average}^*$	2.09	1.92	1.68

ity, which depends on the species mobility. Slightly different values of mobility are reported in the literature. The effect of various mobility values of the positive and negative ions on the parameters of the Trichel pulses have been studied using the presented numerical model.

It is expected that as the mobility of ions increases, they move faster and the period of the pulses will decrease and therefore the average corona current will also increase. This is confirmed by numerical results presented in Table 7.4.

7.2.3 Secondary Electron Emission Coefficient

Secondary electron emission coefficient relates the number of electrons emitted from the corona electrode to the number of positive ions impacting this electrode

$$N_{ec} = \gamma N_{pc} \frac{\mu_p}{\mu_e}$$

where γ is the secondary emission coefficient.

In the literature, the value of the secondary electron emission coefficient is assumed to be approximately 0.01. Investigating the effect of this coefficient on Trichel pulse characteristics seems to be important. Table 7.5 shows the effect of increasing this coefficient while Figure 7.11 shows Trichel pulse period versus γ . The standard deviation of the period is also shown with a bar at each point. Figure 7.12 shows the average corona current versus secondary electron emission coefficient. As

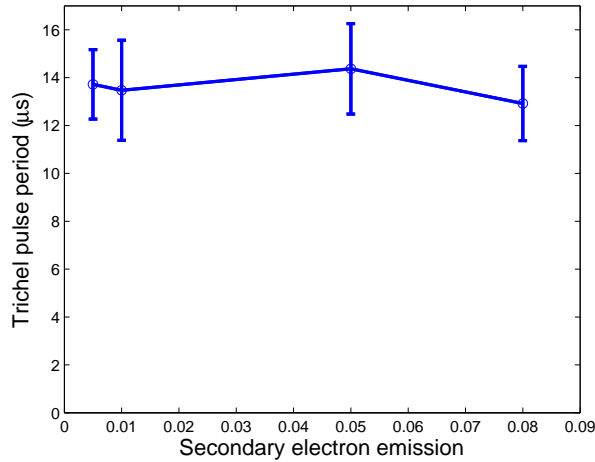


Figure 7.11: Trichel pulse period versus secondary electron emission coefficient

Table 7.5: Trichel pulse characteristics for different secondary emission coefficients,
 $V = -7kV$

Γ	0.005	0.01	0.05	0.08
$T_{average}^*$	$13.7\mu s$	$13.5\mu s$	$14.4\mu s$	$12.9\mu s$
$I_{average}$	$13.2\mu A$	$13.6\mu A$	$12.3\mu A$	$14.1\mu A$
St. D. of $T_{average}^*$	1.45	2.09	1.89	1.55

the Table and Figures show, the value of this coefficient does not seem to have any significant effect on the Trichel pulse characteristics.

7.3 Spatial Distribution of Ionic Species in Air Gap

In order to have a 3D visualization of the distribution of charge carriers during a Trichel pulse, the distributions of electrons and negative and positive oxygen ions at a specific time instant in the entire air gap are shown in this section. For a specific system configuration, five pulses are generated and at the half-pulse rising time of the 5th pulse, the 3D distribution of electron density, negative ion density and positive ion densities are shown in Figures 7.13 to 7.15. At this point a very dense cloud

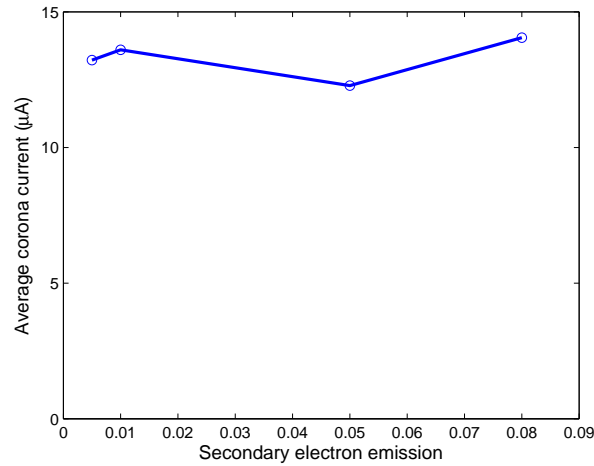


Figure 7.12: Average corona current versus secondary electron emission coefficient

of electrons and positive ions created due to the avalanche ionization exist near the corona electrode. However, since at this point the attachment process has not started yet, the density of negative ions is much smaller than other species and negative ions are composed of several clouds in the air gap. These clouds are created due to the previous pulses which drift in the axial direction, but are not yet deposited on the ground.

7.4 Shape of Ionization Layer

In this section, the thickness of ionization layer along the axis of symmetry versus time and 2D profiles of this layer in the air gap are shown during one Trichel pulse for the applied voltage of $V = -9$ kV, assuming an external resistance of $R_{ext} = 100$ k Ω and normal pressure of 1 atm (Figure 7.16).

In this case, the thickness of ionization layer along the axis is defined as the distance from the corona electrode to the point at which the ionization coefficient is equal to the attachment coefficient. Figures 7.17 and 7.18 show the thickness of this

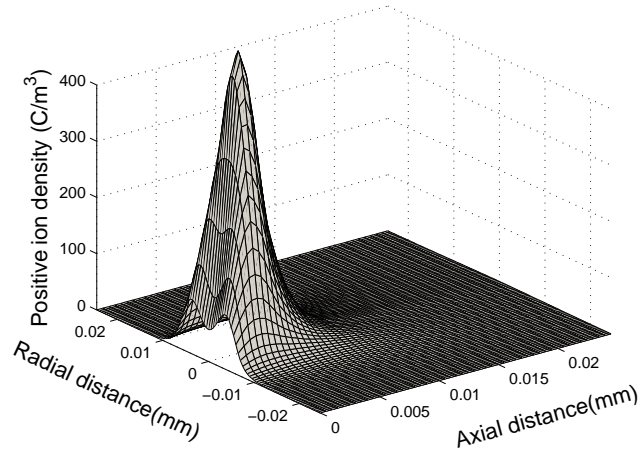


Figure 7.13: Positive ion density at point P1

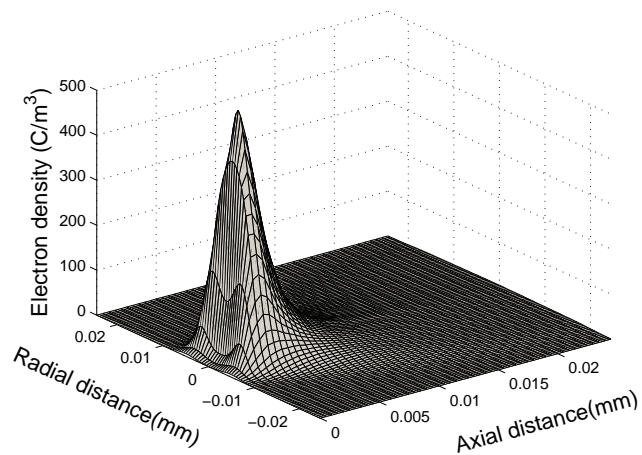


Figure 7.14: Electron density at point P1

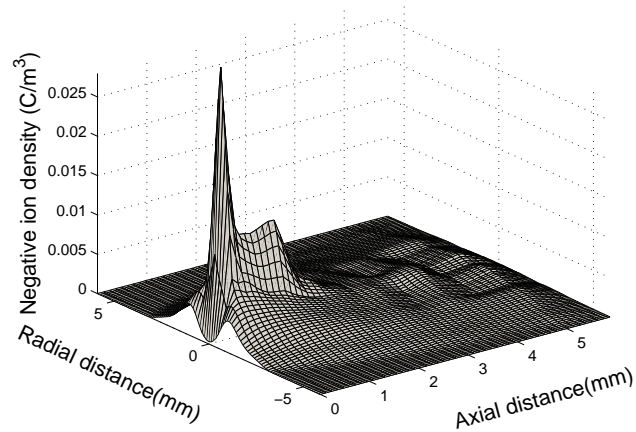


Figure 7.15: Negative ion density at point P1

layer along the symmetry axis and electric field on the corona electrode tip versus time respectively. The ionization coefficient is related to the electric field, therefore, the variation of the electric field and ionization layer thickness has similar profiles.

Figure 7.19 shows the ionization layer profile at different instants of one Trichel pulse: half pulse rising point (1), maximum current point (2), and two points in the falling section of the pulse (points 3 and 4). At points 1 and 2, the ionization layer thickness is the largest. However, at point 2 the ionization stops on the tip of the corona electrode. The diminishing of this layer gradually continues with time along the electrode surface until ionization completely stops in the entire air gap.

7.5 Conclusions

In this Chapter, the 2D three-species numerical model, presented in previous Chapters (Chapters 4 and 6) is used for simulating the negative corona discharge in point-plane configuration in air.

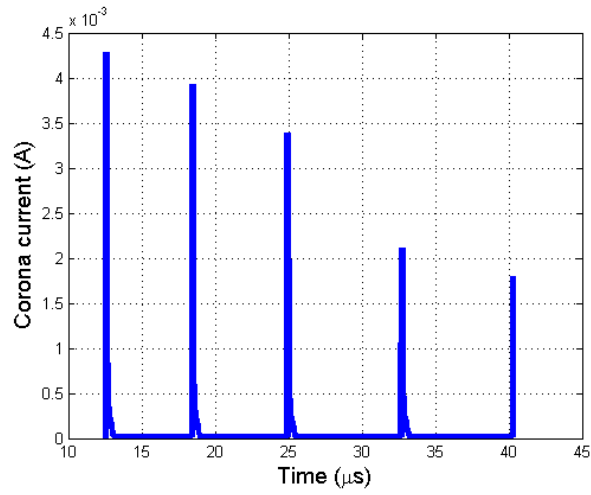


Figure 7.16: Trichel pulses for $V=-9\text{kV}$

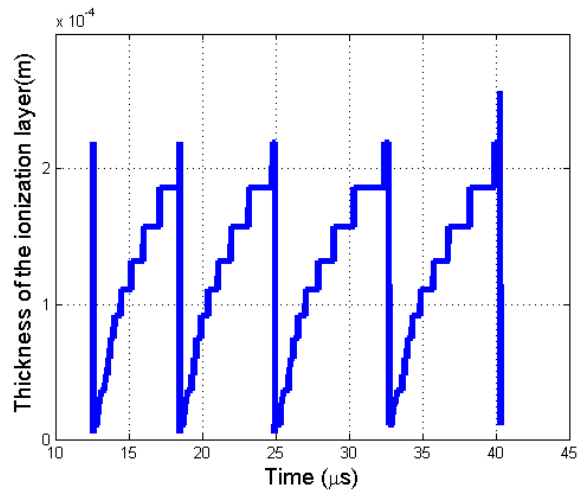


Figure 7.17: The thickness of the ionization layer

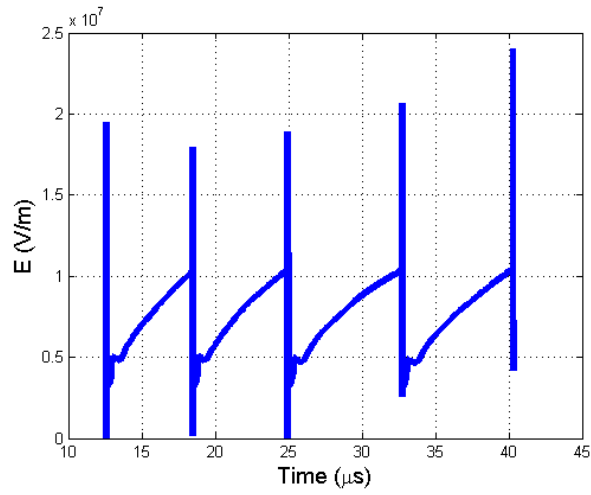


Figure 7.18: Electric field on the tip of corona electrode

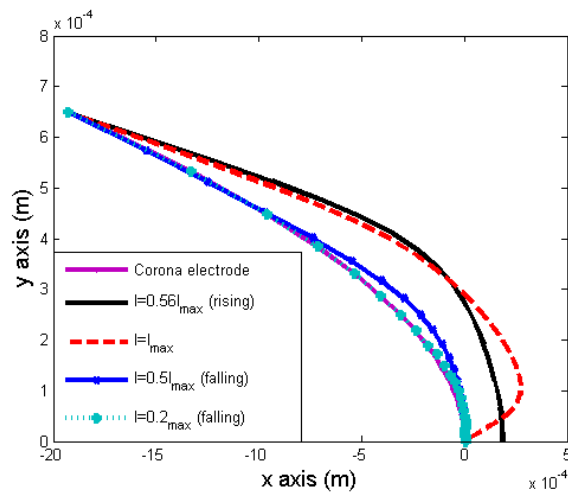


Figure 7.19: Ionization profile at different instants of time

Effect of different parameters of the corona discharge model on Trichel pulse characteristics (Trichel pulse period and the average corona current) was studied. From the numerical simulation results, it was observed that:

1. as the external resistance decreases, period of pulses increases,
2. as the external resistance decreases, average corona current decreases,
3. as the mobility of ions increases, the period of pulse decreases and therefore average corona current increases,
4. secondary electron emission coefficient does not seem to have any significant effect on Trichel pulse characteristics.

Moreover, the variation of the ionization layer in the air gap during one Trichel pulse and the ionization layer thickness along the axis versus time were shown.

Chapter 8

Experimental Verifications of the Numerical Results

8.1 Introduction

In this Chapter, some of the numerical simulation results obtained using the presented numerical technique are compared with the experimental data previously reported in the literature [26]. Moreover, the additional numerical simulation is performed for the same configurations as used in the experimental analysis and the Trichel pulse characteristics in both cases are compared. Also, the effect of pressure on Trichel pulse characteristics is studied. Finally, the effect of tip radius on the charge-per-pulse is investigated and the relation between charge-per-pulse and the average charge-per-pulse is studied. The numerical results are compared with the available experimental data if applicable [32].

8.2 Comparison With Gallo's Experimental Data

Figure 8.1 compares the Trichel pulse period for different applied voltages from the experimental data obtained by Lama and Gallo [26] with the average period of the numerical results obtained from our numerical technique. The relation between the experimental Trichel pulse frequency versus applied voltage, spacing and tip radius, was expressed analytically by Lama and Gallo as:

$$f = \frac{1}{T} \approx \frac{K_1 V (V - V_0)}{rd^2} \quad (8.1)$$

where $K_1 \approx 27kH/mm^3kV^{-2}$. The authors mentioned that K_1 is dependent on the condition of the needle-tip surface, ambient conditions, and the shape of the needle shaft and the tip. In their experimental set-up the corona onset voltage (V_0) was equal to -2.3kV comparatively independent of tip radius which is unexpected and unexplained.

Figure 8.1 shows that the numerical data follow a trend line similar to the experimental results but the numerical results considerably overestimate the pulse period. Figure 8.2 shows the average corona current versus applied voltage both from the experimental investigations and numerical simulations. Both of these figures were obtained for $r=100 \mu\text{m}$, $d=1 \text{ cm}$. Lama and Gallo obtained the following formula to describe their data on the corona current dependence on the applied voltage and spacing.

$$I \approx K_2 V (V - V_0) / d^2 \quad (8.2)$$

where, $K_2 \approx 52 \mu\text{Amm}^2 \text{kV}^{-2}$. The data is comparatively independent of tip radius which is again unexpected and unexplained.

According to (8.1) the Trichel pulse frequency is inversely proportional to the corona electrode radius and square of the gap spacing. This is quite logical because as the distance between the electrodes increases, negative ions take more time to travel towards the ground electrode. Therefore, the Trichel pulse period increases and its frequency decreases. Moreover, a sharper corona electrode (with a smaller radius of curvature) produces a larger electric field close to it. A larger electric field moves the ions faster which increases the frequency of the pulses.

In addition, (8.2) shows that the relation between the average corona current and the gap spacing is also the inverse squared. Since the Trichel pulse period is larger for larger gap spacing, it should be expected that the average corona current would be smaller.

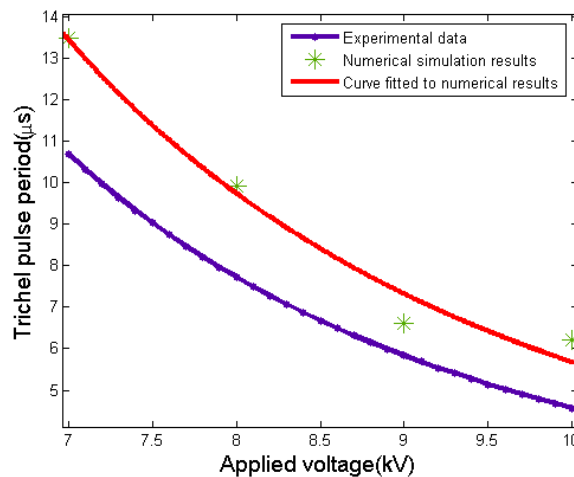


Figure 8.1: Trichel pulse period versus applied voltage - comparison of experimental and numerical results

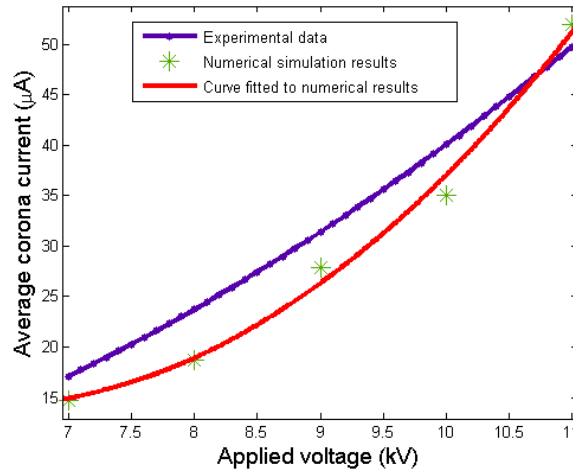


Figure 8.2: Average corona current versus applied voltage: experimental and numerical results

These Figures confirm that increasing the applied voltage decreases the Trichel pulse period (increases its frequency) and therefore increases the average corona current. The numerical simulation results are very compatible with the experimental data but they underestimate the pulse periods, especially at low voltages. This may be due to the difference in geometry (tip to plate spacing) and microscopic issues near the corona tip. For this reason, the simulation is repeated in the section 8.4 for the same configuration as used in the experiment.

8.3 Appearance and Physics of the Trichel Pulse

Near Needle Tip

In an attempt to understand some of the unusual Trichel pulse behaviour, Figure 8.3 shows some previously unpublished details of the experiments and observations as recorded by C.F. Gallo. In order to obtain a uniform series of Trichel pulses, needles of various sizes and shapes at different gap lengths were viewed with a microscope

under negative corona conditions and simultaneously all measurements were done with electrical meters and an oscilloscope. The voltage ranges started at the onset value (-2.3 kV) up to maximum of -7 kV for the larger gaps, with lower maximum voltages for smaller gaps. The data did not continue until sparking in order to avoid instrument damage. The visual appearance of the Trichel pulse corona is shown in Figure 8.3. At the negative needle tip, the existence of an extremely narrow bright ionization channel is conspicuous and unusual. Further from the needle tip, this channel abruptly expands into the usual corona cone configuration that then seems to follow the electric field lines into the gap. By contrast, for positive corona, this ionization channel is absent and the corona glow appears to follow the electric field lines from the needle tip and throughout the gap.

Because of this narrow ionization channel, the shape of the needle tip is critically important for obtaining stable and reproducible Trichel pulses. For a very sharp needle tip, the ionization channel wobbles around the tip erratically and the Trichel pulses are irregular and non-reproducible (an analogy of this instability would be a sharpened pencil standing on its sharp end.). Loeb, Trichel and others have called these “mode shifts” in some mysterious context [102]. These observed “mode shifts” are actually due to wobbles in the physical location of the ionization channel. To avoid this erratic behaviour, it was found that tips with slightly blunt or flattened ends yielded the most stable Trichel pulse behaviour. The ionization channel was securely located at the center of the slightly “blunt” needle tip as shown in Figure 8.3.

This narrow ionization channel is not described by present theory or simulations and may possibly be confined magnetically by the high current density. It is also probably responsible for the discrepancy between the measured low threshold

Table 8.1: Rough estimates of dimensions

Tip radii (r)	$3\mu m - 50\mu m$
Gap spacing (d)	$3mm - 16mm$
Blunted tip portion (BTP)	$0.6\mu m - 10\mu m$
Ionization channel diameter (D)	$0.12\mu m - 2\mu m$
Length of the ionization channel (L)	$1.2\mu m - 20\mu m$

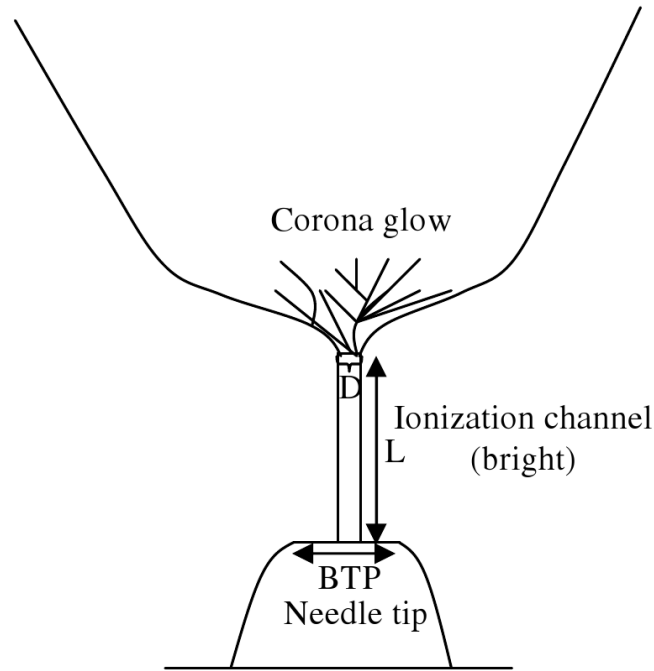


Figure 8.3: Experimental shape of the discharge region

voltages of -2.3 kV (approximately independent of tip radius) compared with calculated estimates of much higher -4.7 kV. Localized electron field emission may be involved in the unexpectedly low threshold voltage and its comparative insensitivity to tip radius. The physics of this narrow ionization channel as contrasted to the usual corona (which follows the expected electric field lines) is an interesting topic for future research.

8.4 Revised Comparison With Gallo's

Experimental Data

In this section, we revise the calculations and analysis presented in the previous section to obtain a better agreement with the Trichel pulse data of Lama and Gallo [26]. This has been done for several reasons:

1. From Figure 8.3 and Table 8.1, it is clear that there is an “effective tip radius” at the thin ionization channel that is much smaller than the actual radius of the needle tip.
2. The experimental fact that the threshold voltage is about -2.3 kV and is comparatively insensitive to tip radius provides a strong evidence that the usual electric field calculations for threshold voltage are not applicable, probably because localized microscopic electron field emission is operative in this case (Figure 8.3).
3. Although the functional trends for both the data and calculations are similar, as shown both in Figure 8.1 (Trichel pulse period) and Figure 8.2 (average corona current), the numerical values are quite different, which is consistent with the discussion above (items (1) and (2)).

Thus, the numerical calculations have been repeated assuming that the ionization channel is approximated by a needle with “effective tip radius” of 10 μm , which is more appropriate in view of the real microscopic situation displayed in Figure 8.3, and for the distance between the needle and plate of 6 mm. The applied voltage was set at -4 kV and the corona onset voltage for this configuration is assumed to be -2.3

Table 8.2: Trichel pulse characteristics for $V = -4kV$, $r = 10\mu m$, $d = 6mm$

$T_{average}^*$	$2.3\mu s$
Gallo's T	$2.0\mu s$
$I_{average}$	$12.1\mu A$
Gallo's $I_{average}$	$9.8\mu A$
St. D. of $T_{average}^*$	0.47

kV. According to the experimental results for this configuration the period of pulses should be $2\mu s$ and the average corona current is expected to be $9.8\mu A$.

The numerical simulation results are shown in Table 8.2. As this Table shows, the average Trichel pulse period is calculated as $2.3\mu s$ which is very close to experimental observations, and the average corona current is $12.1\mu A$. The agreement is very good as the value of calculated period agrees within the standard deviation, but both average values tend to overestimate the experimental observations by 15% and 23%, respectively. This may be due to the arbitrary nature of the approximation of the ionization zone (i.e. simplification of shape) and assumed value of tip radius.

8.5 Effect of Pressure on Trichel Pulse Characteristics

Most of the experimental and theoretical studies on corona discharge are performed at normal pressure (1 atm). Investigating the effect of pressure on the Trichel pulses is of interest and has not been widely discussed.

As reported in [26], for a given needle voltage the Trichel pulse frequency has an inverse relation with pressure. At higher pressures, there are a larger number of air molecules per cubic meter and this produces an inverse relation between mobility and

Table 8.3: Trichel pulse period and pulse duration versus gas pressure ($V=-9\text{kV}$,
 $R_{ext}=100\text{ k}\Omega$)

Air pressure (atm)	0.8	1	1.2
Trichel pulse period (μs)	4.88	6.61	11.07
Pulse duration (μs)	0.30	0.28	0.19

pressure since ions have more frequent collisions with neutral molecules. Therefore, in these gases the Trichel pulse period increases and the frequency decreases. On the other hand, experiments show that pulse duration also has an inverse relation with pressure [32] which is confirmed by our numerical results. Table 8.3 show the variation of Trichel pulse period and pulse duration versus gas pressure for values 80% and 120% of atmospheric.

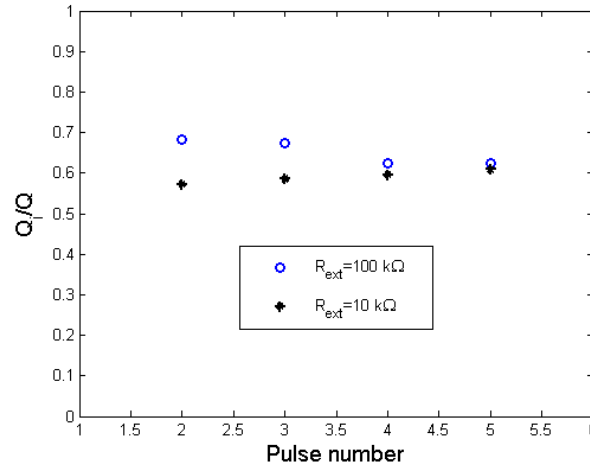
8.6 Comparison with Atten's Experimental Data

Comparing numerical results with the experimental data [32] results in the following conclusions:

1. The mean charge-per-pulse increases with corona electrode radius: as Table 8.4 shows, for the same applied voltage, reducing the radius of the corona electrode decreases the generated charge-per-pulse. This can be explained by the fact that increasing the radius of the corona electrode enlarges the region involved in the ionization. Therefore, the generated charge-per-pulse increases. As the Q_i increases, the Trichel pulse period decreases because larger space charge needs more time to travel through the gap. Therefore, it takes more time for the electric field to increase to a value at which a new Trichel pulse can be generated.

Table 8.4: Charge-per-pulse (in picocoulombs) for two configurations with different radii

Pulse number	2	3	4
Radius = 100 μm	115.61	114.17	111.49
Radius = 10 μm	23.781	21.906	21.415

Figure 8.4: Q_i/Q for $V = -9 \text{ kV}$

2. The ratio Q_i/Q (charge-per-pulse divided by the average charge-per-pulse) is always larger than 0.5. charge-per-pulse, Q_i , was calculated by integrating the corona current in time intervals at which the corona current is above 10% of the maximum current. In Atten's paper [32], it is reported that in high pressure air and with no external resistance, Q_i/Q is always smaller than 0.5. Since our numerical results were for normal pressure and for non-zero external resistances this observation was not confirmed but from Figure 8.4 it is obvious that decreasing the external resistance from 100 $\text{k}\Omega$ to 10 $\text{k}\Omega$ decreases this ratio significantly. Therefore, it is reasonable to extrapolate and expect that for zero external resistance, this ratio can be below 0.5 as reported in [32].

8.7 Conclusions

In this Chapter, the numerical results obtained from the numerical technique are compared with two previously reported sets of experimental data published by Gallo [26] and Atten et al. [32]. The results confirm that the frequency of the Trichel pulses increases as the applied voltage is increased which is compatible with previously reported experimental data. However, the numerical model overestimates the pulse periods at low voltages.

Moreover, Trichel pulses were obtained at different air pressures. The effect of pressure on Trichel pulse characteristics was investigated and it was confirmed that for a given needle voltage, the Trichel pulse frequency, the average corona current and the pulse duration are inversely proportional to pressure.

It has been shown that the mean charge-per-pulse has a direct relation with radius. Contrary to the experimental data presented in [32], the numerical simulation predicts the ratio Q_i/Q is larger than 0.5. It is suggested that this discrepancy is due to the presence of the external surge resistor.

Chapter 9

Modelling of Corona Discharge in Oxygen

9.1 Introduction

In the previous chapters, corona discharge was modelled in air. However, there is no standard definition for air composition and the content of the different gases of standard air are not exactly specified. On the other hand, pure oxygen is a well defined gas and the coefficients for modelling corona discharge in oxygen can be measured more precisely. Therefore, it is expected that a more accurate discharge model can be formulated for oxygen.

In this Chapter, first, the three existing databases in which the coefficients (electron mobility, diffusion coefficient, and ionization and attachment coefficients) are experimentally measured for oxygen are compared. Secondly, selected values of coefficients for solving the equations set from the two models used by Morrow [30] and Zhang and Adamiak [100] (based on Eliasson and Kogelschatz [23] experimental data), are presented and the compatibility of these coefficients with the measured values presented in available databases is investigated. Finally, a series of Trichel pulses in

oxygen is reproduced using Morrow's coefficients and the Trichel pulse characteristics in oxygen and air are compared.

9.2 Databases

According to the author's knowledge, there are three databases in which the coefficients needed for modelling corona discharge in oxygen are presented: Siglo [103], Morgan [104], and Phelps [105], all valid for a specific range of electric field. These experimentally measured values of coefficients are presented in Tables A.1-A.3 of Appendix A. The mobility of positive and negative oxygen ions are also extracted from [106] and are shown in Tables A.4-A.5 of Appendix A.

Figures 9.1-9.4 show comparison of the values of coefficients obtained from the three databases mentioned above. In all these Figures, EN represents the reduced electric field and is equal to $EN = \frac{E \times 10^{21}}{NO_2}$ where $NO_2 = 2.46 \times 10^{25} \times \frac{P}{P_0}$, P_0 is the standard pressure (1 atm or 760 Torr) and E stands for the magnitude of electric field.

As Figures 9.1-9.4 show, the coefficients of Siglo and Morgan databases are approximately the same. Therefore, only Phelps and Morgan databases are compared with the coefficients presented in the two available models.

9.3 Available Discharge Models

There are two available models in which mathematical formulations for the measured coefficients versus electric field are provided. These models are presented below.

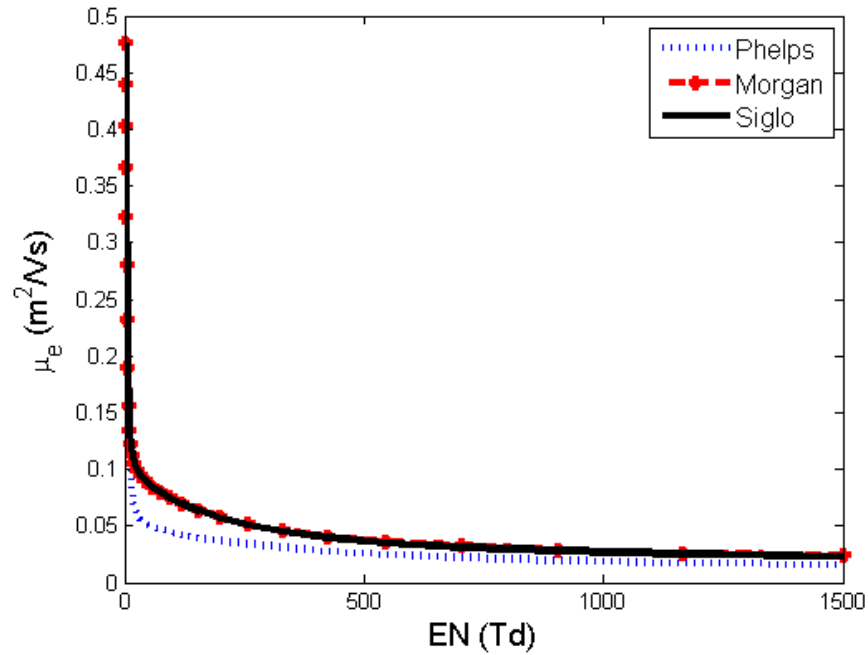


Figure 9.1: Mobility of electrons versus the reduced electric field

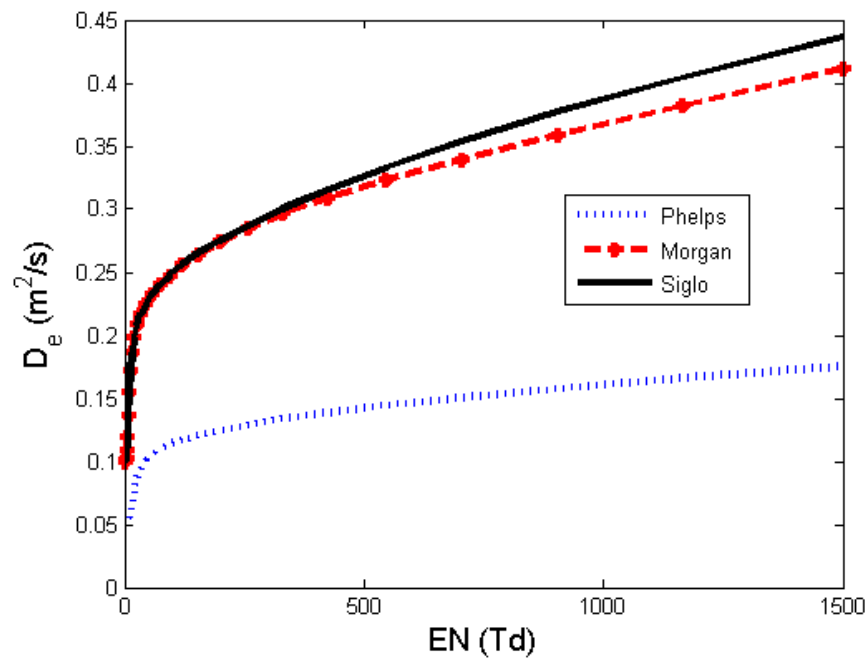


Figure 9.2: Diffusion coefficient versus the reduced electric field

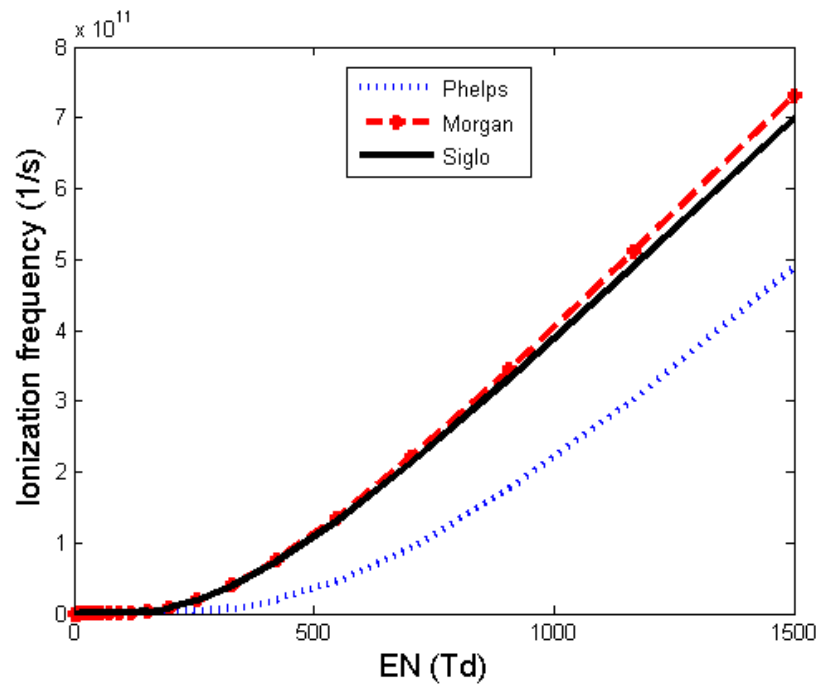


Figure 9.3: Ionization frequency versus the reduced electric field

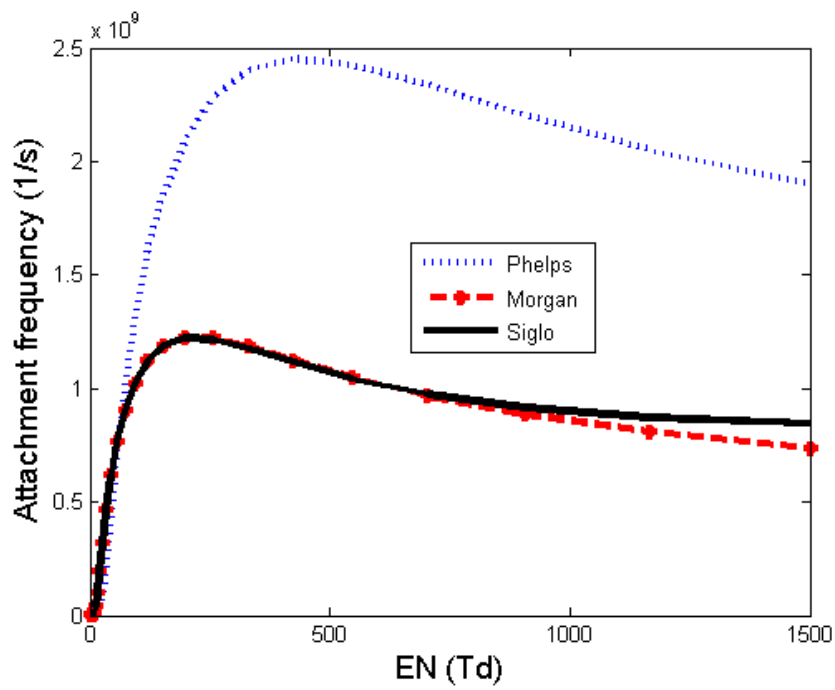


Figure 9.4: Attachment frequency versus the reduced electric field

9.3.1 Morrow's Model [30]

Morrow used the experimental values of the coefficients obtained by several researchers and presented them as functions of electric field.

This was 1D model defined by the following equations:

$$\begin{aligned}\frac{\partial N_e}{\partial t} &= N_e \alpha |W_e| - N_e \eta |W_e| - N_e N_p \beta - \frac{\partial(N_e W_e)}{\partial x} + \frac{\partial^2(D N_e)}{\partial x^2} \\ \frac{\partial N_p}{\partial t} &= N_e \alpha |W_e| - N_e N_p \beta - N_n N_p \beta - \frac{\partial(N_p W_p)}{\partial x} \\ \frac{\partial N_n}{\partial t} &= N_e \eta |W_e| - N_n N_p \beta - \frac{\partial(N_n W_n)}{\partial x}\end{aligned}$$

9.3.2 Eliasson et al. Model [23]

The coefficients of Table 9.2 are extracted from the functions used by Zhang and Adamiak [100] based on Eliasson et al. experimental data [23].

$$\begin{aligned}\frac{\partial N_e}{\partial t} + \nabla \cdot (N_e W_e) &= N_e \alpha |W_e| - N_e \eta |W_e| - \frac{N_e N_p \beta_{ep3}}{e_0} \\ \frac{\partial N_p}{\partial t} + \nabla \cdot (N_p W_p) &= N_e \alpha |W_e| - \frac{N_e N_p \beta_{ep3}}{e_0} - \frac{N_n N_p \beta_{np3}}{e_0} - \frac{N_n N_p \beta_{np2}}{e_0} \\ \frac{\partial N_n}{\partial t} + \nabla \cdot (N_n W_n) &= N_e \eta |W_e| - \frac{N_e N_p \beta_{np3}}{e_0} - \frac{N_n N_p \beta_{np2}}{e_0}\end{aligned}$$

β_{ep3} is the three-body recombination coefficient between electrons and positive ions, β_{np2} is the two-body recombination coefficient between negative and positive ions, and β_{np3} is the three-body recombination coefficient between negative and positive ions.

Figures 9.5-9.8 compare the coefficients of these two models with those of Phelps and Morgan databases. They show that the electron mobility and the diffusion and the ionization coefficients of Morrow's model are compatible with the Phelps and

Table 9.1: Morrow's model coefficients [30]

Parameters	Morrow
v_i (1/s)	$\alpha_e \times E \times NO_2 \times (2.124 \times 10^{-20}) \exp(-621.16/EN)$
v_a (1/s)	$\beta_1 + \beta_2$
β_1 (1/s)	If (EN < 18.35) $\alpha_e \times E \times NO_2 \times (5.032 \times 10^{30}) \left(\frac{E}{NO_2}\right)^{2.655}$ else $\alpha_e \times E \times NO_2 (2 \times 10^{-22})$
β_2 (1/s)	$\frac{3 \times 10^{-42} \times NO_2^2}{1 + \left(\frac{EN}{4}\right)^{1.5}}$
μ_e (m ² /Vs)	$\frac{(5.747 \times 10^{16})}{E} \left(\frac{E}{NO_2}\right)^{0.6064}$
μ_p (m ² /Vs)	$\frac{5.5 \times 10^{21}}{NO_2}$
μ_n (m ² /Vs)	$\frac{5.5 \times 10^{21}}{NO_2}$
D (m ² /s)	if (EN ≤ 2) $D_e = \alpha_e \times (1.343 \times 10^6) \left(\frac{E}{NO_2}\right)^{0.3441}$ if (EN > 2 & EN ≤ 12.3) $D_e = \alpha_e \times (1.213 \times 10^{25}) \times \left(\frac{E}{NO_2}\right)^{1.2601}$ if (EN > 12.3) $D_e = \alpha_e \times (1.519 \times 10^9) \times \left(\frac{E}{NO_2}\right)^{0.46113}$
β_{ep} (m ³ /s)	2×10^{-13}
β_{np} (m ³ /s)	2×10^{-13}

Table 9.2: Eliasson et al. model coefficients based on Zhang et al. [100]

Parameters	Zhang and Adamiak
v_i (1/s)	if ($EN < 218.0$) $v_i = NO_2 \times 10^4$ else $v_i = NO_2 \times (-1.40909 \times 10^{-16} + 2.20315 \times 10^{-18} EN + 7.39257 \times 10^{-21} EN^2)$ $A_1 = -13.5 - \left(\frac{414}{EN}\right) + \left(\frac{10400}{EN^2}\right) - \left(\frac{148000}{EN^3}\right)$
v_a (1/s)	$v_a = ka_3 \times NO_2^2$ $ka_3 = 1.21 \times 10^{-42} \frac{\exp\left(\frac{-0.0939}{\delta}\right)}{\delta}$ if ($EN \leq 75.2$) $\delta = 1.5 \times 10^B$ else $\delta = 1.5 \times 10^C$ $B = -0.827 + (1.25X) - (4.08X^2) + (9.07X^3) - (8.06X^4) + (3.14X^5) - (0.451X^6)$ $C = -0.221 + (0.379X)$ $X = \log(EN)$
μ_e (m^2/Vs)	$\frac{1}{NO_2} 10^{25.06 - 0.502X + 0.0354X^2}$
μ_p (m^2/Vs)	2×10^{-4}
μ_n (m^2/Vs)	2×10^{-4}
D (m^2/s)	0.0
β_{ep3} (m^3/s)	2.46×10^{-13}
β_{np2} (m^3/s)	4.2×10^{-13}
β_{np3} (m^3/s)	4.92×10^{-12}

Morgan's reported data. The attachment coefficient is much more problematic since Morrow has only considered two body and three body attachment reactions. However, his assumed value for attachment coefficient is used in this Chapter for modelling purposes.

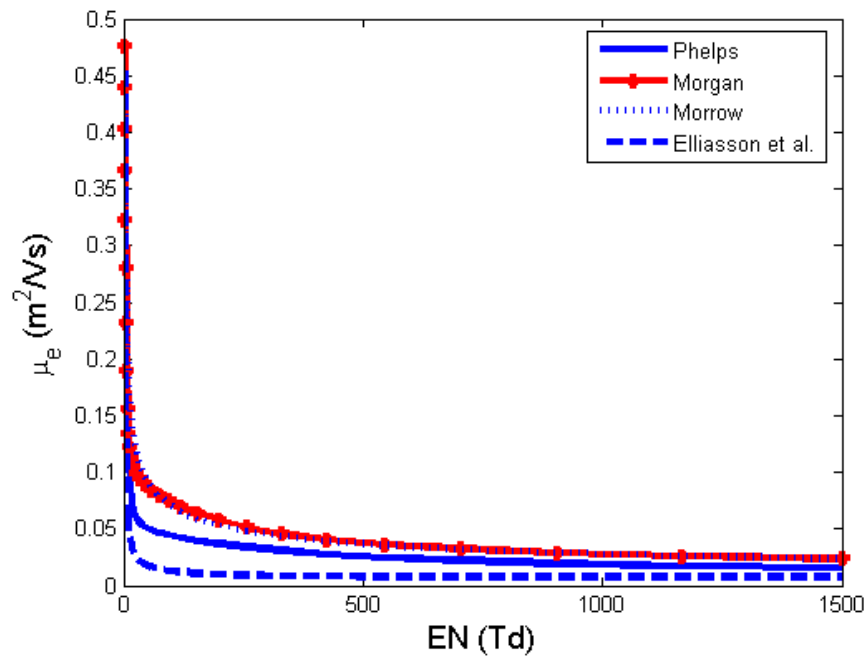


Figure 9.5: Mobility of electrons versus the reduced electric field

9.4 Results

For modelling corona discharge in oxygen, Morrow's set of coefficients were used in the 2D numerical solver presented in Chapter 4. The only difference between the author's and Morrow's coefficients is in the diffusion coefficient. Since using Morrow's diffusion coefficient it was not possible to obtain convergent results, the same diffusion

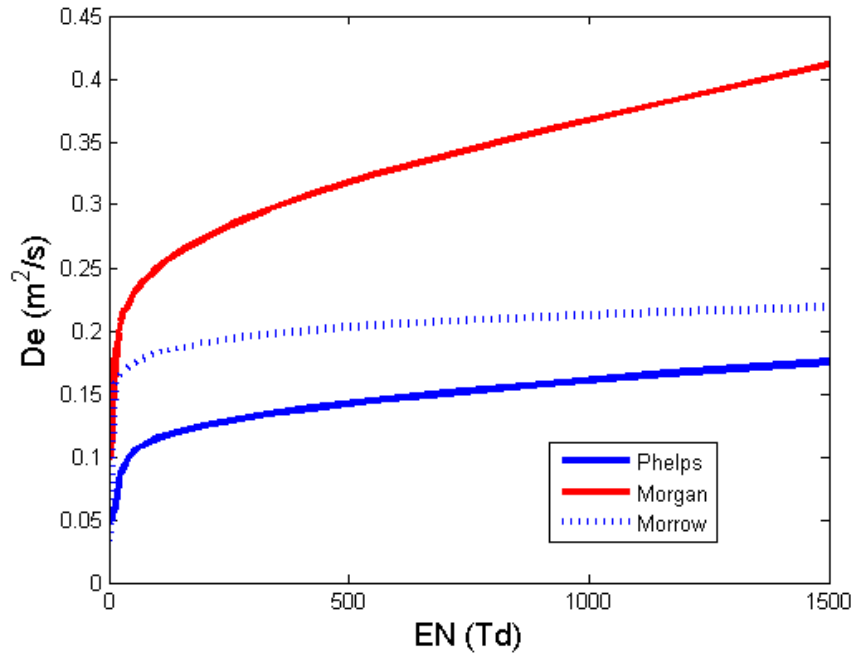


Figure 9.6: Diffusion coefficient versus the reduced electric field

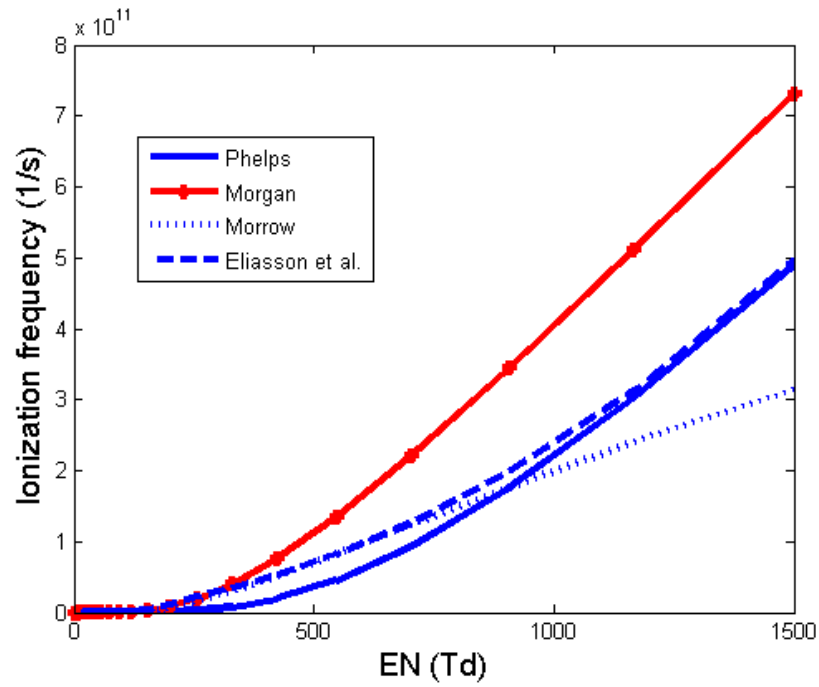


Figure 9.7: Ionization coefficient versus the reduced electric field

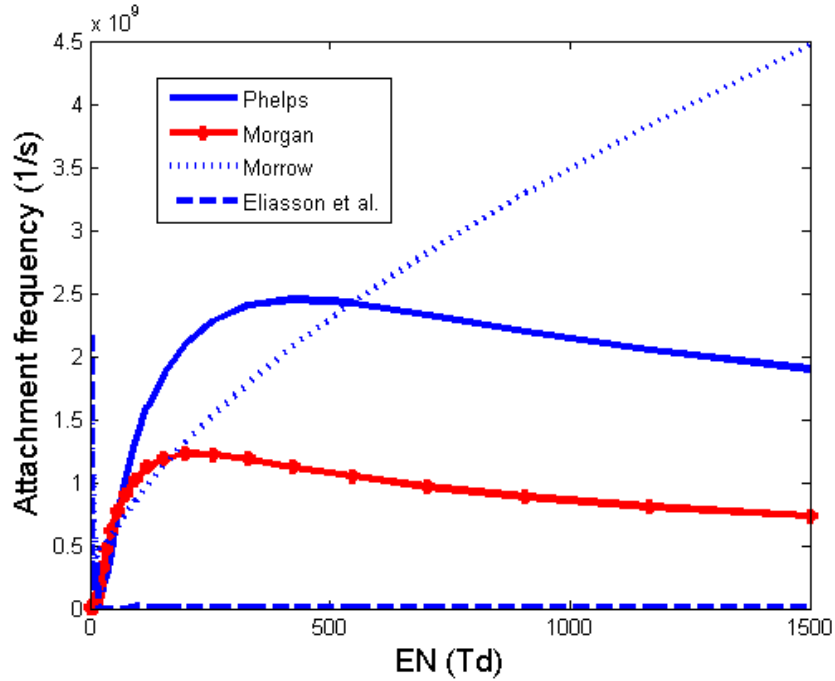


Figure 9.8: Attachment coefficient versus the reduced electric field

coefficient as in the air model, $D = 1.263 \times 10^{-3}$ was used instead. This coefficient is smaller than Morrow's suggested value (Figure 9.6).

Figures 9.9 and 9.10 show a series of Trichel pulses for the applied voltage of -7kV in oxygen and air respectively. Figures 9.11, 9.13 and 9.15 show the total density of electrons, positive ion and negative ions in the air gap versus time for oxygen; Figures 9.12, 9.14 and 9.16 shows the same densities in air. Figure 9.17 shows the electric field versus time for oxygen and Figure 9.18 shows the electric field versus time for air.

Comparing the results in air and oxygen, it can be observed that in oxygen:

1. the average period of pulses is shorter than in air: $8.3 \mu s$ versus $13.47 \mu s$.

2. frequency of pulses is more regular in oxygen, (without taking the first pulse into our calculations) $STD_{oxygen} = 1.21$ and $STD_{air} = 3.26$.
3. the amplitude of pulses is smaller because the total number of electrons and positive ions created during each pulse (due to ionization) are smaller.
4. total number of electrons and positive ions generated during each pulse is smaller, because the ionization coefficient of oxygen model is smaller than that of air model for the same value of electric field.
5. total number of negative ions decreases in a small time span after the first pulse only and after that time, it always increases because of the attachment coefficient which is much larger than the attachment coefficient assumed in air.
6. electric field increases much faster after each pulse because the created number of positive ions is smaller and these ions reduce the electric field of the corona electrode much less.

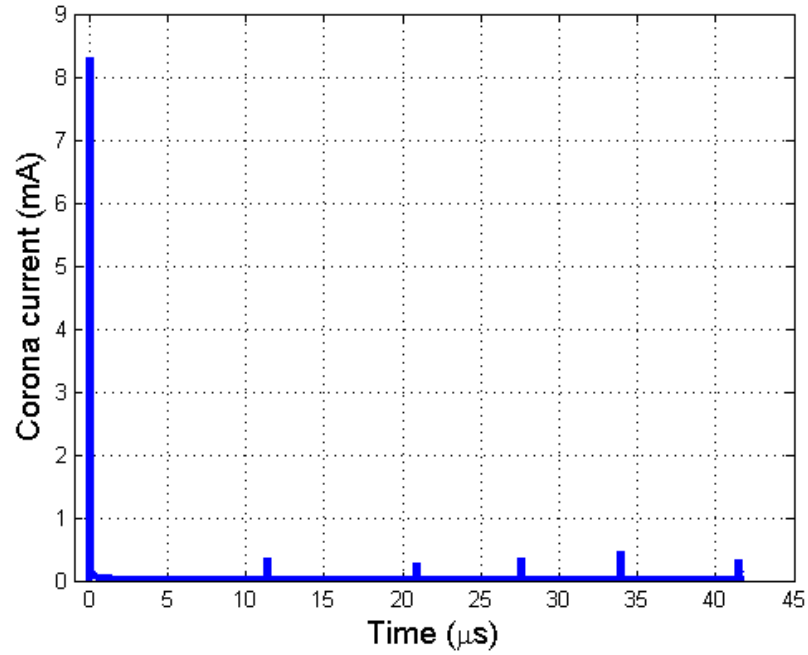


Figure 9.9: Corona current versus time in oxygen

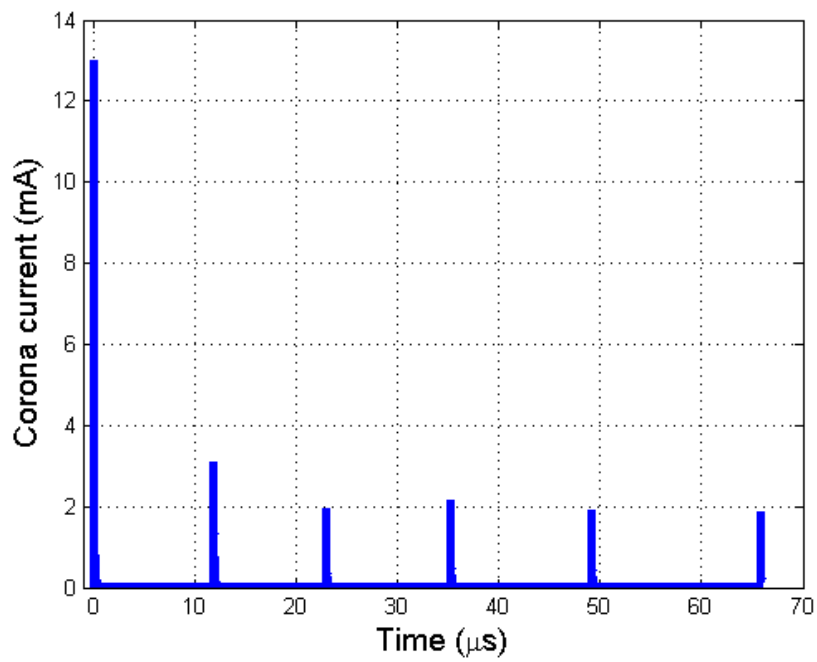


Figure 9.10: Corona current versus time in air

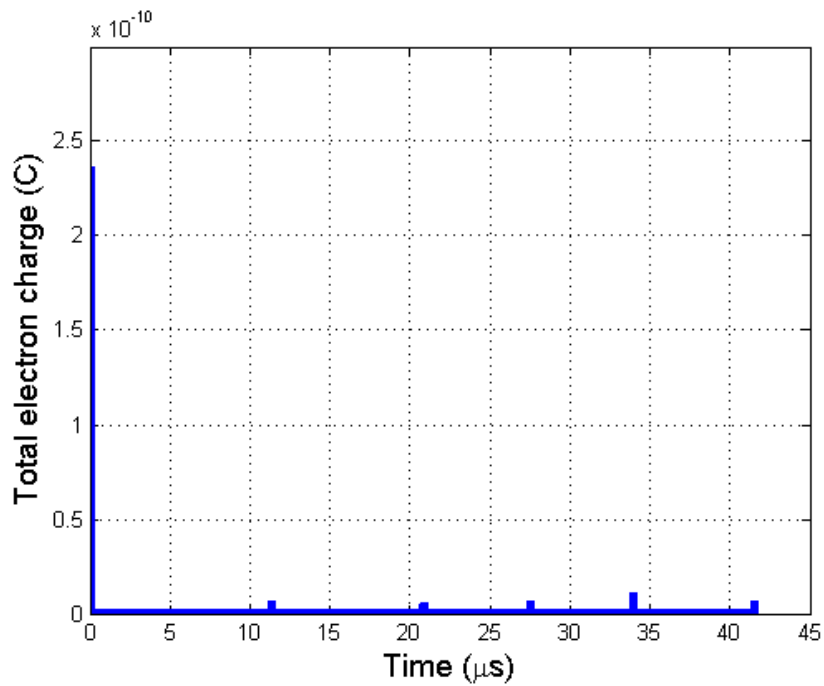


Figure 9.11: Total charge of electrons versus time in oxygen

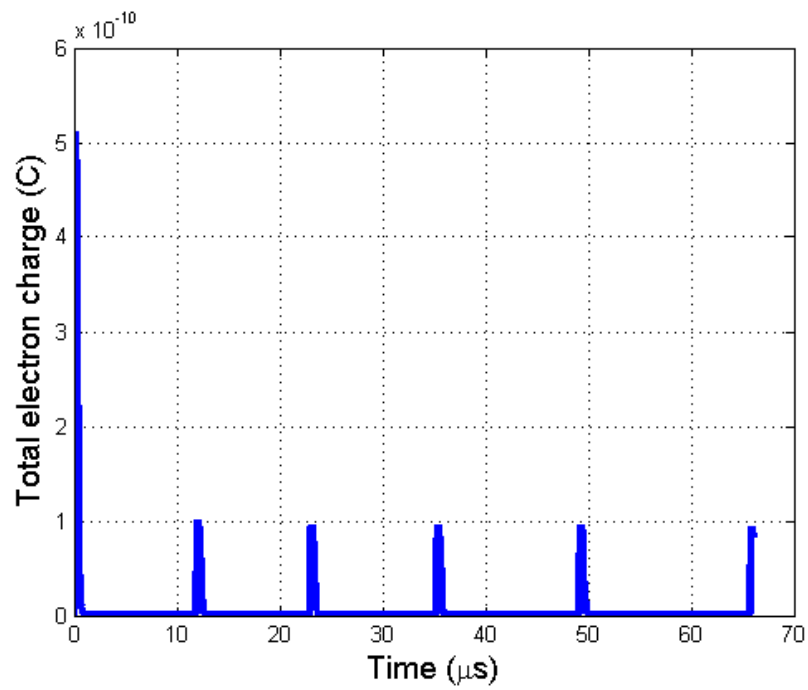


Figure 9.12: Total charge of electrons versus time in air

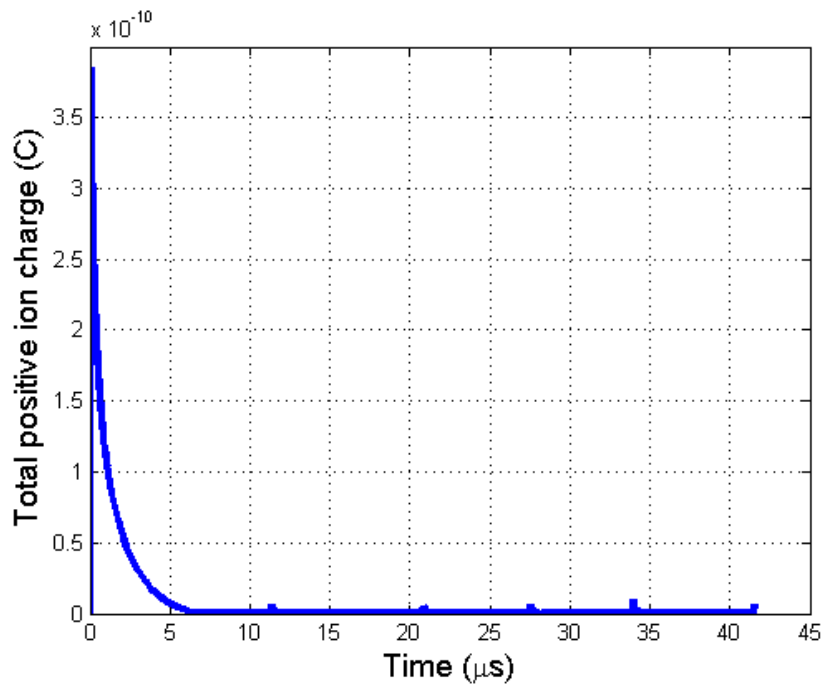


Figure 9.13: Total charge of positive ions versus time in oxygen

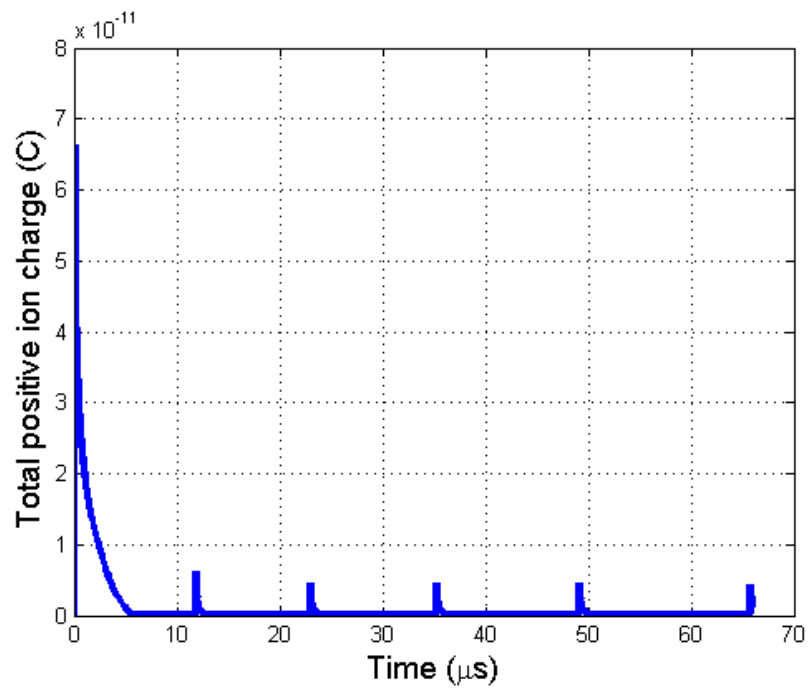


Figure 9.14: Total charge of positive ions versus time in air

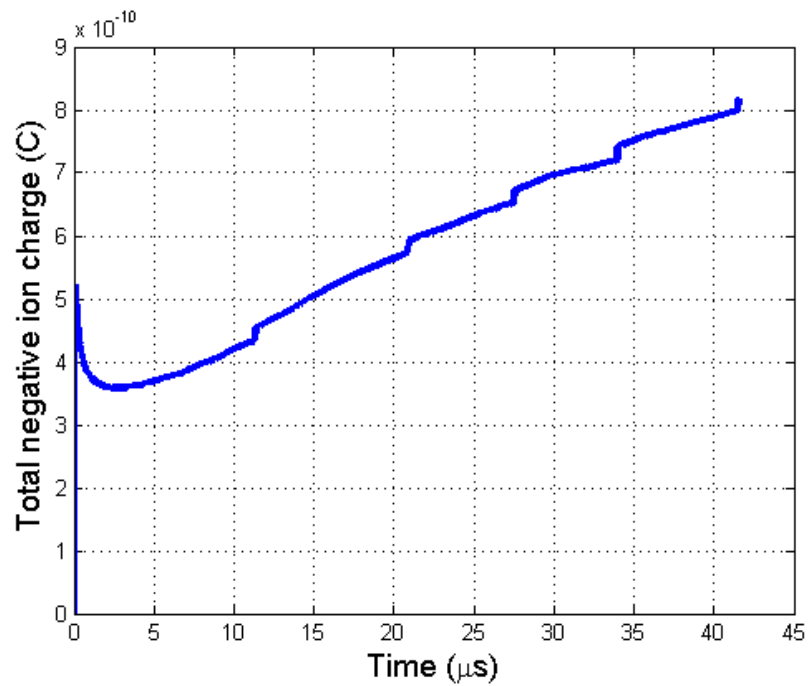


Figure 9.15: Total charge of negative ions versus time in oxygen

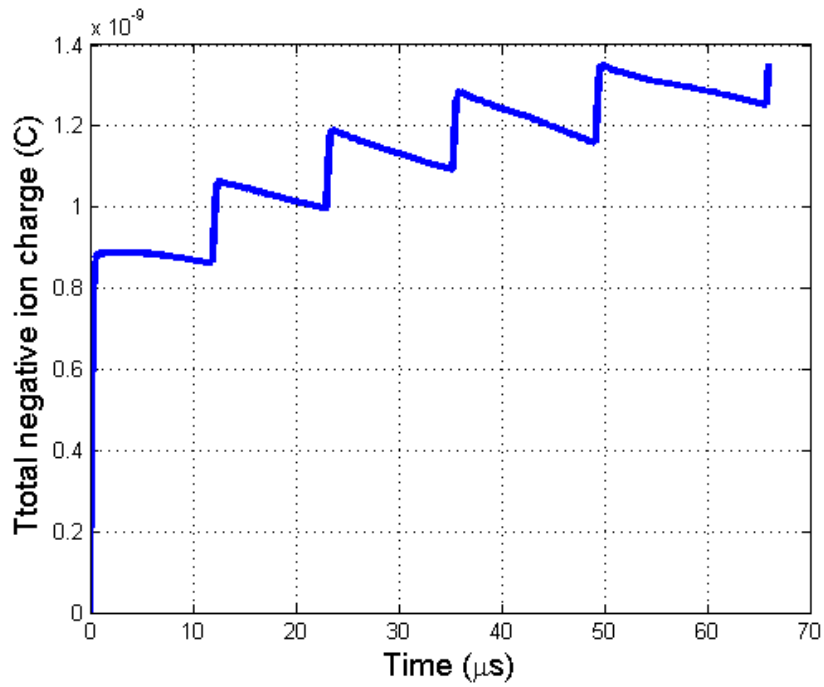


Figure 9.16: Total charge of negative ions versus time in air

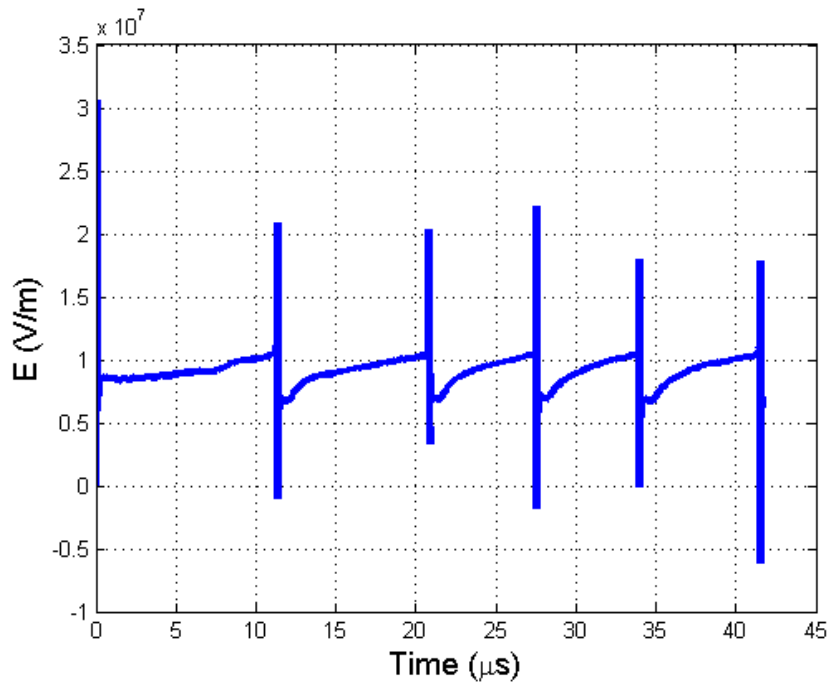


Figure 9.17: Electric field versus time in oxygen

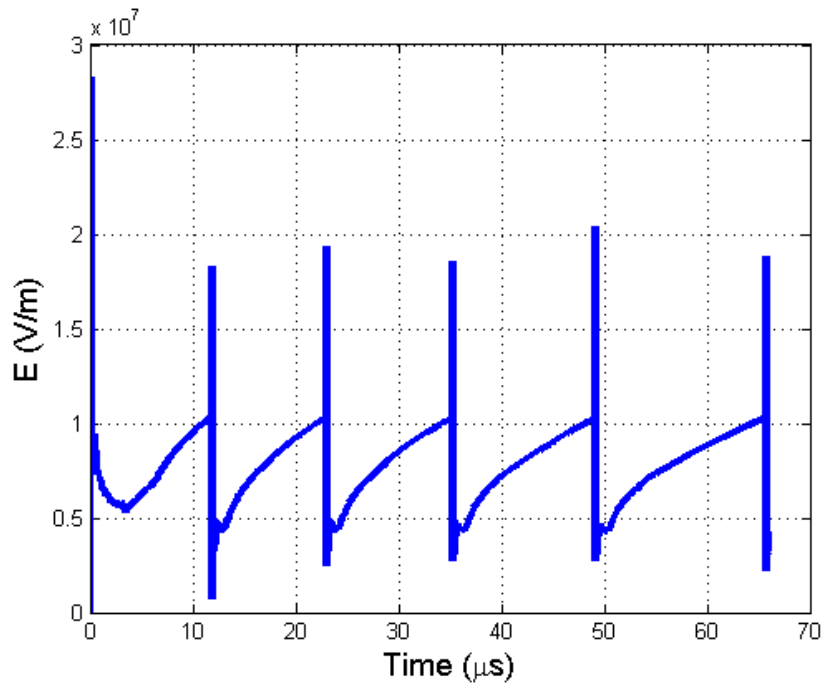


Figure 9.18: Electric field versus time in air

Chapter 10

Summary, Conclusions and Recommendations for Future Study

10.1 Summary

In this thesis, Trichel pulse regime of negative corona discharge in oxygen and air was simulated under dynamic conditions. A FEM based technique was developed for solving the Poisson equation to calculate the electric field and potential distribution. To solve the charge continuity equations, a FEM-FCT based algorithm was proposed. Different steps of the FCT algorithm: high-order solution (based on the Galerkin FEM), low-order solution (upwinding) and limiting were mathematically explained and formulated. The technical problems occurring during the programming were also explained and the solutions to these problems were presented. Several optimization techniques were also proposed for reducing the run time of the code.

10.1.1 Dynamic Single-Species Model of Corona Discharge

In this section, a single species model was used for modelling negative corona discharge. In this model, the ionization layer was completely disregarded. The be-

haviour of the total corona current and space charge density under two waveforms of the applied voltage, step and pulse, was studied. Kaptzov's hypothesis was used as a supplementary boundary condition for calculating the charge density on the surface of the corona electrode.

For the step voltage, the effect of the input voltage and the external resistance on the average corona current was studied.

For the pulse voltage, the effect of the frequency of the applied voltage on the average current was investigated. Moreover, the time evolution of the space charge density was shown. The shapes of charge clouds at different time instants and for different applied voltages were presented.

10.1.2 Simulation of Trichel Pulse in Air

The model used for this simulation included three ionic species: electrons, negative and positive oxygen ions. Three main ionic reactions were considered: electron avalanche ionization, attachment of electrons to neutral molecules and the recombination between electrons and positive ions.

The Trichel pulse regime of negative corona discharge in air was simulated. A series of Trichel pulses for different applied voltages were successfully shown. In addition, the distributions of electron, ion densities and electric field during the different stages of one Trichel pulse were presented.

10.1.3 Parametric Study of Trichel Pulse Characteristics

Effect of different parameters (i.e. external resistance, secondary electron emission coefficient, negative and positive ion mobilities) on the Trichel pulse characteristics was investigated.

The 2D ionization layer profiles in the air gap during one Trichel pulse were shown and the ionization layer thickness along the axis versus time was presented.

10.1.4 Experimental Verification of the Numerical Results

The numerical results were compared with the experimental data reported by Lama and Gallo [26] for a specific configuration of electrodes (needle radius and gap distance). Moreover, the effect of pressure on Trichel pulse characteristics was studied and compared with the existing experimental data presented by Atten et al. [32]. The effect of tip radius on the charge per pulse was also investigated. The relation between charge per pulse and the average charge per pulse was discussed and compared with the available experimental data.

10.1.5 Trichel Pulse Simulation in Oxygen

In this section, the three existing databases and the two available models for modelling negative corona discharge in oxygen were presented and compared. A series of Trichel pulses in oxygen was reproduced and the Trichel pulse characteristics in oxygen and air were compared.

10.2 Conclusions

The following conclusions can be formulated from the results obtained from numerical analysis:

Single-species model:

When a step voltage is applied to the corona electrode:

- The total corona current has large values at $t=0$ but it decreases quickly to a constant value at steady state.
- Larger input voltage results in a larger current in the circuit.
- The value of current is larger for smaller external resistance.

When a periodic pulse voltage is applied to the corona electrode:

- The resulting current will be periodic too.
- The average current depends on the frequency and increases as the frequency of pulses increase. The peak value of these sequential current pulses decreases.
- The current increases quickly to a peak value and then decreases to a small DC value when the applied voltage is below the corona onset voltage.
- The charge clouds are formed in the air gap and move towards the ground plate. The velocity of these charge pulses depends on the electric field. Therefore, as they move, their velocity decreases due to the decrease in the electric field.
- If the frequency of the applied pulse voltage is too high, charge pulses will eventually combine.

Three-species simulation in air:

- The model has successfully reproduced a series of Trichel pulses for different applied voltages and the pulse formation is explained by showing the densities of electrons, ions, and the electric field distributions along the axis of symmetry.
- The results confirm that the frequency of the Trichel pulses increases as the applied voltage is increased.
- The numerical results obtained from this technique are compatible with previously reported experimental data available for Trichel pulse period versus voltage but they underestimate the pulse period at low voltages.
- The effects of different parameters of the corona discharge model on Trichel pulse characteristics (Trichel pulse period and the average corona current) were studied. From the numerical simulation results, it was observed that:
 - As the external resistance decreases, period of pulses increases.
 - As the external resistance decreases, average corona current decreases.
 - As the mobility of ions increases, the period of pulse decreases and, therefore, average corona current increases.
 - Secondary electron emission coefficient does not seem to have any significant effect on Trichel pulse characteristics.
 - The numerical and experimental data obtained for Trichel pulse characteristics for the same configuration agree relatively well.
- The effect of pressure on Trichel pulse characteristics was studied. It was observed that:

- For a given needle voltage, the Trichel pulse frequency, the average corona current and the pulse duration are inversely proportional to pressure.
- It has been shown that the mean charge per pulse has a direct relation with radius.
- Contrary to the experimental data, the numerical simulation predicts that the ratio Q_i/Q is larger than 0.5. It was suggested that this discrepancy is due to the presence of the external surge resistor.

Three-species simulation in oxygen:

Subsequent results are obtained by comparing Trichel pulse characteristics in oxygen with the following observations:

- The average period of pulses in oxygen is shorter than in air.
- Pulses are more regular.
- The amplitude of pulses is smaller.
- Total number of electrons and positive ions generated during each pulse is smaller.
- Total number of negative ions decreases in a small time span after the first pulse only and after that time, it always increases.
- Electric field increases much faster after each pulse.

10.3 Recommendations for Future Study

1. To improve the accuracy of the model, the effect of photoionization can be included. Afterwards, the possibility of the complete model for modelling glow

regime of corona discharge can be investigated, as the glow regime of corona discharge could not be modelled with the existing model.

2. More ionic species and reactions can be included in the model and the possibility of getting more accurate results with the inclusive model can be investigated.
3. The program can be optimized further to reduce the run time of the code by introducing parallel programming.
4. The possibility of modelling the pulses in other gases (electronegative and electropositive) can be investigated. It should be tested whether Trichel pulse regime exists in electropositive gases (e.g., Nitrogen) as some researchers reported.
5. Positive corona discharge can be modelled with this numerical technique.
6. The possibility of using this algorithm for the optimization purpose in industrial devices, such as ionizers and powder coating systems can be investigated.
7. Magnetic field can also be included in the equations to verify its effect on discharge characteristics.
8. The electromagnetic field produced by Trichel pulses can be calculated to investigate electromagnetic interference caused by corona discharge.

References

- [1] V. Repan, "Low current mode of negative corona," Ph.D. dissertation, Dept. Phys., Tartu Univ., Estonia, 2004.
- [2] L. M. Dumitran, L. Dascalescu, P. V. Notingher, and P. Atten, "Modelling of corona discharge in cylinder-wire-plate electrode configuration," *J. of Electrostatics*, vol. 65. pp. 758-763, 2007.
- [3] M. Goldman and A. Goldman, *Gaseous Electronics*, M.N. Hirsh and H.J. Oskam, Eds., vol. I, New York: Academic Press, 1978, pp. 219-290.
- [4] R. S. Sigmond, *Electrical Breakdown of Gases*, J. M. Meek and J. D. Craggs, Eds., New York: Wiley, 1978, p. 369.
- [5] M. Goldman and R. S. Sigmond, "Corona and insulation," *IEEE Trans. Electr. Insul.*, vol. 17, iss. 2, pp. 90-105, 1982.
- [6] F. W. Peek, *Dielectric Phenomena In High Voltage Engineering*, New York: McGraw hill, May 2006.
- [7] G. Noll Charles, "Ozone production by corona discharges," *J. of the IEST*, vol. 45, no. 1, 2002.
- [8] B. Khaddour, P. Atten, and J. L. Coulomb, "Numerical solution and experimental test for corona discharge between blade and plate," *IEEE Trans. Mag.*, vol. 43, no. 4, April 2007.

-
- [9] H. J. White, "Centenary of Frederick Gardner Cottrell," *J. of Electrostat.* vol. 4, pp. 1-34, 1977-78.
- [10] J. S. Chang, P. A. Lawless, and O. Yamamoto, "Corona discharge process," *IEEE Trans. Plasma Sci.*, vol. 19, no. 6, Dec. 1991.
- [11] M. Woong-Gee, L. Seok-Hyun, K. Hyoeng-Seok, and H. Song-Yop, "Transient approach to steady state of discharge phenomena in corona device," *IEEE Trans. Mag.*, vol. 38, no. 2, March 2002.
- [12] C. Junhong and J. H. Davidson, "Model of the negative DC corona plasma: comparison to the positive DC corona plasma," *Plasma chemistry and plasma processing*, vol. 23, no. 1, March 2003.
- [13] E. M. Veldhuizen, *Electrical Discharges for Environmental Purposes, Fundamentals and Applications*, New York: Nova Scotia Publishers, Inc., 2000.
- [14] K. H. Becker, U. Kogelschatz, K. H. Schoenbach and R. J. Barker., Eds. *Non-Equilibrium Air Plasmas at Atmospheric Pressure*. London: Institute of Physics, 2005, pp. 41-68.
- [15] W. Hermstein, "Positive Glow Corona," *Archiv. Elektrotech.*, vol. 45, pp. 209-224, 1960.
- [16] G. W. Trichel, "The mechanism of the positive point-to-plane corona in air at atmospheric pressure," *Phys. Rev.*, vol. 55, iss. 4, pp. 382-390, 1938.
- [17] L. R. Grabowski, "Pulsed corona in air for water treatment," Ph.D. Thesis, Eindhoven University of Technology, The Netherlands, 2006.
- [18] L. Dascalescu, *An Introduction to Ionized Gases: Theory and Applications*, Toyohashi, Japan: TUT Press, 1993.

- [19] Y. S. Akishev, M. E. Grushin, V. B. Karal'nik, and N. I. Trushkin, "Pulsed mode of a negative corona in nitrogen: I. experiment," *Plasma Phys. Reports*, vol. 27, no. 6, pp. 520-531, 2001.
- [20] Y. S. Akishev, M. E. Grushin, V. B. Karal'nik, and N. I. Trushkin, "Pulsed mode of a negative corona in nitrogen: II. numerical calculations," *Plasma Phys. Reports*, vol. 27, no. 6, pp. 532-541, 2001.
- [21] L. B. Loeb, *Fundamental Processes of Electrical Discharge in Gases*, New York: Wiley, 1947.
- [22] F. Pontiga, C. Soria, and A. Castellanos, "Spatial distribution of electrons and ions in a negative corona discharge," *Conference on Electrical Insulation and Dielectric Phenomena*, San Francisco, October 20-23, 1996.
- [23] B. Eliasson and U. Kogelschatz, "Basic Data for Modelling of Electrical Discharges in Gases: Oxygen," *Bown Boveri Technical Report*, 1986 (unpublished).
- [24] R. Zentner, "Ober die anstiegszeiten der negativen korona entladungsimpulse," *Angew. Math Phys.*, vol. 29, pp. 294-301, 1970.
- [25] C. Soria, F. Pontiga, and A. Castellanos, "Particle-in-cell simulation of Trichel pulses in pure oxygen," *J. of Phys. D: Applied Physics*, vol. 40, no. 15, pp. 4552-4560, August 2007.
- [26] W. L. Lama and C. F. Gallo, "Systematic study of the electrical characteristics of the Trichel current pulses from negative needle-to-plane coronas," *J. Appl. Phys.*, vol. 45, iss. 1, p. 103, 1974.
- [27] L. B. Loeb, A. F. Kip, and G. G. Hudson, "Pulses in negative point-to-plane corona," *Phys. Rev.*, A 60, pp. 714-722, 1941.

- [28] G. N. Aleksandrov, "On the nature of current pulses of a negative corona," *Sov. Phys. Tech. Phys.*, vol. 8, no. 2, pp. 161-166, 1963.
- [29] M. M. Kekez, P. Savic and G. D. Lougheed, "A novel treatment of Trichel-type phenomena with possible application to stepped-leader," *J. Phys. D: Appl. Phys.*, vol. 15, pp. 1963-73, 1982.
- [30] R. Morrow, "Theory of negative corona in oxygen," *Phys. Rev.*, A 32, pp. 1799-1809, 1985.
- [31] R. Morrow. "Theory of stepped pulses in negative corona discharges," *Phys. Rev.*, A 32, pp. 3821-3824, 1985.
- [32] M. Haidara, A. Denat and P. Atten, "Corona discharges in high pressure air," *J. Electrostatics*, , vol. 40-41, pp. 61-66, 1997.
- [33] C. Soria, F. Pontiga and A. Castellanos, "Particle-in-cell simulation of Trichel pulses in pure oxygen", *J.Phys. D: Appl. Phys.*, vol. 40, no. 15, pp. 4552-4560, August 2007.
- [34] A. P. Napartovich, Yu. S. Akishev, A. A. Deryugin, I. V. Kochetov, M. V. Pan'kin, and N. I. Trushkin, "A numerical simulation of Trichel-pulse formation in a negative corona," *J. Phys. D: Appl. Phys.*, vol. 30, pp. 2726-2736, 1997.
- [35] Yu. S. Akishev, I. V. Kochetov, A. I. Loboiko, and A. P. Napartovich, "Numerical simulation of Trichel pulses in a negative corona in air," *Plasma Phys. Reports.*, vol. 28, no. 12, 2002, pp. 1049-1059.
- [36] J. M. K. MacAlpine and W. C. Yim, "Computer modelling of Trichel pulses in air," *Conf. on Electrical insulation and Dielectric Phenomena*, pp. 118-21, 1995.

- [37] P. A. Va'zqueza, A. T. Pe'rez, A. Castellanos, and P. Atten, "Dynamic of electrohydrodynamic laminar plumes: scaling analysis and integral model," *Phys. Fluids*, vol. 12, no. 11, pp. 2809-2818, 2000.
- [38] T. N. Tran, I. O. Golosnov, P. L. Levin and G. E. Georghiou, "Two dimensional studies of Trichel pulses in air using the finite element method," *IEEE Conference on Electrical Insulation and Dielectric Phenomena*, CEIDP '09 , pp. 592-595, Oct. 18-21 2009.
- [39] J. R. McDonald, W. B. Smith, H. W. Spencer, and L. E. Sparks, "A mathematical model for calculating electrical conditions in wire-duct electrostatic precipitation devices," *J. Appl. Phys.*, vol. 48, pp. 2231-2243, 1977.
- [40] J. L. Davis and J. F. Hoburg, "Wire-duct precipitator field and charge computation using finite element and characteristics method," *J. Electrostatics*, vol. 14, pp. 187-199, 1983.
- [41] A. J. Butler, Z. J. Cendes, and J. F. Hoburg, "Interfacing the finite element method with the method of characteristics in self-consistent electrostatic field models," *IEEE Trans. Ind. Appl.*, vol. 25, pp. 533-538, 1989.
- [42] G. Ghione and R. D. Graglia, "Two-dimensional finite-boxes analysis of monopolar corona fields including ion diffusion," *IEEE Trans. Magn.*, vol. 26, pp. 567-570, 1990.
- [43] P. L. Levin and J. F. Hoburg, "Donor cell-finite element descriptions of wire-duct precipitator fields, charges, and efficiencies," *IEEE Trans. Ind. Appl.*, vol. 26, no. 4, pp. 662-670, 1990.

-
- [44] H. Singer, H. Steinbigler, and P. Weiss, "A charge simulation method for the calculation of high voltage fields," *IEEE Trans. Power Appar. and Sys.*, vol. 93, no. 5, pp. 1660-1668, 1974.
- [45] M. H. Horenstein, "Computation of corona space charge, electric field, and V-I characteristic using equipotential charge shells," *IEEE Trans. Ind. Appl.*, vol. 20, no. 6, pp. 1607-1612, 1984.
- [46] A. A. Elmoursi and G. S. P. Castle, "Modelling of corona characteristics in a wire-duct precipitator using the charge simulation technique," *IEEE Trans. Ind. Appl.*, vol. 23, no. 1, pp. 95-102, 1987.
- [47] N. H. Malik, "A review of the charge simulation method and its applications," *IEEE Trans. Dielect. and Electr. Insul.*, vol. 24, no. 1, pp. 3-20, 1989.
- [48] A. A. Elmoursi and C. E. Speck, "Simulation of space charge in unbounded geometries," *IEEE Trans. Ind. Appl.*, vol. 26, no. 2, pp. 384-392, 1990.
- [49] K. Adamiak, "Simulation of corona in wire-duct electrostatic precipitator by means of the boundary element method," *IEEE Trans. Ind. Appl.*, vol. 30, no. 2, pp. 381-386, 1994.
- [50] H. Yamashita, K. Shinozaki and E. Nakamae, "A boundary-finite element method to compute directly electric field intensity with high accuracy," *IEEE Trans. Power Deliv.*, vol. 3, no. 4, pp. 1754-1760, 1988.
- [51] S. S. Bamji, A. T. Bulinshi, and K. M. Prasad, "Electric field calculations with the boundary element method," *IEEE Trans. Dielect. and Electr. Insul.*, vol. 28, no. 3, pp. 420-424, 1993.

-
- [52] M. D. Driga and A. Wu, "Coupled transient finite element and boundary element method modelling of nonlinear, nonhomogeneous, electric field devices with mesh refinement," *IEEE 1997 Annual Report of Conference on Electr. Insul. and Diel. Phenomena*, Mineapolis, MN, USA, vol. 2, pp. 485-489, 1997.
- [53] K. Adamiak and P. Atten, "Simulation of corona discharge in point-plane configuration," *J. of Electrostatics*, vol. 61, iss. 2, pp. 85-98, 2004.
- [54] J. Zhang, K. Adamiak, and G. S. P. Castle, "Negative corona discharge in point-plane geometry: two species model in oxygen," *In Gaseous Dielectrics*, L.G. Christophorou, J.K. Olthoff and P. Vassiliou, Eds., New York: Springer, pp. 149-154, 2004.
- [55] P. L. Levin and J. F. Hoburg, "Donor cell-finite elements discreptions of wire-duct precipitator fields, charges and efficiencies," *IEEE Trans. Ind. Appl.*, vol. 26, pp. 662-670, 1990.
- [56] P. L. Levin, "Comparison of the donor cell method to other computational techniques for the duct electrostatic precipitator," *J. of Electrostat.*, vol. 25, pp. 201-220, 1990.
- [57] R. Morrow, "The theory of positive glow corona," *J. Phys. D: Appl. Phys.*, vol. 30, pp. 3099-3114, 1997.
- [58] P. Atten, "Methode generale de resolution du problems du champ electrique modifie par une charge d' espace unipolaire injecte," *Rev. Gen. Electricite*, vol. 83, pp. 143-153, 1974.

-
- [59] M. Abdel-Salam, Z. Alhamouz, "Finite element analysis of monopolar ionized fields including ion diffusion," *J. Phys. D: Appl. Phys.*, vol. 26, pp. 2202-2211, 1993.
- [60] K. Adamiak, "Particle charging by unipolar ionic bombardment in an AC electric field," *IEEE Trans. Ind. Appl.*, vol. 33, iss. 4, pp. 421-426, 1997.
- [61] P. Atten, "Methode generale de resolution du problems du champ electrique modifie par une charge d' espace unipolaire injecte," *Rev. Gen. Electricite*, vol. 83, pp. 143-153, 1974.
- [62] W. Janischewskij and G. Gela, "Finite element solution for electric fields of coronating DC transmission lines," *IEEE Trans. PAS*, vol. 98, no. 3, pp. 1000-1012, 1979.
- [63] J. Q. Feng, "Application of Galerkin finite element method with Newton iterations in computing steady state solutions of unipolar charge currents in corona devices," *J. Comp. Phys.*, vol. 151, iss. 2, pp. 969-989, 1999.
- [64] M. Abdel-Salam, M. Farghally, and A. Abdel-Sattar, "Finite element solution of monopolar corona equation," *IEEE Trans. Electr. Insul.*, vol. 18, no. 2, pp. 110-119, 1983.
- [65] M. Abel-Salam and E. Z. Abdel-Aziz, "Improved calculation for corona loss on three-phase power transmission lines," *Conference Record of the 1996 IEEE Trans. Ind. Appl. Soc. Annual Meeting*, Denver, Colorado, USA, pp. 1601-1607, 1994.

-
- [66] T. Takuma, T. Ikeda, and T. Kawamoto, "Calculation of ion flow fields of HVDC transmission lines by the finite element method," *IEEE Trans. Power Apparatus and Systems*, vol. 100, no. 12, pp. 4802-4810, 1981.
- [67] A. J. Butler, Z. J. Cendes, and J. F. Hoburg, "Interfacing the finite element method with the method of characteristics in self-consistent electrostatic field models," *IEEE Trans. Ind. Appl.*, vol. 25, no. 3, pp. 533-538, 1989.
- [68] Z. M. Al-Hamouz, "A combined algorithm based on finite elements and a modified method of characteristics for the analysis of the corona in wire-duct electrostatic precipitators," *IEEE Trans. Ind. Appl.*, vol. 38, no. 1, pp. 43-48, 2002.
- [69] P. Atten, L. J. Coulomb, and B. Khaddour, "Modelling of electrical field modified by injected space charge," *IEEE Trans. Magn.*, vol. 41, no. 5, pp. 1436-1439, 2005.
- [70] L. N. Menegozzi and P. L. Feldman, "The physics of pulse energization of electrostatic precipitators," *Proc. at the 3rd Symp. Transfer and Utilization of Particulate Control Technology*, Orlando, FL, Mar. 1981.
- [71] S. Sekar, "An investigation of pulsed corona in cylindrical and wire-plate geometries," *J. Electrostatics*, vol. 13, iss. 1, pp. 29-41, 1982.
- [72] L. Salasoo and J. K. Nelson, "Simulation and measurement of corona for electrostatic pulse powered precipitators," *J. Appl. Phys.*, vol. 58, no. 8, pp. 2949-2957, Oct. 1985.
- [73] C. Buccella, "Computation of V-I characteristics of electrostatic precipitators," *J. Electrostatics*, vol. 37, iss. 4, pp. 277-291, 1996.

- [74] A. M. Meroth, T. Garber, C.D. Munz, P.L. Levin, and A.J. Schwab, "Numerical solution of nonstationary charge coupled problems," *J. Electrostatics*, vol. 45, iss. 3, pp. 177-198, 1999.
- [75] X. Liang, S. Jayaram, and A. Berezin, et al. "Modelling of the electrical parameters of a wire-cylinder electrostatic precipitator under pulse energization," *IEEE Trans. Ind. Appl.*, vol. 38, no. 1, pp. 35-42, 2002.
- [76] B. Qin and P. Pedrow, "Particle-in-cell simulation of bipolar dc corona," *IEEE Trans. Diel. Electr. Insul.*, vol. 1, no. 6, pp. 1104-1118, 1994.
- [77] J. Zhang and K. Adamiak, "A dynamic model for negative corona discharge in point-plane configuration," *Proc. of ESA/IEJ/IEEE-IAS/SFE Joint Conference on Electrostatics*, Berkeley, California, vol. 2, pp. 588-597, June 2006.
- [78] G.E. Georghiou, R. Morrow, and A.C. Metaxas, "Characterization of point-plane corona in air at radio frequency using a FE-FCT method," *J. Phys. D: Appl. Phys.*, vol. 32, pp. 2204-2218, 1999.
- [79] R. Loehner, *Applied Computational Fluid Dynamics Techniques: An Introduction Based on the Finite Element Method*, John Wiley and Sons, 2001.
- [80] K. S. Godunov, "A Difference Scheme for Numerical Solution of Discontinuous Solution of Hydrodynamic Equations," *Math. Sbornik*, 47, 271-306, translated US Joint Publ. Res. Service, JPRS 7226, 1969.
- [81] D. Kuzmin and S. Turek, "Flux correction tools for finite elements," *J. of Computational Physics*, vol. 175, iss. 2, pp. 525-558, Jan. 2002.

-
- [82] F. Grane, J. F. loiseau, and N. spyrou, "Numerical and experimental determination of ionizing front velocity in a DC point-to-plane corona discharge," *J. Phys. D: Appl. Phys.*, vol. 113, pp. 1619-29, 1995.
- [83] R. Morrow, "Numerical modelling of time dependent electrical breakdown in non-uniform electric fields," *Proc. 18th int. conf. on phenomena in ionized gases (Swansea wales)*, W. T. Williams, Ed., Bristol: adam hilger, p. 268, 1987.
- [84] R. Morrow and J. J. Lowke, "Streamer propagation in air," *J. Phys. D: Appl. Phys.*, vol. 30, no. 4, pp. 614-27, 1997.
- [85] I. Odrobina and M. Cernak, "Numerical simulation of streamer-cathode interaction," *J. Appl. Phys.*, vol. 78, pp. 3635-42, 1995.
- [86] D. Djermoune, E. Marode, and P. Segur, "Two dimensional modelling of a streamer induced discharge," *Proc. XXII Int. Conf. on phenomena in Ionized gases (Hoboken)*, book 1, p. 33, 1995.
- [87] P. A. Vitello, B. M. Penetrante, and J. N. Bardsley, "Multi dimensional modelling of the dynamic morphology of streamer coronas Non-Thermal Techniques for Pollution Control," B. M. Penetrante and S. E. Schultheis, Eds., Berlin: Springer, part A, pp. 249-72, 1993.
- [88] A. Kulikovsky, "Production of chemically active species in the air by a single streamer in a non-uniform field," *IEEE Trans. Plasma Sci.*, vol. 25, pp. 439-46, 1997.
- [89] P. G. Ciarlet, *The Finite Element Method for Elliptic Problems*, Series "Studies in Mathematics and its Applications," North-Holland, Amsterdam, 1978.

-
- [90] P. J. Waterman, "Meshing: the Critical Bridge," Desktop Engineering Magazine, Aug. 1, 2008.
- [91] M. Sadiku, *Numerical techniques in electromagnetics with MATLAB*, 3rd ed. Boca Raton: CRC Press, c2009.
- [92] X. Deng, Numerical simulation of corona discharge in triode and AC charger, 1997.
- [93] D. Kuzmin, and M. Möller, "Algebraic flux correction I. Scalar conservation laws In: D. Kuzmin, R. Löhner, S. Turek, Eds., Flux-Corrected Transport: Principles, Algorithms, and Applications," New York: Springer, pp. 155-206.
- [94] S. T. Zalesak, "Fully multidimensional flux-corrected transport algorithms for fluids," *J. Comput. Phys.*, vol. 31, pp. 335-362, 1979.
- [95] J. Zhang and K. Adamiak, "A single-species pulsed model of negative corona discharge in air," *IEEE Trans. Ind. Appl.*, vol. 44, no. 2, pp. 494-500, 2008.
- [96] K. Adamiak, V. Atrazhev, and P. Atten, "Corona Discharge in the Hyperbolic Point-plane Configuration: Direct Ionization Criterion versus Approximate Formulations," *IEEE Trans. Dielect. and Electr. Insul.*, vol. 12, no. 5, pp. 1025-1034, 2005.
- [97] K. Adamiak, "Numerical investigation of shape of liquid droplets in an electric field," In C.A. Brebbia, S. Kim, T.A. Oswald, H. Power, Eds., *Boundary Elements XVII*, Comp. Mech. Publ., Southampton, pp. 459-469, 1995.
- [98] N. Sato, "Discharge current induced by the motion of charged particles," *J. Phys. D: Appl. Phys.*, vol.13, iss. 1, pp. L3-L6, 1980.

-
- [99] Yu. S. Akishev, M. E. Grushin, A. A. Deryugin, et al., "Formation of a two-dimensional model for Trichel pulse formation," TRINITY Report by Contract with the ABB Firm, 1997.
- [100] J. Zhang and K. Adamiak, "A multi-species DC stationary model for negative corona discharge in oxygen: point-plane configuration," *J. of Electrostatics*, vol. 65, pp. 459-464, 2007.
- [101] P. Sattari, G. S. P. Castle and K. Adamiak, "FEM-FCT Based Dynamic Simulation of Corona Discharge in Point-Plane Configuration," *IEEE Trans. on Ind. Appl.*, vol. 46, no. 5, pp. 1699-1706, Sept. - Oct. 2010.
- [102] L. B. Loeb, *Electrical Coronas: Their Basic Physical Mechanisms*, Berkeley: University of California Press, 1965.
- [103] SIGLO database, <http://www.lxcat.laplace.univ-tlse.fr>, retrieved February 28, 2011
- [104] MORGAN database, <http://www.lxcat.laplace.univ-tlse.fr>, retrieved February 28, 2011
- [105] PHELP database, <http://www.lxcat.laplace.univ-tlse.fr>, retrieved February 28, 2011
- [106] VIEHLAND database, <http://www.icecat.laplace.univ-tlse.fr>, retrieved February 28, 2011

Appendix A

Appendix A

A.1 Oxygen Model Databases

Tables A.1-A.3 show the model coefficients of the three available databases: Siglo, Morgan and Phepls

Tables A.4 and A.5 show the mobilities of positive and negative ions according to [106].

Table A.1: Model coefficients in oxygen: Siglo database

$EN(\text{Td})$	$\mu_e(1/\text{cm v s})$	$D(1/\text{cm s})$	$a/N(\text{cm}^2)$	$\eta/N(\text{cm}^2)$
1	1.191e+023	2.487e+022	0	2.274e-036
1.287	1.099e+023	2.478e+022	0	1.782e-036
1.656	1.006e+023	2.477e+022	0	3.214e-032
2.131	9.127e+022	2.479e+022	0	1.051e-028
2.742	8.059e+022	2.499e+022	0	4.195e-026
3.529	7.023e+022	2.555e+022	0	4.465e-024
4.541	5.79e+022	2.707e+022	0	1.968e-022
5.843	4.711e+022	2.988e+022	0	3.548e-021
7.519	3.892e+022	3.393e+022	0	3.116e-020
9.676	3.356e+022	3.856e+022	7.827e-035	1.487e-019
12.45	3.025e+022	4.288e+022	2.111e-030	4.339e-019
16.02	2.802e+022	4.652e+022	1.657e-027	8.901e-019
20.62	2.623e+022	4.957e+022	2.915e-025	1.439e-018
26.53	2.48e+022	5.209e+022	1.607e-023	1.949e-018
34.14	2.352e+022	5.426e+022	3.66e-022	2.323e-018
43.93	2.233e+022	5.621e+022	4.287e-021	2.521e-018
56.54	2.116e+022	5.806e+022	3.046e-020	2.559e-018
72.75	1.995e+022	5.991e+022	1.498e-019	2.484e-018
93.62	1.866e+022	6.186e+022	5.625e-019	2.339e-018
120.5	1.728e+022	6.397e+022	1.733e-018	2.153e-018
155	1.578e+022	6.627e+022	4.59e-018	1.945e-018
199.5	1.422e+022	6.884e+022	1.072e-017	1.723e-018
256.7	1.266e+022	7.174e+022	2.235e-017	1.496e-018
330.3	1.12e+022	7.507e+022	4.176e-017	1.271e-018
425.1	9.89e+021	7.887e+022	7.048e-017	1.059e-018
547	8.769e+021	8.323e+022	1.087e-016	8.686e-019
703.9	7.824e+021	8.827e+022	1.553e-016	7.063e-019
905.8	7.027e+021	9.412e+022	2.083e-016	5.744e-019
1166	6.343e+021	1.01e+023	2.656e-016	4.715e-019
1500	5.743e+021	1.091e+023	3.247e-016	3.934e-019

Table A.2: Model coefficients in oxygen: Morgan database

$EN(\text{Td})$	$\mu_e(1/\text{cm v s})$	$D(1/\text{cm s})$	$a/N(\text{cm}^2)$	$\eta/N(\text{cm}^2)$
1	1.19e+023	2.487e+022	0	2.271e-020
1.287	1.099e+023	2.478e+022	0	1.779e-020
1.656	1.008e+023	2.482e+022	0	1.38e-020
2.131	9.14e+022	2.485e+022	0	1.075e-020
2.742	8.071e+022	2.503e+022	0	8.305e-021
3.529	7.016e+022	2.556e+022	0	6.398e-021
4.541	5.79e+022	2.707e+022	0	4.89e-021
5.843	4.719e+022	2.986e+022	0	6.773e-021
7.519	3.886e+022	3.395e+022	0	3.336e-020
9.676	3.351e+022	3.859e+022	3.76e-036	1.505e-019
12.45	3.034e+022	4.282e+022	2.103e-030	4.319e-019
16.02	2.802e+022	4.652e+022	1.637e-027	8.909e-019
20.62	2.624e+022	4.957e+022	2.919e-025	1.44e-018
26.53	2.48e+022	5.209e+022	1.633e-023	1.949e-018
34.14	2.352e+022	5.426e+022	3.793e-022	2.324e-018
43.93	2.233e+022	5.621e+022	4.504e-021	2.521e-018
56.54	2.116e+022	5.805e+022	3.237e-020	2.559e-018
72.75	1.995e+022	5.99e+022	1.601e-019	2.482e-018
93.62	1.868e+022	6.183e+022	6.015e-019	2.335e-018
120.5	1.731e+022	6.391e+022	1.844e-018	2.149e-018
155	1.584e+022	6.611e+022	4.83e-018	1.938e-018
199.5	1.432e+022	6.851e+022	1.114e-017	1.714e-018
256.7	1.281e+022	7.113e+022	2.29e-017	1.485e-018
330.3	1.14e+022	7.402e+022	4.23e-017	1.258e-018
425.1	1.013e+022	7.718e+022	7.079e-017	1.043e-018
547	9.029e+021	8.073e+022	1.088e-016	8.48e-019
703.9	8.08e+021	8.482e+022	1.555e-016	6.791e-019
905.8	7.261e+021	8.967e+022	2.093e-016	5.383e-019
1166	6.545e+021	9.554e+022	2.684e-016	4.239e-019
1500	5.908e+021	1.028e+023	3.301e-016	3.323e-019

Table A.3: Model coefficients in oxygen: Phelps database

$EN(\text{Td})$	$\mu_e(1/\text{cm v s})$	$D(1/\text{cm s})$	$a/N(\text{cm}^2)$	$\eta/N(\text{cm}^2)$
1	7.081e+022	1.25e+022	0	4.489e-020
1.287	6.709e+022	1.248e+022	0	3.505e-020
1.656	6.308e+022	1.246e+022	0	2.737e-020
2.131	5.85e+022	1.243e+022	0	2.134e-020
2.742	5.368e+022	1.239e+022	0	1.666e-020
3.529	4.908e+022	1.241e+022	0	1.297e-020
4.541	4.429e+022	1.244e+022	0	1.006e-020
5.843	3.916e+022	1.254e+022	0	7.819e-021
7.519	3.344e+022	1.293e+022	0	5.957e-021
9.676	2.753e+022	1.382e+022	0	5.176e-021
12.45	2.248e+022	1.536e+022	0	1.577e-020
16.02	1.862e+022	1.757e+022	0	1.002e-019
20.62	1.628e+022	1.985e+022	4.851e-032	4.069e-019
26.53	1.478e+022	2.195e+022	2.618e-029	1.075e-018
34.14	1.375e+022	2.368e+022	1.382e-026	2.053e-018
43.93	1.293e+022	2.512e+022	1.766e-024	3.149e-018
56.54	1.224e+022	2.633e+022	7.675e-023	4.115e-018
72.75	1.161e+022	2.738e+022	1.468e-021	4.779e-018
93.62	1.102e+022	2.834e+022	1.505e-020	5.087e-018
120.5	1.043e+022	2.926e+022	9.697e-020	5.097e-018
155	9.82e+021	3.019e+022	4.43e-019	4.902e-018
199.5	9.166e+021	3.118e+022	1.574e-018	4.587e-018
256.7	8.465e+021	3.225e+022	4.636e-018	4.2e-018
330.3	7.715e+021	3.34e+022	1.181e-017	3.773e-018
425.1	6.944e+021	3.467e+022	2.659e-017	3.322e-018
547	6.187e+021	3.608e+022	5.347e-017	2.865e-018
703.9	5.484e+021	3.766e+022	9.667e-017	2.418e-018
905.8	4.862e+021	3.943e+022	1.586e-016	1.999e-018
1166	4.328e+021	4.146e+022	2.393e-016	1.625e-018
1500	3.873e+021	4.382e+022	3.363e-016	1.308e-018

Table A.4: Mobility of positive ions

$EN(\text{Td})$	$\mu_p(m^2/\text{Vs})$
4.000e+0	2.230e-4
5.000e+0	2.230e-4
6.000e+0	2.230e-4
8.000e+0	2.230e-4
1.000e+1	2.230e-4
1.200e+1	2.230e-4
1.500e+1	2.230e-4
2.000e+1	2.230e-4
2.500e+1	2.230e-4
3.000e+1	2.230e-4
4.000e+1	2.210e-4
5.000e+1	2.180e-4
6.000e+1	2.140e-4
8.000e+1	2.080e-4
1.000e+2	2.020e-4
1.200e+2	1.960e-4
1.500e+2	1.880e-4
2.000e+2	1.770e-4
2.500e+2	1.670e-4
3.000e+2	1.590e-4
4.000e+2	1.450e-4
5.000e+2	1.340e-4

Table A.5: Mobility of negative ions

$EN(\text{Td})$	$\mu_n(m^2/\text{Vs})$
3.000e+0	2.170e-4
4.000e+0	2.170e-4
5.000e+0	2.170e-4
6.000e+0	2.170e-4
8.000e+0	2.170e-4
1.000e+1	2.170e-4
1.200e+1	2.170e-4
1.500e+1	2.170e-4
2.000e+1	2.170e-4
2.500e+1	2.170e-4
3.000e+1	2.160e-4
4.000e+1	2.160e-4
5.000e+1	2.150e-4
6.000e+1	2.140e-4
8.000e+1	2.110e-4
1.000e+2	2.060e-4
1.200e+2	2.010e-4
1.400e+2	1.930e-4

Appendix B

Curriculum Vitae

Name:	Paria Sattari
Place of birth:	Iran
Year of birth:	1981
Post-secondary Education and Degrees:	1999-2003 B.Sc. Electrical Engineering Sharif University of Technology Tehran, Iran 2003-2006 M.Sc. Electrical Engineering Amirkabir University of Technology Tehran, Iran

2007-2011 Ph.D.

Electrical and Computer Engineering

University of Western Ontario

London, Ontario, Canada

Honours and Awards: Best presentation award at the graduate symposium
of ECE department, UWO, London, Ontario, June 2010

Second place best presentation award at ESA conference,
The University of North Carolina, Charlotte, NC, USA,
June 2010

Best Ph.D. presentation award, Cage Club student
conference, McMaster University, Hamilton, Ontario,
Aug. 2009

Best presentation award at the graduate symposium
of ECE department, UWO, London, Ontario, June 2009

Graduate research scholarship at UWO, London, Ontario,
May 2007

First rank among the M.Sc. telecommunications students
of the Electrical Engineering Department, Amirkabir
University of Technology, Sept. 2005

Related Work Research Assistant, Research Group, Niroo Research
Experience: Centre (MATN), Tehran, Iran, 2002

Research Assistant, Amirkabir University of Technology,
Tehran, Iran, Electromagnetic Research Lab, 2003-2006

Research Engineer, Iran Telecom Research Centre (ITRC),
Communication Technology Department, 2006-2007

Research Assistant
The University of Western Ontario
2007-2011

Teaching Assistant
The University of Western Ontario
2007-2011

Publications:

- [1] P. Sattari, G. S. P. Castle and K. Adamiak, "FEM-FCT based dynamic simulation of corona discharge in point-plane configuration," *IEEE Transactions on Industry Applications*, vol. 46, no. 5, pp. 1699-1706, Sept.-Oct. 2010. (also presented at ESA/IEEE-IAS/SFE Joint Conference on Electrostatics, Boston, MA, 16-18 June 2009)

-
- [2] P. Sattari, G. S. P. Castle and K. Adamiak, "FEM-FCT based 2D Simulation of Trichel Pulses in Air," under review to be published in IEEE Transactions on Industry Applications. (also presented at IEEE/IAS Annual Meeting, Houston, TX, 3-7 Oct. 2010)
- [3] P. Sattari, C. F. Gallo, G. S. P. Castle, K. Adamiak, "Trichel Pulse Characteristics - Negative Corona Discharge in Air," *J. Phys. D: Appl. Phys.*, vol. 44, April. 2011.
- [4] P. Sattari, G. S. P. Castle, K. Adamiak, "Numerical simulation of Trichel pulse corona in oxygen," to be submitted to IEEE Transactions on Industry Applications.
- [5] P. Sattari, G. S. P. Castle and K. Adamiak, "Investigation of Trichel Pulses in Oxygen and Air," *ESA Annual Meeting on Electrostatics, Cleveland, Ohio*, June 2011.
- [6] P. Sattari, G. S. P. Castle and K. Adamiak, "Numerical Algorithm For Simulating Trichel Pulses in Electric Corona Discharge in Air," *ISEF 2011 - XV International Symposium on Electromagnetic Fields in Mechatronics, Electrical and Electronic Engineering, Funchal, Madeira*, September 1-3, 2011.
- [7] P. Sattari, G. S. P. Castle and K. Adamiak, "A Numerical Model of Trichel Pulses in Air; the Effect of Pressure," *13th International Conf. on Electrostatics, Wales, UK*, April 2011.
- [8] P. Sattari, G. S. P. Castle and K. Adamiak, "Numerical simulation of Trichel pulses in a negative corona discharge in air," *ESA Annual Meeting on Electrostatics, Charlotte, NC*, 22-24 June 2010.

-
- [9] P. Sattari, "Two dimensional simulation of Trichel pulse regime of negative corona discharge in point-plane configuration," presented at the Cage Club Student Conference on High Voltage Engineering and Applied Electrostatics, University of Western Ontario, ON, 12th Aug. 2010.
- [10] P. Sattari, "Two dimensional modeling of Trichel pulse corona in air," presented at the Cage Club Student Conference on High Voltage Engineering and Applied Electrostatics, McMaster University, ON, 12th Aug. 2009.
- [11] P. Sattari, "Dynamic simulation of corona discharge in point-plane configuration," presented at the Cage Club Student Conference on High Voltage Engineering and Applied Electrostatics, University of Ontario Inst. of Tech., ON, 20th Aug. 2008.